

THE DEVELOPMENT OF THE SNO+ EXPERIMENT:  
SCINTILLATOR TIMING, PULSE SHAPE  
DISCRIMINATION, AND STERILE NEUTRINOS

by

ERIN O'SULLIVAN

A thesis submitted to the  
Department of Physics, Engineering Physics & Astronomy  
in conformity with the requirements for  
the degree of Doctor of Philosophy

Queen's University  
Kingston, Ontario, Canada

April 2014

Copyright © Erin O'Sullivan, 2014

# Abstract

The SNO+ experiment is a multi-purpose neutrino detector which is under construction in the SNOLAB facility in Sudbury, Ontario. SNO+ will search for neutrinoless double beta decay, and will measure low energy solar neutrinos.

This thesis will describe three main development activities for the SNO+ experiment: the measurement of the timing parameters for the liquid scintillator cocktail, using those timing parameters to estimate the ability of SNO+ to discriminate alpha and beta events in the detector, and a sensitivity study that examines how solar neutrino data can constrain a light sterile neutrino model.

Characterizing the timing parameters of the emission light due to charged-particle excitation in the scintillator is necessary for proper reconstruction of events in the detector. Using data obtained from a bench-top setup, the timing profile was modelled as three exponential components with distinct timing coefficients. Also investigated was the feasibility of using the timing profiles as a means to separate alpha and beta excitation events in the scintillator. The bench-top study suggested that using the peak-to-total method of analyzing the timing profiles could remove  $>99.9\%$  of alpha events while retaining  $>99.9\%$  of beta events. The timing parameters measured in the test set-up were then implemented in a Monte Carlo code which simulated the SNO+ detector conditions. The simulation results suggested that detector effects reduce the

effectiveness of discriminating between alpha and beta events using the peak-to-total method. Using a more optimal method of analyzing the timing profile differences, specifically using a Gatti filter, improved the discrimination capability back to the levels determined in the bench-top setup.

One of the physics goals of SNO+ is the first precision measurement of the pep solar neutrino flux at the level of about 5 % uncertainty. A study was performed to investigate how current solar neutrino data constrains the allowed parameters of a light 3+1 sterile neutrino model. The impact of adding a SNO+ pep solar neutrino measurement on the allowed parameters of the sterile model was then examined.

# Statement of Originality

Being a member of an experimental physics collaboration often means that the work produced by an individual will be performed in collaboration with others.

In this thesis, the work in Chapter 4 was performed in collaboration with Helen O’Keeffe and Mark Chen. The author of this thesis participated in designing and setting up the apparatus, and was a leader in the data taking. The author also developed the analysis code that was ultimately used to extract the final numbers from the timing fit. For the pulse shape discrimination capability study, the author worked in collaboration with Helen O’Keeffe to obtain the bench top results quoted in this thesis. For the study using pulse shape discrimination to identify  $^{210}\text{Po}$  in the SNO+ detector, the author used the RAT Monte Carlo code which was developed by the SNO+ collaboration. The analysis of this data was performed solely by the author of this thesis.

In Chapter 5, the code which produced the survival probability tables that included the effects from sterile neutrinos was developed by the author using an active neutrino oscillation code which was developed by Ryan Martin. The global fit results used the QPhysics code which was developed by the SNO experiment. The analysis and interpretation of the global fit was solely the work of the author of this thesis.

# Acknowledgments

First and foremost, thank you to my advisor Mark Chen for his guidance both with this thesis and with my research work in general. Mark somehow found a good balance between giving me enough independence to develop my own research style and being present enough to advise me when I was really stuck on a problem.

Also, thanks to Alex Wright, who was a great source for advice at the very beginning (and then again at the very end) of my degree. When you left I felt like I had big shoes to fill, and that made me strive to be a better physicist. Thanks, also, to Art McDonald for his useful physics discussions and for being an example of how to love what you do.

To Satoko Asahi, who was the best office and travel mate, thanks for the adventures abroad and for your many potluck parties here in Kingston. I especially enjoyed our time in Japan when you introduced me to onsens, sake, and the delicacy of raw horse meat.

To the rest of the SNO+ group, past and present, including Helen, Nasim, Matt, Maryam and Emilie, thanks for your friendship, and for making the long drives to Sudbury fun. To my fellow basement-dwellers, including Paradorn, Yohan, Patrick, and Alvine, try and go out into the sunshine every once in a while.

I am indebted to high school physics teacher, Greg Pickering, who introduced me

to the Sudbury Neutrino Observatory and who encouraged me to pursue science as a career. I am so grateful to Richard Ford for hiring a 19 year old with hardly any physics knowledge and giving me my first neutrino physics job. That opportunity opened many doors for me very early in my career, and without it I would not be where I am today.

Finally, to my family, thanks for your support and patience. Thanks to my parents for being an ever-present source of assistance, whether that meant helping me move to Sudbury in the middle of January, or picking me up from a late-night flight after a conference. Lastly, thank you to Evan, who is my partner in life but also plays a big role in my research. Thank you for your proofreading, formatting, deriving, and coding advice, and also for knowing when I needed to get out of the house and have some fun. I can't wait to start the next chapter with you.

# Table of Contents

Abstract	i
Statement of Originality	iii
Acknowledgments	iv
Table of Contents	vi
List of Tables	viii
List of Figures	ix
<b>1 Thesis Overview</b>	<b>1</b>
1.1 Main results contained in this thesis . . . . .	1
1.2 Organization of the thesis . . . . .	3
<b>Chapter 2:</b>	
<b>Introduction to Neutrinos . . . . .</b>	<b>5</b>
2.1 Neutrinos: A History . . . . .	6
2.2 Neutrinos: A Modern Picture . . . . .	15
2.3 The Standard Solar Model . . . . .	19
2.4 (Active) Neutrino Oscillations . . . . .	22
2.5 Solar Neutrino Propagation (In Words) . . . . .	32
2.6 The Electron Neutrino Survival Probability . . . . .	34
<b>Chapter 3:</b>	
<b>The SNO+ Experiment . . . . .</b>	<b>37</b>
3.1 SNOLAB . . . . .	38
3.2 The SNO Detector . . . . .	38
3.3 Transitioning from SNO to SNO+ . . . . .	39
3.4 SNO+ Run Plan . . . . .	42
3.5 SNO+ Physics Goals . . . . .	44

3.6	A final word on backgrounds (for now)	55
<b>Chapter 4:</b>		
	<b>Timing Measurements in Linear Alkylbenzene</b>	<b>56</b>
4.1	Motivation	56
4.2	The SNO+ Scintillator Cocktail	57
4.3	Scintillator Physics	58
4.4	Experimental Apparatus and Method	60
4.5	Extraction of Timing Parameters from Timing Profiles	64
4.6	Comparison of Timing Parameters Found in Literature	67
4.7	Pulse Shape Discrimination with the Bench-Top Results	68
4.8	Application of Pulse Shape Discrimination in the SNO+ Experiment	70
4.9	Summary and Conclusions	76
<b>Chapter 5:</b>		
	<b>Solar Neutrinos as a Probe for a 3+1 Model</b>	<b>78</b>
5.1	An Introduction to Sterile Neutrinos	79
5.2	Sterile Neutrino Oscillations in the Sun	81
5.3	The Effect of Sterile Neutrino Mixing on Active Neutrino Observables	86
5.4	The Global Fit Code	93
5.5	Individual Experimental Contributions to the Global Fit	107
5.6	Global fits for Allowed Sterile Neutrino Parameters	111
5.7	Summary and Conclusions	114
<b>Chapter 6:</b>		
	<b>Conclusions and Recommendations</b>	<b>123</b>
	<b>Bibliography</b>	<b>125</b>
<b>Appendix A:</b>		
	<b>Background Decay Chains</b>	<b>136</b>
<b>Appendix B:</b>		
	<b>List of Important Acronyms</b>	<b>138</b>

# List of Tables

2.1	Predicted Solar Neutrino Fluxes from BS05(OP) . . . . .	22
3.1	Neutrinoless double beta decay candidates with their corresponding Q-value and natural abundance. . . . .	47
4.1	Summary of timing results from alpha and beta timing profiles . . . .	67
4.2	Comparison of timing parameters found in literature . . . . .	68
5.1	Best Fit Values for the SNO Experimental Observables . . . . .	102

# List of Figures

2.1	Neutrino production regions in the Sun. . . . .	20
2.2	Electron and neutron density profiles in the Sun. . . . .	21
2.3	The Feynman diagrams for the elastic scattering interactions with matter. . . . .	26
2.4	Effect of the resonance region on neutrino flavour states . . . . .	33
2.5	Three cases of neutrino propagation in the Sun . . . . .	35
2.6	Survival probability of a solar electron neutrino, $P_{ee}$ , as a function of neutrino energy for a ${}^8\text{B}$ neutrino averaged over the production region. The low energy plateau in $P_{ee}$ is the vacuum dominated region. The high energy plateau in $P_{ee}$ is the matter dominated effect. . . . .	36
3.1	A schematic of the SNO Detector . . . . .	39
3.2	A schematic of the SNO+ Detector . . . . .	41
3.3	Idealized schematic of the neutrinoless double beta decay signal . . . . .	48
3.4	SNO+ energy spectrum with tellurium in the detector after two years of livetime . . . . .	49
3.5	Thermonuclear reactions in the Sun that produce solar neutrinos . . . . .	51
3.6	Energy spectra of solar neutrino fluxes as predicted by the Standard Solar Model . . . . .	52
3.7	Solar neutrino signal in the SNO+ detector with backgrounds . . . . .	54
4.1	Electronics setup for scintillator timing profiles. . . . .	61
4.2	Electronics setup for scintillator timing profiles taken in the deoxygenated configuration. . . . .	65
4.3	Background subtracted timing profiles due to alpha and beta excitation for oxygenated and deoxygenated scintillator. . . . .	66
4.4	Peak-to-total ratios for excitations due to alpha and beta particles in oxygenated and deoxygenated LAB+PPO. . . . .	70
4.5	CNO signal with ${}^{210}\text{Bi}$ background. . . . .	71
4.6	Timing spectrum from alpha and electron particles in the SNO+ detector. . . . .	73
4.7	Peak-to-total ratios using simulated data from RAT. . . . .	74
4.8	Gatti number distributions using simulated data from RAT. . . . .	76
4.9	Comparison of the peak-to-total and the Gatti method. . . . .	77

5.1	Effect Aof sterile neutrino mixing on survival probability . . . . .	89
5.2	Schematic of the Homestake detector . . . . .	94
5.3	A schematic drawing of the SAGE and GALLEX/GNO experiments.	96
5.4	A schematic drawing of the water Cherenkov experiments: Super-Kamiokande and SNO. . . . .	97
5.5	Schematic of the Borexino detector . . . . .	98
5.6	The fit of the SNO data using the polynomial $P_{ee}$ and the day-night asymmetry function $A_{ee}$ . . . . .	101
5.7	Allowed sterile neutrino parameters considering radiochemical experiments only. . . . .	115
5.8	Allowed sterile neutrino parameters considering the Borexino ${}^7\text{Be}$ solar neutrino measurement only. . . . .	116
5.9	Allowed sterile neutrino parameters considering the ${}^8\text{B}$ solar neutrino measurements from SNO and SK only. . . . .	117
5.10	Allowed sterile neutrino parameters considering the pep solar neutrino measurements from borexino only. . . . .	118
5.11	Allowed sterile neutrino parameters considering an example of a future pep solar neutrino measurement, which agrees with the LMA solution, from SNO+. . . . .	119
5.12	Allowed sterile neutrino parameters considering all current solar neutrino data. . . . .	120
5.13	Allowed sterile neutrino parameters considering all current solar neutrino data and the expected LMA pep signal after one year of SNO+ live-time. . . . .	121
5.14	Allowed sterile neutrino parameters considering all current solar neutrino data and the expected LMA pep signal after two years of SNO+ live-time. . . . .	122
A.1	Thorium decay chain. . . . .	136
A.2	Uranium decay chain. . . . .	137

# Chapter 1

## Thesis Overview

### 1.1 Main results contained in this thesis

This thesis covers key research on the development of the SNO+ experiment. There are three main results contained in this thesis: the measurement of the timing components of the scintillation light emission for a scintillator cocktail of linear alkylbenzene with PPO fluor, an investigation into how timing can be used to differentiate beta and alpha excitation in the scintillator cocktail, and a sensitivity study on the impact of a pep neutrino measurement on a light sterile neutrino model. The first two results address the development of the tools that SNO+ requires to reconstruct its signal and to disentangle signal events from background events, while the third result follows as an example of how a SNO+ measurement could impact the field of neutrino physics.

### **1.1.1 Measuring the timing components of linear alkylbenzene**

Linear alkylbenzene with PPO fluor is gaining popularity as a scintillating detection medium in neutrino experiments. Besides being used in SNO+, linear alkylbenzene with PPO is used in RENO [1] and Daya Bay [2] and could be used in the proposed LENA experiment [3].

The results in Chapter 4 represent the first published measurement of the alpha timing components for LAB+PPO. Accurate measurement of the timing components is vital for proper event reconstruction in the experiment, and thus these measured parameters are very useful for the SNO+ experiment.

### **1.1.2 Using timing to discriminate between alpha and beta events**

The emission timing in the scintillator differs if the event is from alpha or beta excitation. This difference in timing profiles can be utilized to remove alpha background events from beta signals.

The work in Chapter 4 is the first time that the timing was examined as a means for separating alpha and beta events in this scintillator cocktail. Though it was generally accepted that the ability to separate alpha and beta events using timing profiles in liquid scintillator improved with deoxygenation, this work was the first to show that this was conclusively the case.

### 1.1.3 Sensitivity of a pep neutrino measurement on a light sterile neutrino model

The search for sterile neutrinos is an active area of modern neutrino research. Oscillations of active neutrinos into sterile neutrino states would be an extension to the standard model. Using solar neutrino data from past experiments, this thesis shows how the allowed parameters of a light 3+1 sterile model can be constrained. Furthermore, the work in Chapter 5 shows how a SNO+ pep neutrino measurement could further constrain the model parameters.

The work in Chapter 5 is important as it is the first time that the 3+1 sterile neutrino model was examined in light of the latest results from SNO, including the proper polynomial fit to the data. This thesis also is the first to present the impact of a pep neutrino measurement on the allowed model parameters.

## 1.2 Organization of the thesis

Chapter 2 will introduce the reader to the historical milestones in neutrino physics and to the modern questions that current neutrino experiments are attempting to address. This chapter will set up the mathematical framework which describes neutrino oscillation, and will outline a detailed description of neutrino propagation through the Sun. The purpose of Chapter 2 is to show how the original research contained in this thesis fits into the overall field of neutrino physics, as well as to set up the necessary background information on neutrino oscillations.

Chapter 3 will discuss the details of the SNO+ experiment. A description of the SNO+ detector will be given, and an overview of the current construction activities

which are underway will be discussed. The two main physics goals of the experiment, neutrinoless double beta decay detection and low energy solar neutrino measurements, will be described. The purpose of Chapter 3 is to introduce how a signal event would appear in the SNO+ detector and to show the backgrounds that could hinder the measurements of these signals. By showing that some backgrounds are in the same energy region as the signals, it will motivate the investigation of a discrimination method which is described in Chapter 4. The description of the detector, as well as the information on the low energy solar neutrino measurement, will be useful for Chapter 5.

Chapter 4 describes the measurement of the timing parameters from scintillation light emission in linear alkylbenzene. A study to examine if alpha and beta events could be differentiated using pulse shape discrimination (PSD) was performed using the bench-top data. The timing parameters were then implemented in the SNO+ Monte Carlo code to simulate how detector effects could affect the alpha-beta discrimination. Finally, as a concrete example of how PSD could be used to tag backgrounds, a study of the efficiency of using PSD to tag  $^{210}\text{Po}$  in the detector was performed. Two PSD methods, peak-to-total and Gatti's method, were compared to determine the best way to identify the  $^{210}\text{Po}$  background events.

Chapter 5 outlines a sensitivity study which looks at how solar neutrino data can be used to constrain the parameters of a light sterile neutrino model. Results are first presented using current solar neutrino data, then the effects due to the addition of a future pep solar neutrino measurement are examined.

# Chapter 2

## Introduction to Neutrinos

Neutrinos, the existence of which was first proposed in 1930, have been one of the most unusual particles ever studied and hold the promise of an even more interesting future. This chapter will provide some background information on neutrinos. Section 2.1 is an overview of the historical milestones in the field of neutrino physics. Section 2.2 summarizes our current understanding of the neutrino and outlines some open questions in the field. Section 2.3 will introduce the standard solar model, which is our greatest tool for understanding the neutrino observables from the Sun. Section 2.4 is the real heart of the chapter, outlining the mathematical framework that describes how neutrinos oscillate. The rigorous treatment of the mathematics of neutrino oscillations will help the reader to better understand the material related to sterile neutrino oscillations in Chapter 5. Finally, a summary of how neutrinos propagate through the Sun using the concepts introduced throughout this chapter will be given with a colloquial description in section 2.5 and with a description of the electron neutrino survival probability curve in section 2.6.

## 2.1 Neutrinos: A History

Modern neutrino physics is a rich area of study, but the road to our current knowledge of neutrino properties has been paved by some truly amazing theorists and experimentalists. This section is by no means a complete history of all aspects of neutrino physics, but it will attempt to instill an appreciation for the difficulties faced by early neutrino physicists, as well as to outline some of the major milestones in neutrino physics research.

### The Birth of the Neutrino

In 1930, Wolfgang Pauli wrote a letter to a physics conference in Tübingen, Germany which began “Dear Radioactive Ladies and Gentlemen”. In this letter, Pauli went on to propose that there existed a neutral, weakly interacting fermion which could explain the surprising result that the  $\beta$  spectrum was continuous. He called his new particle a neutron [4]. In 1932, Chadwick discovered the particle that we now know as the neutron [5], and Pauli’s particle was renamed the neutrino. Pauli’s letter would set in motion a journey that would take us into the depths of the earth and inspire scientists to attempt seemingly impossible measurements<sup>1</sup>. It would lead to the creation of high energy accelerators, and to new detector technology. It would be another 26 years before the neutrino was observed, and there would be many puzzles, some of which we are still attempting to solve today.

---

<sup>1</sup>In fact, Pauli is famously known for saying “I have done something very bad today by proposing a particle that cannot be detected; it is something no theorist should ever do.”

### **The First Antineutrino Measurement**

The first detection of an antineutrino came in the 1950s by physicists Clyde Cowan and Fred Reines. Cowan and Reines used a water tank containing dissolved  $\text{CdCl}_2$ , which was surrounded by liquid scintillator. The detector was placed near a nuclear reactor, which is a rich source of antineutrinos. A preliminary first measurement was made in 1953 [6] and a later, more conclusive, measurement was made in 1956 [7]. This experiment resulted in a Nobel Prize in 1995 for Reines (Cowan died in 1974).

### **Parity Violation is Discovered**

Conservation of parity rules state that reactions must be invariant under space inversion, for example when moving from a right-handed to left-handed system. Parity conservation was established in the strong interaction sector, and was assumed to also hold for weak interactions. In 1956, Tsung Dao Lee and Chen Ning Yang proposed an experiment which would be able to detect parity violation in weak interactions by observing the beta decays from polarized  $^{60}\text{Co}$  [8]. This experiment was performed by Chien-Shiung Wu, also in 1956, and parity violation was discovered [9], earning Lee and Yang the 1957 Nobel prize. In an experiment performed by Goldhaber in 1958, it was determined that neutrinos violated parity maximally and that the neutrino is left handed, while the antineutrino is right handed [10].

### **The First Solar Neutrino Measurement**

In 1951 Ray Davis Jr., the grandfather of modern solar neutrino research and the recipient of the 2002 Nobel Prize in Physics for his pioneering work, began his pursuit to measure the first solar neutrino [11]. The Sun is an abundant source of neutrinos,

but they are notoriously hard to measure due to their low reaction cross section. Davis built a detector which consisted of a 378,000 litre tank of tetrachloroethylene ( $C_2Cl_4$ ) which he constructed underground in a defunct gold mine in South Dakota [12]. Davis looked for the reaction which was first proposed as a detection method by Pontecorvo in 1946 [13], where the neutrino changes a chlorine atom to an argon atom, as in equation 2.1. This experiment will be referred to later in this thesis as the Homestake experiment, after the mine where the detector was located.



In 1962, Davis sought the help of John Bahcall, a theorist who could construct a model which would predict the expected number of solar neutrinos [14]. Davis discovered he was measuring about a third of neutrinos that Bahcall's model predicted he should see. This would come to be known as the solar neutrino problem [11]. This discrepancy between the theoretical expectation and the observed number of solar neutrinos was a difficult period in the history of neutrino physics. The process of extracting and measuring a small number of argon atoms led some to question the results of Davis' experiment. More overwhelmingly, many experimentalists questioned whether theorists could accurately model solar physics well enough to make predictions of the neutrino flux. This dilemma was outlined in a paper from Bahcall [15]. In this paper he states,

The attitude of many physicists toward the present discrepancy is that astronomers never really understand astronomical systems as well as they think they do, and the failure of the standard theory in this simple case just proves that physicists are correct in being skeptical of the

astronomers' claims. Many astronomers believe, on the other hand, that the present conflict between theory and observation is so large and elementary that it must be due to an error in the basic physics, not in our astrophysical understanding of stellar evolution.

The next experiment to make a solar neutrino measurement would not do so for many years. An experiment in a Japanese mine, which was originally constructed to search for nucleon decay, underwent upgrades in 1986 in order to be able to detect solar neutrinos. The experiment, called KamiokaNDE II [16] (the Kamioka Nucleon Decay Experiment) consisted of 3000 tons of water in a cylindrical steel tank. The measurement from the KamiokaNDE II experiment represented the first real-time measurement of neutrinos coming from the Sun. The experiment measured solar neutrinos from January 1987 to February 1995. In 1988, KamiokaNDE II reported a flux of  $0.46 \pm 0.13(\text{stat}) \pm 0.08(\text{sys})$  of the value predicted from the solar model [16].

The KamiokaNDE II measurement sparked interest in the physics community and motivated others to build experiments to measure solar neutrinos. The next experiments to measure solar neutrinos, GALLEX [17] and SAGE [18], used gallium as a detector medium. The advantage of the gallium experiments was that they could measure solar neutrinos which were very low in energy. Using the reaction described in equation 2.2, solar neutrinos as low as 0.2 MeV could be detected (compared with 0.8 MeV for Homestake and 9 MeV for KamiokaNDE II). SAGE and GALLEX published results in the early 1990s. In 1998, the GALLEX experiment ended and the next phase of the experiment, the Gallium Neutrino Observatory (GNO) began taking data. SAGE and the GALLEX/GNO results saw only 56% - 60% of the

neutrino capture rate predicted by the solar model [19, 20].

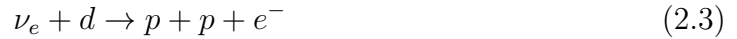


In 1969, V.N Gribov and B. Pontecorvo proposed that a solution to the solar neutrino problem could be that neutrinos change flavours as they travel from the Sun to the Earth [21]. All reactions which produce neutrinos in the Sun produce only electron type neutrinos. The radiochemical experiments (Homestake and the gallium experiments) are sensitive only to electron neutrinos, while the water experiment, KamiokaNDE II, had sensitivity to all types of neutrinos but the electron neutrinos had a higher cross section in the reaction than muon or tau flavour neutrinos. The fact that radiochemical experiments saw a different result than KamiokaNDE II, as well as the fact that all experiments were seeing a deficit of neutrinos from the model predictions, made this an appealing solution.

### **The Solar Neutrino Problem is Solved**

In 1985, Herb Chen proposed an experiment which could address the hypothesis that neutrinos oscillate [22]. The Sudbury Neutrino Observatory (SNO) was designed to have a reaction channel which is sensitive to only electron neutrino flavours and another reaction channel which is sensitive to all neutrino flavours equally [23]. SNO was located in a nickel mine in Sudbury, Ontario and took data from 1999 until 2006. The SNO detector consisted of a detector volume of heavy water ( ${}^2\text{H}_2\text{O}$ ), surrounded by a volume of light water to provide shielding. SNO measured solar neutrinos primarily using the two reactions outlined in equations 2.3 and 2.4. Equation 2.3 is called the charged current (CC) reaction and occurs when an electron neutrino interacts with

the deuterium and produces two protons and an electron. Equation 2.4 is called the neutral current reaction and occurs when a neutrino interacts with the deuterium and produces a neutrino, a proton, and a neutron. Equation 2.3 is sensitive strictly to electron flavoured neutrinos, while equation 2.4 is sensitive to all flavours of neutrinos equally.



In the neutral current channel, SNO obtained a  $^8\text{B}$  neutrino flux of  $5.09^{+0.44}_{-0.43}(\text{stat})^{+0.46}_{-0.43}(\text{syst}) \times 10^6 \text{ cm}^{-2} \text{ s}^{-1}$ , which was in agreement with the solar model [24]. In the charged current reaction channel, measured a  $\nu_e$  flux of  $1.76 \pm 0.05(\text{stat}) \pm 0.09(\text{syst}) \times 10^6 \text{ cm}^{-2} \text{ s}^{-1}$  above a 5 MeV threshold, which infers a non- $\nu_e$  component of  $3.41 \pm 0.45(\text{stat})^{+0.48}_{-0.45}(\text{syst}) \times 10^6 \text{ cm}^{-2} \text{ s}^{-1}$  [24]. The non- $\nu_e$  component was  $5.3 \sigma$  greater than zero, which provided strong evidence for solar neutrino oscillations and solved the long-standing solar neutrino problem [24]. A more detailed description of the SNO detector and the experimental results of the experiments mentioned above can be found in Sections 3.2 and 5.4.1 respectively.

### Neutrino Oscillations are Discovered using Atmospheric Neutrinos

In 1998 the successor of the KamiokaNDE II experiment, called Super-Kamiokande, saw evidence for neutrino oscillations in the atmospheric neutrino sector [25]. Due to charged particle interactions in the atmosphere, the production rate of muon neutrinos and antineutrinos should be twice that of electron neutrinos and antineutrinos.

Super-Kamiokande, which was sensitive to both electron and muon type neutrinos, measured a deficiency in the rate of muon neutrinos that was dependent on the zenith angle. This observation was consistent with the oscillation of muon neutrinos into tau neutrinos [25]. As this discovery was made prior to the SNO measurement, the Super-Kamiokande results were the first conclusive observation of neutrino oscillations.

### **The Muon and Tau Neutrino are Discovered**

In 1962, an experiment at Brookhaven discovered muon neutrinos in the decay of pions [26]. In 1988, the Nobel prize was awarded to Leon Lederman, Melvin Schwartz, and Jack Steinberger, for the neutrino beam method and the demonstration of the doublet structure of the leptons through the discovery of the muon neutrino.

In 2000, the final neutrino flavour was observed with the discovery of the tau neutrino by the Direct Observation of the NU Tau (DONUT) collaboration [27].

### **Determination of the Number of Active Neutrino Species**

In 1989, the width of the decay process of the Z boson was measured at the LEP collider at CERN. The measurement determined that only three generations of light neutrinos can couple to the Z boson [28, 29, 30, 31].

### **Neutrinos from a Supernova are Observed**

In 1987, a blue supergiant named Sanduleak became the first supernova visible to the naked eye since Kepler made his supernova observation in 1604 [32]. Sanduleak -69°202 was a star in the Large Magellanic Cloud, which is located about 50 kpc from

Earth [32]. This supernova was designated as SN1987A. Measuring supernova neutrinos can give information about neutrino properties, as well as about the supernova core-collapse mechanism. Three neutrino experiments observed the neutrinos from SN1987A: IMB, Baksan, and KamiokaNDE II. IMB recorded 8 neutrino-like events [33], Baksan recorded 5 events [34], and KamiokaNDE II recorded 11 events [35]. This observation was important in the context of neutrino history because it was the first time neutrinos which originated outside of our solar system were measured.

### **The Race to Measure Neutrino Mixing Parameters**

Once it was known that neutrinos oscillate, physicists turned their attention to characterizing the behaviour of the oscillation. The mathematics of neutrino oscillation will be discussed in section 2.4, but generally speaking neutrino oscillations can be mathematically described using three mixing angles ( $\theta_{12}$ ,  $\theta_{23}$ , and  $\theta_{13}$ ) and two mass squared differences between the three mass eigenstates ( $\Delta m_{21}^2$  and  $\Delta m_{31}^2$ ).

The measurement of these oscillation parameters has relied on the input of many different experiments to paint a complete picture. The current best-fit parameters, as well as the experiments which have contributed to that measurement, can be found in [36]. Solar neutrinos are most sensitive to the behaviour of  $\theta_{12}$ , and so the SNO experiment has the leading measurement for that oscillation parameter [37]. Atmospheric neutrinos are sensitive to  $\theta_{23}$  so the Super-Kamiokande experiment has made the best measurement of that parameter [38]. KamLAND, which is a reactor neutrino experiment, has made the best measurement of  $\Delta m_{21}^2$  [39]. A beam-line experiment called MINOS has made the best measurement of  $\Delta m_{32}^2$  [40]. The last piece of the neutrino mixing parameter puzzle,  $\theta_{13}$  was measured in 2011, by the Daya

Bay experiment [41].

### Hints for a Sterile Neutrino?

Measurements of the width of the Z boson decay determined that only three types of light active neutrinos exist. There could, however, exist neutrinos which do not couple to the Z boson and which do not take part in any weak interactions. These neutrinos would be right-handed neutrinos and left-handed antineutrinos.

The search for sterile neutrinos in the solar sector will be discussed in great detail in Chapter 5. In this section, the sterile neutrino and how it pertains to an open question in the field, will be addressed. Sterile neutrinos attracted attention in the 1990s when the LSND (Liquid Scintillating Neutrino Detector) experiment measured an excess of electron antineutrinos from a muon antineutrino beam [42]. The results of the LSND experiment could only be explained by a neutrino flavour with a mass squared difference of  $\Delta m^2 \sim 1\text{eV}$  (where  $\Delta m^2$  is the difference between two neutrino mass eigenstates  $i$  and  $j$  such that  $\Delta m_{ij}^2 = m_i^2 - m_j^2$ ), which is much larger than the  $\Delta m^2$  values measured for the three active neutrinos. Since it was known from the LEP experiments that there could only be three light active neutrino flavours, this led to the proposition that the oscillation behaviour at LSND could be explained by the inclusion of a sterile neutrino which does not couple to the bosons. More recently MiniBooNE, an experiment constructed to test the validity of the LSND experiment, published results which also suggested an anomaly in the expected appearance probability [43], though there are some discrepancies between the MiniBooNE and LSND results which are the subject of ongoing investigations [44].

Another piece of experimental evidence which could point to the existence of

a sterile neutrino comes from gallium-based neutrino experiments. Two previously mentioned solar neutrino experiments, SAGE [18] and GALLEX [17], discovered that when their detectors were calibrated with a neutrino source, less neutrinos were observed than the strength of the radioactivity of the source suggested [45, 46]. This discrepancy is statistically significant at a  $\sim 3\sigma$  level [47].

The most recent hint for a sterile neutrino comes from reactor neutrino measurements. A recent recalculation of the expected reactor neutrino flux indicates that it should be higher than the flux detected by all previous short baseline reactor neutrino experiments. This is known as the “reactor neutrino anomaly” and is at the significance of close to  $3\sigma$  [48].

The hints from LSND, gallium experiments, and reactor neutrinos all point to a sterile neutrino with  $\Delta m^2 \sim 1\text{eV}^2$ .

Hints for sterile neutrino mixing affecting the solar neutrino energy region also exist. Data from SNO and Super-Kamiokande do agree with the anticipated result from having only three active neutrinos, but a model which has a sterile neutrino is weakly favoured from this data. For a sterile neutrino to affect solar neutrino oscillations, it would need a mass which is similar to the active neutrino mass eigenstates. More on the hints and consequences of sterile neutrino mixing with solar neutrinos will be addressed in Chapter 5.

## 2.2 Neutrinos: A Modern Picture

Now that the history of the neutrinos has been introduced, it is important to summarize our current understanding of neutrinos, as well as to explain what measurements current and next-generation neutrino experiments will be performing.

### 2.2.1 A Modern Definition of the Neutrino

Neutrinos are neutral, weakly-interacting leptons. Originally assumed to be massless, we now know that neutrinos have a very tiny mass compared to other subatomic particles. Neutrinos come in three flavours: electron, muon, and tau. We know that no other light active neutrino flavours exist from the LEP experiments. An interesting property of the neutrino is that it mixes in flavour, so a neutrino that is created as an electron flavour can be detected as a muon or tau flavour some time later. A similar type of mixing behaviour has also been seen in kaons.

### 2.2.2 Open Questions in Neutrino Physics

While we have come a long way in our understanding of neutrino physics, there are still a number of unanswered questions in modern neutrino physics. The main focus of the neutrino community is on three main topics: the measurement of neutrino mass, the search for neutrinoless double beta decay (which is also related to neutrino mass), and the search for charge-parity (CP) violation. Each of these topics will be discussed below. Current and future sterile neutrino searches will also be discussed.

#### Direct Neutrino Mass Measurements

We have an upper limit on the neutrino mass from measurements, and we know neutrinos are not massless because they oscillate. We do not, however, have a measured value for the neutrino mass. One way to search for the mass of an electron neutrino is to look for the missing energy that the neutrino takes away in a beta decay reaction. Experiments looking at the beta decay of tritium have given us our most stringent upper limit on neutrino mass using this method, the most notable being

from the Mainz collaboration with a limit of  $m_{\nu_e} < 2.3$  eV [49] and from the Troitsk collaboration with a limit of  $m_{\nu_e} < 2.2$  eV [50].

An experiment which has an improved detector setup is under construction and is scheduled to begin taking data 2015. This experiment is called KATRIN and the expected sensitivity is  $\sim 0.2$  eV [51].

### **Neutrinoless Double Beta Decay Measurements**

Neutrinoless double beta decay is one of the main physics goals of the SNO+ experiment and so is outlined more thoroughly in section 3.5.

The search for neutrinoless double beta decay is, arguably, the most popular topic in modern neutrino physics. Current or near-future neutrinoless double beta decay experiments exist in Canada, the United States, Japan, and Italy, using a wide range of technologies.

Searching for this process is particularly attractive because it would prove that the neutrino is its own antiparticle, as well as be evidence for lepton number violation. Neutrinoless double beta decay also has some sensitivity to the measurement of absolute neutrino mass. For a more detailed description of this, see Section 3.5.

### **CP Violation**

The question of a CP violating phase in neutrino oscillations is another area of intensive research in neutrino physics. A CP transformation occurs when you perform a parity transformation, followed by a charge conjugation. CP violation has been observed in neutral kaons and B mesons [47], but has yet to be observed in the lepton

sector. If CP violation is observed in neutrinos, it could account for the matter-antimatter asymmetry in the universe.

### **Solar Neutrinos**

There are still some open questions in the comparatively well-studied field of solar neutrinos. Direct measurements have yet to be made of neutrinos from the thermonuclear CNO cycle in the Sun. Also, the transition region between low energy solar neutrinos, which are not affected by matter effects, and high energy solar neutrinos, which are very affected by matter, have not been well studied. Solar neutrinos are a physics goal for SNO+ and so will be further discussed in Section 3.5. Super-Kamiokande, is currently taking solar neutrino data mainly to better characterize the oscillation behaviour near their low-energy limit as this is beginning to approach the transition region [38]. Super-Kamiokande also is aiming to measure any asymmetry between day and night neutrino detection rates, which is a probe for neutrino interactions with matter [52]. Borexino, which has been very successful as a detector for measuring low energy solar neutrinos, is also still currently taking data. Borexino has recently reported first measurements of two types of solar neutrinos:  ${}^7\text{Be}$  neutrinos [53] and pep neutrinos [54].

### **Search for Sterile Neutrinos**

The search for mixing between active and sterile neutrino flavours is ongoing. A proposed extension of the Borexino experiment, SOX, is planning to probe for sterile neutrinos using a  ${}^{51}\text{Cr}$  source [55]. This chromium source would be a very strong source of neutrinos, which could be deployed in an existing tunnel next to the Borexino

detector. If there exists a sterile neutrino with a  $\Delta m^2$  of  $\sim 1\text{eV}$ , then the oscillation length should be on the order of a meter, which would be visible in the Borexino detector. In a future phase, a  $^{144}\text{Ce}$  source, which emits anti-neutrinos, could also be deployed.

New experiments are being constructed near nuclear reactors to provide more information on the reactor neutrino anomaly. Nucifer [56] is an operational experiment located 7 meters from the core of a reactor. Nucifer plans to measure the overall number of neutrinos to see if there is a deficit from the number expected, which could suggest some active neutrinos are oscillating into sterile neutrinos. Furthermore, since the oscillation behaviour into sterile neutrinos should be energy dependent, Nucifer will look at the rate as a function of neutrino energy to characterize the nature of possible sterile oscillations.

In the solar neutrino sector, Super-Kamiokande is still taking measurements and will perhaps reduce the uncertainty of their low energy region [38] which is most sensitive to sterile neutrinos with a mass on the order of the active neutrinos. SNO+ will be particularly well suited to probe for light sterile neutrinos in the solar sector. This will be the main focus of Chapter 5.

## 2.3 The Standard Solar Model

The standard solar model refers to a model that predicts solar properties, including solar neutrino quantities. These models are generated every few years with updated measurements and modelling techniques. For the purposes of this thesis, we will only consider the solar model that was compiled in 2005, called BS05(OP) [57]. The model used new opacity measurements and was the last model produced by John Bahcall.

The main inputs into the standard solar model are the heavy metal abundances, radiative opacities, and nuclear reaction rates, as well as the main properties of the Sun such as solar mass, luminosity, and radius.

This section will describe those key quantities predicted by the model, namely the neutrino production zones, the electron and neutron densities in the Sun, and the total expected neutrino flux for each neutrino type. These values will be used in Chapter 5 when the propagation of the neutrino through the Sun is calculated numerically.

### 2.3.1 Neutrino Production Zones in the Sun

The production zones vary for different neutrino types. Figure 2.1 depicts the production profiles for each neutrino type. As seen here, the neutrinos are produced in the inner third of the Sun.

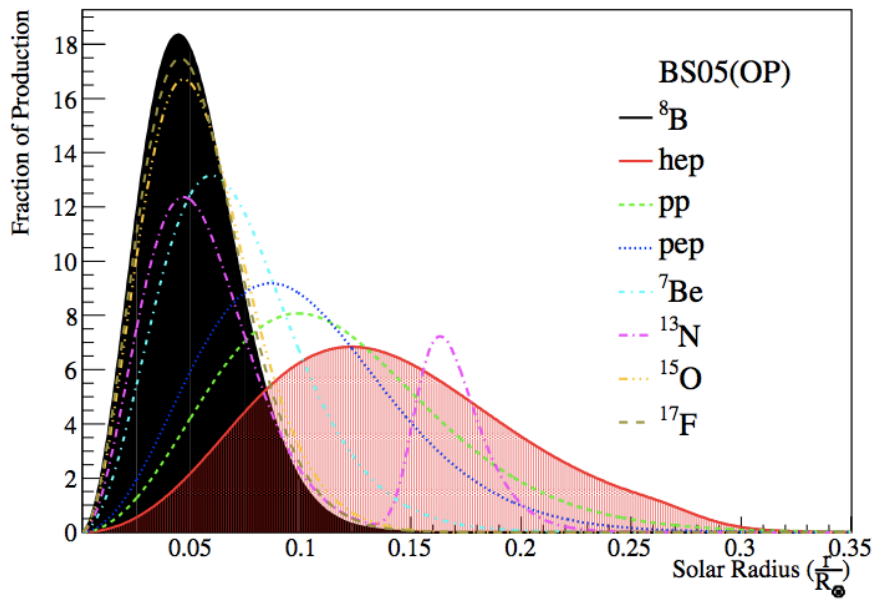


Figure 2.1: Neutrino production regions in the Sun. [58]

### 2.3.2 Electron and Neutron Density Profiles

Figure 2.2 shows the electron and neutron densities given by BS05(OP).

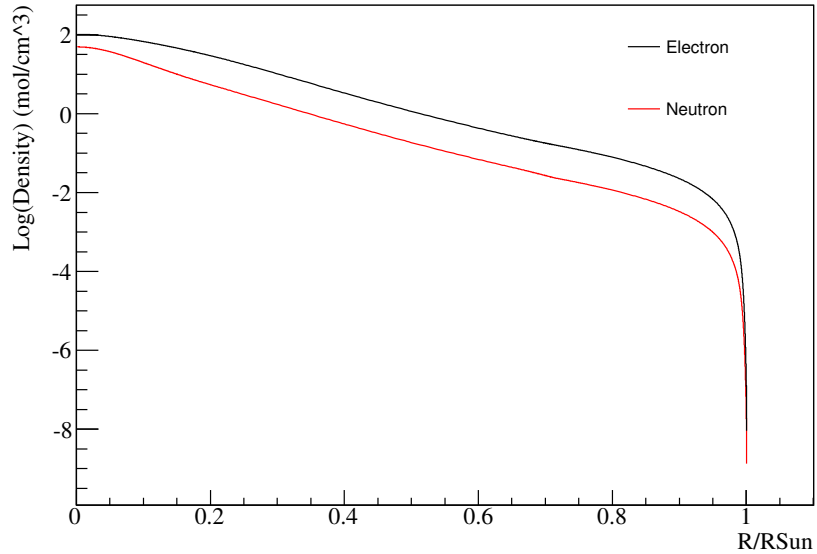


Figure 2.2: Electron (black line) and neutron (red line) density profiles in the Sun from BS05(OP).

### 2.3.3 Predicted Neutrino Fluxes

Table 2.1 shows the predicted fluxes of each type of solar neutrino in the BS05(OP) solar model. The uncertainties on each of the flux values are also quoted.

pp neutrinos have the highest flux and the smallest uncertainty, but their low energy makes them harder to detect. pep neutrinos also have a relatively low uncertainty and SNO+ plans to make a measurement of this neutrino type. hep neutrinos have a very low overall flux and have not yet been directly measured.  ${}^7\text{Be}$  neutrinos have a relatively high flux, but a relatively large uncertainty.  ${}^8\text{B}$  neutrinos have a relatively low flux and a relatively high uncertainty, but since they have a higher

end point energy background reduction is more feasible and thus they are easier to measure. These neutrinos have been studied by water Cherenkov experiments.

Table 2.1: Predicted Solar Neutrino Fluxes from BS05(OP) [57]

Source	Flux ( $\text{cm}^{-2} \text{s}^{-1}$ )	Uncertainty (%)
pp	$5.99 \times 10^{10}$	1
pep	$1.42 \times 10^8$	2
hep	$7.93 \times 10^3$	16
${}^7\text{Be}$	$4.84 \times 10^9$	10.5
${}^8\text{B}$	$5.69 \times 10^6$	16
${}^{13}\text{N}$	$3.07 \times 10^8$	36
${}^{15}\text{O}$	$2.33 \times 10^8$	40
${}^{17}\text{F}$	$5.84 \times 10^6$	44

## 2.4 (Active) Neutrino Oscillations

Solar neutrinos are affected by two different oscillation effects, referred to as vacuum oscillations and matter oscillations. Vacuum oscillations refer to the quantum mechanical oscillations generated by the interference of different massive neutrino eigenstates. The mathematics of vacuum oscillations will be the focus of Section 2.4.1. Matter oscillations, which are discussed in Section 2.4.2, describe the modified oscillation probability due to charged current and neutral current interactions with particles in a medium. Vacuum oscillations are the dominant effect for solar neutrinos that are very low in energy, while matter oscillations dominate the higher energy region. For neutrinos which pass through matter of changing density, there can be a further enhancement called the MSW effect, which will be described in Section 2.4.3.

### 2.4.1 Vacuum Oscillations for Active Neutrinos

The fact that neutrinos oscillate makes for an interesting mathematical framework. Unlike other leptons, the flavour eigenstate is not a direct mapping to the mass eigenstate. So, for example, an electron neutrino is not composed of a single mass eigenstate, but is a linear combination of mass eigenstates that are related to each other by the degree to which these eigenstates mix. This mixing is described by the mixing angles. The equation for the relation between the flavour basis and the mass eigenstate basis can be seen in equation 2.5. Equations for vacuum oscillations are taken from [47].

$$\nu_\alpha = \sum_{k=1}^3 U_{\alpha k} \nu_k \quad (2.5)$$

In equation 2.5, the matrix  $U$  is introduced. Here,  $\alpha$  is a flavour eigenstate (e,  $\mu$ ,  $\tau$ ) and  $k$  is a mass eigenstate (1,2,3).  $U$  is a rotation matrix that describes the mixing of neutrino mass eigenstates.  $U$  is known as the Pontecorvo-Maki-Nakagawa-Satake (PMNS) matrix and it is shown explicitly using the common parameterization [36] in equation 2.6.

$$U \equiv U^D D^M \quad (2.6)$$

where

$$U^D = \begin{pmatrix} c_{12}c_{13} & s_{12}c_{13} & s_{13}e^{-i\delta_{13}} \\ -s_{12}c_{23} - c_{12}s_{23}s_{13}e^{i\delta_{13}} & c_{12}c_{23} - s_{12}s_{23}s_{13}e^{i\delta_{13}} & s_{23}c_{13} \\ s_{12}s_{23} - c_{12}c_{23}s_{13}e^{i\delta_{13}} & -c_{12}s_{23} - s_{12}c_{23}s_{13}e^{i\delta_{13}} & c_{23}c_{13} \end{pmatrix} \quad (2.7)$$

and

$$D^M = \begin{pmatrix} 1 & 0 & 0 \\ 0 & e^{i\frac{\lambda_{21}}{2}} & 0 \\ 0 & 0 & e^{i\frac{\lambda_{31}}{2}} \end{pmatrix} \quad (2.8)$$

The PMNS matrix contains three mixing angles ( $\theta_{12}$ ,  $\theta_{23}$ , and  $\theta_{13}$ ) and up to three CP violating phases ( $\delta$  and  $\lambda_i$ ). Here,  $c_{ab} \equiv \cos\theta_{ab}$  and  $s_{ab} \equiv \sin\theta_{ab}$ ,  $\delta_{13}$  is the Dirac CP violating phase, and  $\lambda_{21}$  and  $\lambda_{31}$  are the Majorana CP violating phases which are non-zero only if the neutrino is a Majorana particle.

The PMNS matrix is related to survival probability in the vacuum oscillations case through equation 2.9, where  $\alpha$  is the neutrino flavour ( $e$ ,  $\mu$ ,  $\tau$ ) at the time of production,  $\beta$  is a neutrino flavour detected some time later,  $k$  and  $j$  are neutrino mass eigenstates,  $L$  is the distance between the neutrino source and the detector,  $E$  is neutrino energy, and  $\Delta m_{kj}^2$  is the mass squared differences between neutrino mass eigenstates  $k$  and  $j$  (explicitly,  $\Delta m_{kj}^2 \equiv m_k^2 - m_j^2$ ).

$$P_{\nu_\alpha \rightarrow \nu_\beta}(L, E) = \sum_{k>j} U_{\alpha k}^* U_{\beta k} U_{\alpha j} U_{\beta j}^* \sin^2\left(\frac{\Delta m_{kj}^2 L}{4E}\right) \quad (2.9)$$

For the case where the neutrino flavour that is created is the same as the one

detected, the equation simplifies to equation 2.10.

$$P_{\nu_\alpha \rightarrow \nu_\alpha}(L, E) = 1 - 4 \sum_{k>j} |U_{\alpha k}|^2 |U_{\alpha j}|^2 \sin^2\left(\frac{\Delta m_{kj}^2 L}{4E}\right) \quad (2.10)$$

Using equation 2.10, we can define an electron neutrino survival probability ( $P_{ee}$ ) for the case of vacuum oscillations. This equation is particularly valuable because all solar neutrinos are created as electron type neutrinos, so  $P_{ee}$  is the probability that a neutrino created in the Sun is detected as an electron neutrino when it arrives at the detector. This is shown in equation 2.11. The electron neutrino survival probability will be referred to often in this thesis, sometimes just as survival probability or  $P_{ee}$ .

$$P_{ee} = 1 - 4 \sum_{k>j} |U_{ek}|^2 |U_{ej}|^2 \sin^2\left(\frac{\Delta m_{kj}^2 L}{4E}\right) \quad (2.11)$$

### 2.4.2 Matter Oscillations for Active Neutrinos

As the neutrinos pass through the vacuum, their oscillation behaviour is defined only by the mixing between the eigenstates. As neutrinos pass through matter, there is an additional effect in the form of coherent forward elastic scattering. These reactions can be charged current reactions, as seen in figure 2.3a or neutral current reactions, as seen in figure 2.3b. Equations which describe the neutrino interactions with matter, as taken from [47], are given here.

The potential term for the charged current reaction ( $V_{CC}$ ) is shown in equation 2.12 and the potential for neutral current reactions ( $V_{NC}$ ) is shown in 2.13.

$$V_{CC} = \sqrt{2}G_f N_e \quad (2.12)$$

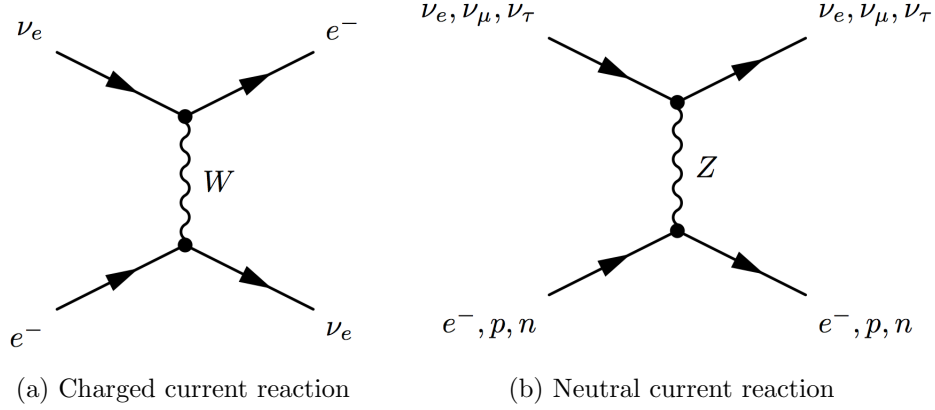


Figure 2.3: The Feynman diagrams for the elastic scattering interactions with matter. [47]

$$V_{NC} = -0.5\sqrt{2}G_f N_n \quad (2.13)$$

The charged current potential in equation 2.12 is dependent on the Fermi constant  $G_f$  and the electron density  $N_e$ . The neutral current potential in equation 2.13 is in principle dependent on protons, electron, and neutron densities, though the effect of the protons and electrons negate each other and so the overall term is only dependent on the neutron density  $N_n$ .

We can construct an equation for how neutrinos propagate in matter, as seen in equation 2.14. The propagation equation for neutrinos in matter is not just related to the mixing of the neutrinos themselves, but is also related to the properties of the matter being traversed. The neutral current potential has disappeared from the final

equation because it affects all three neutrino types and so can be ignored.

$$i \frac{d}{dt} \begin{pmatrix} \nu_e \\ \nu_\mu \\ \nu_\tau \end{pmatrix} = (UmU^* + V) \begin{pmatrix} \nu_e \\ \nu_\mu \\ \nu_\tau \end{pmatrix} \quad (2.14)$$

where

$$V = \begin{pmatrix} V_{cc} & 0 & 0 \\ 0 & 0 & 0 \\ 0 & 0 & 0 \end{pmatrix} \quad (2.15)$$

When looking at neutrinos going through matter, it is helpful to define a matter basis where the Hamiltonian in matter is diagonalized. To simplify the equations, we will consider two neutrino mixing where there are only eigenstates  $\nu_1$  and  $\nu_2$ , two flavour eigenstates  $\nu_e$  and  $\nu_\tau$ , and thus where there is a mixing angle  $\theta$  and a mass squared difference of  $\Delta m^2$ . While this is an approximation, this simplification models the case of solar neutrinos quite well. If we explicitly write out the Hamiltonian from equation 2.14, we see that the main term in the Hamiltonian in the flavour basis,  $H_f$  is

$$H_f = (UmU^* + V) = \frac{1}{4E} \begin{pmatrix} -\Delta m^2 \cos 2\theta + 2EV_{cc} & \Delta m^2 \sin 2\theta \\ \Delta m^2 \sin 2\theta & \Delta m^2 \cos 2\theta - 2EV_{cc} \end{pmatrix}. \quad (2.16)$$

If we want to rotate from the flavour basis into the matter flavour basis, we will

introduce a rotation by an angle  $\theta_m$  of the form

$$H_m = U_m^T H_f U_m \quad (2.17)$$

where

$$U_m = \begin{pmatrix} \cos \theta_m & \sin \theta_m \\ -\sin \theta_m & \cos \theta_m \end{pmatrix}. \quad (2.18)$$

When we consider a neutrino propagating in matter, we can diagonalize the Hamiltonian. Now we get a redefined Hamiltonian in the matter flavour basis where,

$$i \frac{d}{dt} \begin{pmatrix} \nu_e^m \\ \nu_a^m \end{pmatrix} = H_m \begin{pmatrix} \nu_e^m \\ \nu_a^m \end{pmatrix} \quad (2.19)$$

and the new main term in the Hamiltonian becomes

$$H_m = \frac{1}{4E} \begin{pmatrix} -\Delta m_m^2 & 0 \\ 0 & \Delta m_m^2 \end{pmatrix}. \quad (2.20)$$

We have defined the entries on the diagonal of  $H_m$  as the effective mass splitting in the matter basis,  $\Delta m_m^2$ , shown explicitly in equation 2.21 where  $\Delta m^2 \equiv m_2^2 - m_1^2$ . If  $m_2^2$  is larger than  $m_1^2$ , then  $\Delta m^2$  will be positive, whereas if  $m_1^2$  is larger this term will be negative. The angle that was required to rotate from the flavour basis to this new matter basis is the effective mixing angle in matter,  $\theta_m$ , and is defined in equation 2.22.

$$\Delta m_m^2 = \sqrt{(\Delta m^2 \cos 2\theta - 2EV_{cc})^2 + (\Delta m^2 \sin 2\theta)^2} \quad (2.21)$$

$$\tan 2\theta_m = \frac{\tan 2\theta}{1 - \frac{2EV_{cc}}{\Delta m^2 \cos 2\theta}} \quad (2.22)$$

Finally, it is sometimes helpful to see the evolution equation in the mass eigenstate basis. Using equations 2.23 and 2.24, we can derive the Hamiltonian in the mass basis which is shown in equation 2.25.

$$\begin{pmatrix} \nu_e^m \\ \nu_a^m \end{pmatrix} = U_m \begin{pmatrix} \nu_1^m \\ \nu_2^m \end{pmatrix} \quad (2.23)$$

$$i \frac{d}{dt} \begin{pmatrix} \nu_e^m \\ \nu_a^m \end{pmatrix} = i \frac{dU_m}{dt} \begin{pmatrix} \nu_1^m \\ \nu_2^m \end{pmatrix} + iU_m \frac{d}{dt} \begin{pmatrix} \nu_1^m \\ \nu_2^m \end{pmatrix} \quad (2.24)$$

$$i \frac{d}{dt} \begin{pmatrix} \nu_1^m \\ \nu_2^m \end{pmatrix} = \begin{pmatrix} -\Delta m_m^2 & -4Ei \frac{d\theta_m}{dt} \\ 4Ei \frac{d\theta_m}{dt} & \Delta m_m^2 \end{pmatrix} \begin{pmatrix} \nu_1^m \\ \nu_2^m \end{pmatrix}. \quad (2.25)$$

### 2.4.3 The MSW Effect

In 1985, Mikheyev and Smirnov [59] introduced an effect which could account for the efficient conversion of electron neutrinos in the Sun to other flavour types. Since this idea was based on previous work from Wolfenstein [60], this was referred to as the MSW effect. Again, the derivations in this section are from [47].

Following from equation 2.22, it can be shown that if  $\Delta m$  is positive, for large energy and electron density  $\theta_m$  is  $90^\circ$ . From equation 2.23, we can write equation 2.26. From equation 2.26 we see the implication of  $\theta_m = 90^\circ$  is that electron neutrinos created at high energies (approximately  $>10$  MeV) and at high electron densities will be almost completely in the  $\nu_2$  state. Since the transition through the Sun

occurs adiabatically, the neutrinos will emerge in the  $\nu_2$  state and will have a lower probability of being detected on Earth as an electron neutrino than simple vacuum oscillations or effects related to the modified potentials in matter would suggest.

$$\nu_e = \cos \theta_m \nu_1 + \sin \theta_m \nu_2 \quad (2.26)$$

In the MSW effect there is also a concept of a resonance condition which makes the denominator of equation 2.22 equal to zero. This condition is shown in equation 2.27. At the resonance condition,  $\theta_m = 45^\circ$  and so neutrinos produced at an energy and electron density which exactly satisfied this condition would be equally produced in the  $\nu_1$  and  $\nu_2$  state.

$$2\sqrt{2}E_\nu G_F N_e = \Delta m^2 \cos 2\theta \quad (2.27)$$

In practice, this resonance condition represents the transition region between  $\theta_m = 90^\circ$  and  $\theta_m = \theta$ . The critical energy for the resonance condition,  $E_{\nu_{crit}}$ , occurs when equation 2.28 is satisfied. Here,  $N_e^{centre}$  is the electron density in the center of the Sun. Neutrinos which are much higher than this energy will be almost completely in the  $\nu_2$  state as previously described. Neutrinos which are much lower than this energy will be produced with  $\theta_m \sim \theta$  and will not see this enhancement from the MSW effect. Neutrinos between these two energy extremes will see some effect on their oscillation behaviour since  $\theta_m$  will be larger than  $\theta$ . The numerical value of equation 2.28, using measured solar parameters  $\Delta m_{21}^2 = 7.50 \times 10^{-5}$  and  $\sin^2(2\theta_{12})$

= 0.857 [36], is approximately 1.5 MeV.

$$E_{\nu_{crit}} = \frac{\Delta m^2 \cos 2\theta}{2\sqrt{2}G_F N_e^{centre}} \quad (2.28)$$

As stated previously, equation 2.27 relies on the fact that  $\Delta m^2$  and  $\cos 2\theta$  are positive, because in matter  $N_e$  is positive and  $\cos 2\theta$  is positive by convention. This has profound implications on the hierarchy of the neutrino mass eigenstates  $m_1$  and  $m_2$ . As a reminder,  $\Delta m^2 = \Delta m_{21}^2 = m_2^2 - m_1^2$ . Vacuum oscillations, after averaging, can only give a survival probabilities which are greater than 0.5. SNO measured the survival probability of the  $^8\text{B}$  solar neutrinos to be less than 0.5, which can only be possible if the MSW effect is included. Therefore,  $\Delta m^2$  must be positive, which implies  $m_2^2 > m_1^2$  [47].

A graphical depiction of what happens to the neutrino flavour at the resonance condition is shown in Figure 2.4. In this plot,  $\rho$  is the electron density and  $\Delta m^2$  is the effective mass splitting in the matter basis as described by equation 2.21. For antineutrinos, the effective sign of the matter potential is negative, and so a resonance condition is never met.

All neutrinos are produced in an electron flavour state near the centre of the Sun (which has a high electron density, called  $\rho$  in this figure). When both the neutrino energy and the electron density is high, the right hand side of equation 2.22 is small, which is satisfied when  $\theta_m$  is  $\sim 90^\circ$ , and so from equation 2.26 we know that the electron neutrinos which are high in energy ( $> 10$  MeV) almost completely correspond to the  $\nu_2$  state. We also know that  $\nu_2$  is the higher mass eigenstate and so when the neutrino is produced in the Sun, it is on the upper curve at high  $\rho$ . As the electron density drops, the effective neutrino mass follows equation 2.21 which is

proportional to the electron density.

The resonant condition is represented by the region on the plot where the  $\nu_1$  and  $\nu_2$  curves are the closest. At the resonant condition, the diagonal terms in the Hamiltonian in equation 2.25 are at the minimum value and if the off-diagonal terms ( $4Ei\frac{d\theta_m}{dx}$ ) were large they could generate mixing between the  $\nu_2^m$  and  $\nu_1^m$  states. In the Sun, the electron density changes slowly, and so these off-diagonal terms are small. Thus, the solar neutrino, which was mostly in the  $\nu_2^m$  state when it was produced, will continue to propagate as a  $\nu_2^m$  state. At resonance,  $2EV_{cc} = \Delta m^2 \cos 2\theta$ , and so the right hand term in equation 2.22 approaches infinity, which is satisfied by  $\theta_m = 45^\circ$ . Thus, the neutrino is now an even admixture of electron and muon type neutrinos.

Once past the resonance region,  $\theta_m$  continues to decrease until the electron density approaches zero at the edge of the Sun. As the neutrino exits the Sun, the  $\nu_2^m$  eigenstate is now aligned with the  $\nu_2$  state.

The phase averaged survival probability equation for neutrinos which propagate adiabatically through the Sun and where the distance between the neutrino source and detector is large, is shown in equation 2.29, where  $\theta_m^i$  is the effective matter mixing angle where the neutrino is produced.

$$P_{ee}^{adiabatic} = \frac{1}{2} + \frac{1}{2} \cos 2\theta_m^i \cos 2\theta \quad (2.29)$$

## 2.5 Solar Neutrino Propagation (In Words)

Section 2.4 introduces the equations which describe neutrino oscillations through vacuum and matter. In this section, a more colloquial description will be given of the effects the neutrino encounters from production until detection.

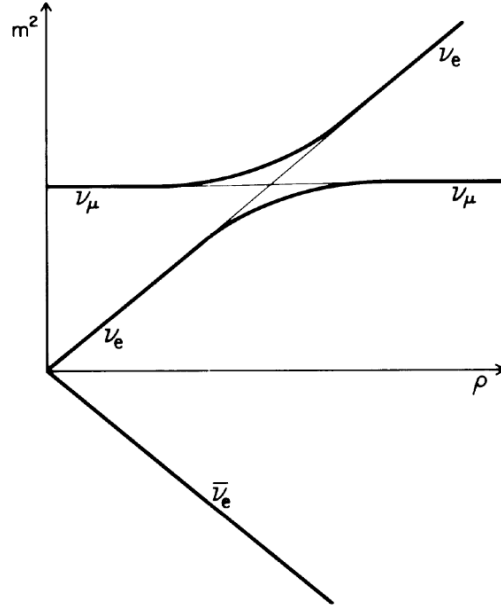


Figure 2.4: Level crossing diagram which shows the propagation of neutrinos which are affected by the MSW effect. This shows the neutrino mass as a function of electron density in the Sun,  $\rho$  [61].

Electron neutrinos are produced near the centre of the Sun in the production regions which are depicted in figure 2.1. How the neutrino propagates through the Sun is dependent on the energy of the neutrino. Three cases are described below.

For neutrinos which are lower in energy than equation 2.28, the matter does not have a large effect on the oscillation behaviour and so the matter terms in equation 2.14 offer only small corrections to the vacuum oscillation case. Neutrinos in this energy region are in what is referred to as the vacuum-dominated region. This is shown in the bottom panel of figure 2.5.

For neutrinos which are high in energy ( $E > 10$  MeV), the MSW effect strongly affects the propagation of the neutrino. The neutrino is still produced as an electron type, but this almost completely corresponds to a  $\nu_2$  neutrino type since  $\theta_m$  is  $\sim$

$90^\circ$  at high densities and high neutrino energy. As it propagates through the Sun, the neutrino will reach a resonance region where the likelihood that the  $\nu_2^m$  matter state will transition to a  $\nu_1^m$  state is the highest. Because the electron density in the Sun changes smoothly, transitions between  $\nu_2^m$  and  $\nu_1^m$  states will not occur, and thus the neutrino emerges from the Sun in the  $\nu_2^m$  state. Because the electron density approaches zero at the surface of the Sun, the  $\nu_2^m$  state corresponds to the more familiar  $\nu_2$  state. For solar neutrinos with  $E > 10$  MeV, only about 30 % of neutrinos detected on Earth will be electron flavour. This neutrino energy region is called the matter-dominated region. This case is shown in the top panel of figure 2.5.

In the last case, we will consider a neutrino which has an intermediate energy (roughly between 1 MeV and 10 MeV). The effective mixing angle  $\theta_m$  now does not fully translate into the  $\nu_2$  state and the electron neutrino will propagate as an admixture of the  $\nu_1$  state and the  $\nu_2$  state. As the neutrino propagates, it may encounter a resonance region. The neutrino will emerge from the Sun as an admixture of  $\nu_1$  and  $\nu_2$  eigenstates. This neutrino energy region is referred to as the transition region. This case is represented by the middle panel of figure 2.5.

## 2.6 The Electron Neutrino Survival Probability

A plot of the electron neutrino survival probability curve, as shown in figure 2.6, is a good way to visually summarize the effects which are discussed in this chapter.

As previously defined, the electron neutrino survival probability, also known as  $P_{ee}$ , is the probability that an electron neutrino from the Sun is measured as an electron neutrino when it reaches the detector. At the low energies, this is described by equation 2.11. At high energies, this is described by equation 2.29.

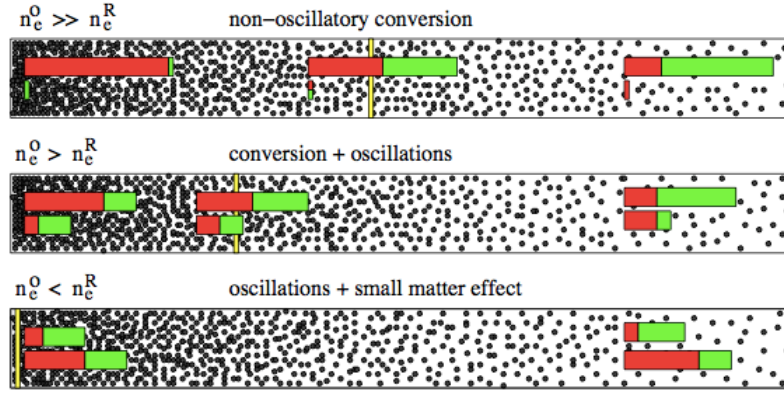


Figure 2.5: The three cases of neutrino propagation, as taken from [62]. The density of the black dots are representative of the electron density.  $n_e^O$  refers to the electron density where the neutrino was produced and  $n_e^R$  refers to the electron density at the resonance for that neutrino energy. The yellow lines represent where the resonance occurs. The red and green coloured bars depict the proportion of the electron flavour (red) and muon flavour (green) in the  $\nu_2$  (top) and  $\nu_1$  (bottom) states. The top panel represents a neutrino in the matter dominated region, the middle panel represents a neutrino in the transition region, and the bottom panel shows a neutrino which is in the vacuum dominated region.

As shown in figure 2.6, there is a plateau in the  $P_{ee}$  values at very low energies because vacuum oscillation is the dominant effect. Similarly, there is a plateau in  $P_{ee}$  for higher energy neutrinos because the matter effects dominate the behaviour in this region. There is also a transition region where the value of  $P_{ee}$  changes quickly with energy. In this energy region the behaviour is determined by a combination of matter effects and oscillation effects. As seen in figure 2.6, the neutrinos with the lowest energies and thus in the vacuum oscillation dominated region have a  $P_{ee}$  of  $\sim 0.55$ . Neutrinos with high energy, in the matter oscillation dominated region, have a  $P_{ee}$  of  $\sim 0.3$ . Neutrinos which are intermediate in energy, in the so-called transition region, have  $P_{ee}$  values ranging from 0.55 to 0.3.

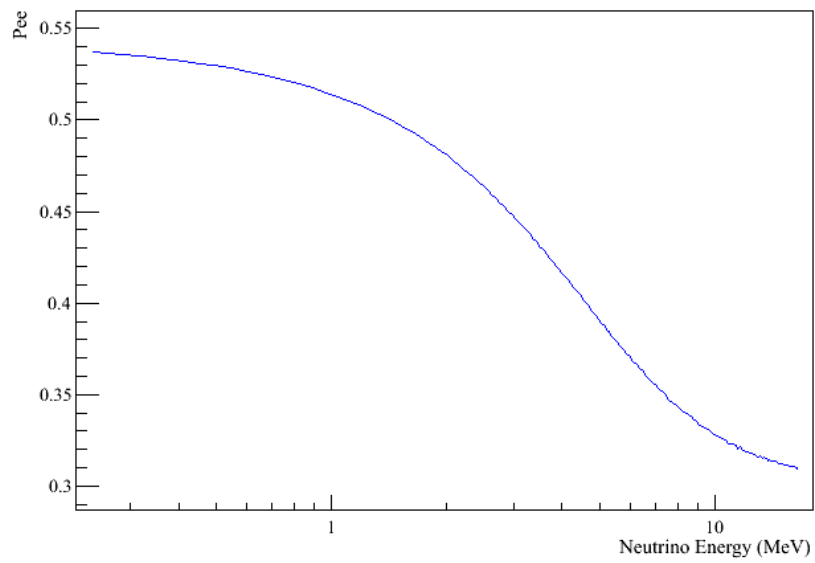


Figure 2.6: Survival probability of a solar electron neutrino,  $P_{ee}$ , as a function of neutrino energy for a  ${}^8\text{B}$  neutrino averaged over the production region. The low energy plateau in  $P_{ee}$  is the vacuum dominated region. The high energy plateau in  $P_{ee}$  is the matter dominated effect.

# Chapter 3

## The SNO+ Experiment

The SNO+ experiment will attempt to answer some of the open questions in neutrino physics that were introduced in Section 2.2.2. This chapter will describe the details of the hardware and software for the experiment. Section 3.1 will give a brief description of SNOLAB, where SNO+ is housed. Section 3.2 discusses the SNO detector, which is the predecessor of the SNO+ experiment. Much of the hardware from the SNO detector is being reused in SNO+ and so describing SNO gives context to the modifications SNO+ is performing as described in Section 3.3. SNO+ will take data in three different modes, which are outlined in Section 3.4. The physics goals of SNO+ are discussed in Section 3.5. The final section in this chapter, Section 3.6, outlines the major backgrounds for each phase of the SNO+ experiment, which motivates the background mitigation techniques that are the focus of Chapter 4.

## 3.1 SNOLAB

The SNO+ experiment is located in the SNOLAB facility. SNOLAB is an underground physics laboratory located just outside of Sudbury, Ontario, Canada. SNOLAB operates at Vale's Creighton nickel mine and consists of both a facility on the surface of the mine property, and an underground laboratory space which is 6800 feet below the surface. The underground space is a class 2000 clean facility, which means that there are less than 2000 particles that are  $0.5 \mu\text{m}$  or larger in diameter per cubic meter of air. SNOLAB is home to many different astroparticle detectors, mostly related to neutrino or dark matter detection.

## 3.2 The SNO Detector

To introduce the SNO+ experiment, it is helpful to first describe the predecessor experiment, SNO. SNO was introduced briefly in Section 2.1, but the detector hardware will be explained in more detail here.

The SNO experiment was the original project that was housed at the SNOLAB location. As mentioned in Section 2.1, SNO was built with the intention of solving the solar neutrino problem, where less neutrinos were measured coming from the Sun than the theoretical model predicted.

A diagram of the SNO detector is shown in Figure 3.1. Details of SNO's latest results can be found in [37], and a comprehensive description of the detector can be found in [63]. SNO consisted of a 12 metre diameter spherical acrylic vessel (AV) which housed 1 kilotonne of heavy water ( $^2\text{H}_2\text{O}$  or  $\text{D}_2\text{O}$ ). Neutrinos interacted with the  $\text{D}_2\text{O}$  and created Cherenkov light, which was viewed by the 9456 20cm Hamamatsu

photomultiplier tubes (PMTs) that surrounded the AV. The PMTs were affixed to a stainless steel, geodesic photomultiplier support structure (PSUP). Surrounding the AV was a light water ( $\text{H}_2\text{O}$ ) shielding, with 1.7 kilotonnes of light water contained between the AV and the PSUP, and an additional 5.7 kilotonnes contained between the PSUP and the cavity walls. The light water outside of the PSUP was viewed by 91 outward looking 20cm Hamamatsu PMTs, which served to reject external background events in the detector volume.

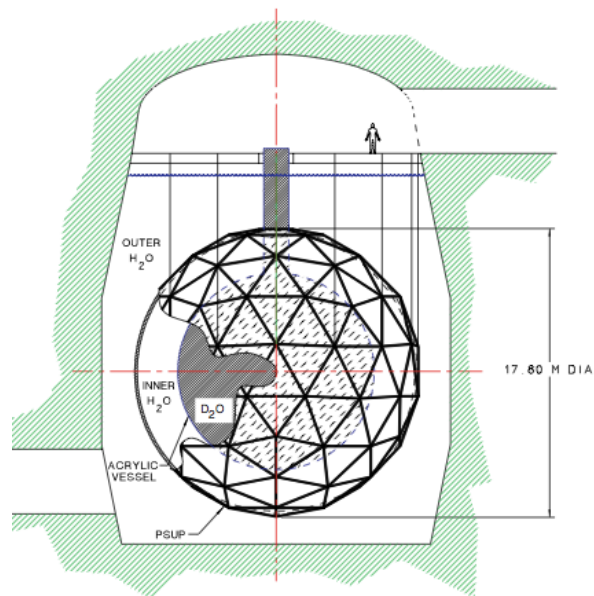


Figure 3.1: A schematic of the SNO Detector. [63]

### 3.3 Transitioning from SNO to SNO+

When the SNO detector finished taking data in November 2006, there was an opportunity to refurbish the detector to achieve new physics goals. This led to the formation of the SNO+ collaboration. The specific physics goals of SNO+ are the

measurement of lower energy solar neutrinos, neutrinoless double beta decay, reactor and geoneutrinos, supernova neutrinos, and nucleon decay. Some of these physics goals will be more thoroughly described in section 3.5.

SNO+ will keep most of the pre-existing hardware including the AV, PMTs, and PSUP from SNO. However, to adapt to fit the SNO+ agenda a number of changes need to be made to the detector. The most significant change is the replacement of the heavy water in the acrylic vessel with liquid scintillator.

### **Hardware Modifications**

When the acrylic vessel was filled with heavy water it needed to be held up since the heavy water was denser than the surrounding light water. An interesting consequence of the AV now being filled with liquid scintillator is that a system will need to be in place which will hold down the AV since the scintillator is less dense than light water. A system to hold down the vessel which consists of ropes arranged to form a net around the top of the AV has been installed. Figure 3.2 shows the SNO+ detector with the hold down ropes installed.

Material compatibility is an issue because traditionally used scintillators are not compatible with acrylic, which is a concern because the scintillator will be in contact with the AV. Long term tests performed by the Queen's University SNO+ group have indicated that acrylic is compatible with the liquid scintillator that will be used in SNO+ [65, 66].

Due to the higher light yield obtained with liquid scintillator, the electronics also needed to be upgraded to handle the higher event rate. Trigger levels and data storage capacity are two big issues which are being addressed. Because the electronics are

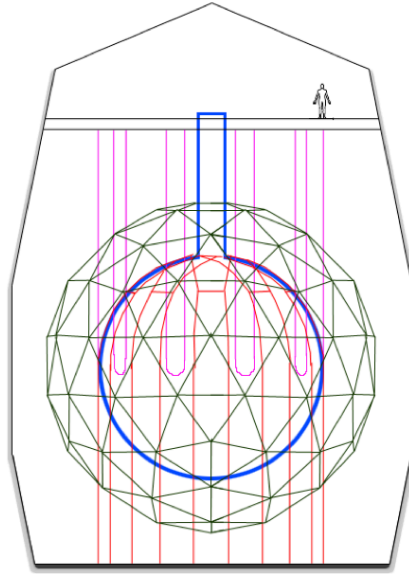


Figure 3.2: A schematic of the SNO+ Detector. The acrylic vessel is drawn in blue. The hold up ropes are shown in purple, while the hold down ropes are red. The PSUP on which the PMTs are mounted is shown in green. [64]

now a number of years old, some repairs are underway to fix the PMTs which have broken down. It is also necessary to clean the electronics that have developed deposits from being underground for an extended period of time.

### Software Modifications

The Monte Carlo code which simulates the detector geometry and optics is getting a complete overhaul from the code used by SNO. While SNO used a FORTRAN based code [67], SNO+ moved to a C++ based code called Reactor Analysis Tools (RAT) in 2006 [64]. This code was originally designed by Stan Seibert for the Braidwood reactor neutrino experiment and has been modified by the SNO+ collaboration to incorporate our detector parameters. RAT uses the Geant4 libraries [68], which contain

particle interaction information, and ROOT libraries [69], which contain mathematical analysis tools. These libraries are updated regularly by CERN. RAT also contains files that are specific to our detector, such as geometry files which simulate the configuration of the SNO+ detector components, and optics files, which contain information such as the index of refraction of detector materials, as well as information about the liquid scintillator such as scattering length and emission timing coefficients. An example of how optical properties, specifically timing coefficients, can be measured on a bench-top experiment and then implemented into RAT, will be discussed in Chapter 4.

### 3.4 SNO+ Run Plan

The SNO+ experiment will have three distinct modes of running, each with their own physics goals. The details of the main physics goals will be more thoroughly described in Section 3.5.

#### **Phase I: Water**

In the water phase, the SNO+ AV volume will be filled with clean H<sub>2</sub>O. The main goals of this phase are understanding of backgrounds in the detector and improving the cleanliness of the detector. Some physics can be extracted in this phase, including a search for nucleon decay.

#### **Phase II: Scintillator**

Next will be the scintillator phase, where SNO+ will fill the AV with liquid scintillator. The main goal of this phase will be to understand the radioactive backgrounds

inherent to the scintillator, as well as alpha backgrounds which are not detectable in the water phase. If the backgrounds are low in this phase, it may be possible to extract low energy solar neutrino data.

### **Phase III: Scintillator + tellurium**

In the neutrinoless double beta decay phase of the experiment,  $^{130}\text{Te}$  will be added to the scintillator. The concentration of the tellurium is expected to be initially around 0.3%. The feasibility of loading up to a concentration of around 3% in future years is currently being investigated, and will depend on the optical properties of the 3% loading, the intrinsic backgrounds in the Te, as well as funding for a larger amount of tellurium.

### **Phase IIb: Scintillator revisited**

After the neutrinoless double beta decay phase is complete, the experiment will remove the tellurium and return to scintillator-only running conditions. The experiment will remove the tellurium by purifying the scintillator, and this will remove radioactive backgrounds in the low energy region as well. SNO+ will then collect more solar neutrino data with lower backgrounds and a longer running time than during the first scintillator phase.

## 3.5 SNO+ Physics Goals

SNO+ will be a multipurpose neutrino experiment. The physics aims for SNO+ include the search for the elusive process of neutrinoless double beta decay, the measurement of low energy solar neutrinos, and the detection of reactor [70] and geoneutrinos [71]. If a galactic supernova occurs during the lifetime of SNO+, the detected neutrinos from the event will give insight into supernova explosions [72]. During the water phase of the experiment, the main physics activity will be a search for invisible mode nucleon decay [73].

For the purpose of this thesis, only neutrinoless double beta decay and low energy solar neutrinos will be discussed. Neutrinoless double beta decay is the main science goal for SNO+ and so a discussion of this rare process will give insight into the primary activities of the experiment. Solar neutrinos are another important physics goal of the experiment, and the main focus of Chapter 5, and so we will examine the details of this physics goal to give context to work covered later in this thesis. For more information on any of the other SNO+ physics goals, refer to the references above.

### 3.5.1 Neutrinoless double beta decay

One of the most important topics in neutrino physics is the determination of neutrino mass. From previous experiments, the mass squared difference between neutrino mass eigenstates are known, however there exists no absolute measurement of these masses. In addition to determining an absolute neutrino mass scale, it is also of interest to classify neutrinos as Dirac or Majorana particles. The most promising way of answering these questions is by observing the theoretically proposed process

of neutrinoless double beta decay.

### A brief introduction to neutrinoless double beta decay

Double beta decay (Equation 3.1) occurs when it is energetically forbidden for a nucleus to undergo single beta decay, or when single beta decay is forbidden due to angular momentum selection rules. Double beta decay is the process by which two neutrons in a nucleus are converted to two protons, two electrons, and two antineutrinos. This process has been observed for a number of isotopes and is allowed in standard model physics. Neutrinoless double beta decay (Equation 3.2) is a proposed reaction by which the two neutrons in the nucleus convert to two protons and two electrons, but no neutrinos are emitted. This reaction would violate lepton number conservation rules.



Observing neutrinoless double beta decay would have a profound impact on our understanding of the fundamental nature of the neutrino. If no neutrinos were emitted from the double beta decay process, this would imply that the neutrinos annihilated each other. This would prove that the neutrino is a Majorana particle, and thus its own antiparticle.

In addition to determining that the neutrino is a Majorana particle, the observation of neutrinoless double beta decay would give insight into the absolute mass scale of the neutrino. The half life of the neutrinoless double beta decay process,  $T^{0\nu\beta\beta}$ ,

is proportional to the effective Majorana mass ( $m_{2\beta}$ ), as seen in Equation 3.3 [74]. Here, the absolute mass scale of the neutrino is related to the sum of the mass eigenstates as in Equation 3.4 [47], where  $m_k$  is the mass of the neutrino mass eigenstate  $k$  and  $U_{ek}^2$  is the neutrino mixing amplitudes given by Equation 2.6. Equation 3.3 is also dependent on the mass of the electron,  $m_e$ , the phase space factor  $G^{0\nu}$ , which scales with the Q value of the reaction and can be accurately calculated, and the nuclear matrix element  $M^{0\nu\beta\beta}$ , which has a large uncertainty due to different models producing different results [74].

$$(T^{0\nu\beta\beta})^{-1} = G_{0\nu} |M^{0\nu\beta\beta}|^2 \left( \frac{|m_{2\beta}|}{m_e} \right)^2 \quad (3.3)$$

$$m_{2\beta} = \sum_{k=1}^3 U_{ek}^2 m_k \quad (3.4)$$

As a comparison, the half life for two neutrino double beta decay is given in Equation 3.5. As seen here, the half life is not suppressed by the neutrino mass, and thus the rate of this decay is much higher.

$$(T^{2\nu\beta\beta})^{-1} = G_{2\nu} |M^{2\nu\beta\beta}|^2 \quad (3.5)$$

Table 3.1 shows all isotopes with a Q-value greater than 2 MeV that undergo double beta decay, along with their Q-value and natural abundance. The Q-value for  $^{136}\text{Xe}$  was taken from [75], while all Q-values were taken from [76]. Isotopic abundances were taken from [77].

**SNO+ and neutrinoless double beta decay**

SNO+ will add  $^{130}\text{Te}$  to the liquid scintillator in the detector in an attempt to observe neutrinoless double beta decay process. Regular double beta decay has been observed for  $^{130}\text{Te}$  by the NEMO3 [78] and CUORICINO [79] experiments.  $^{130}\text{Te}$  was chosen by SNO+ because of its relatively high natural abundance. In addition, when  $^{130}\text{Te}$  is loaded into the scintillator it remains optically clear, which implies that there is a possibility of loading a high concentration amount of  $^{130}\text{Te}$  into the liquid scintillator without losing a large number of photons to optical absorption. It is anticipated that  $\sim 0.3\%$   $^{130}\text{Te}$  will initially be loaded into the liquid scintillator, but eventually there is the possibility that the concentration of  $^{130}\text{Te}$  could be increased to loading of a few percent.

Table 3.1: Neutrinoless double beta decay candidates with their corresponding Q-value and natural abundance.

Isotope	Q-value (MeV)	Abundance (%)
$^{48}\text{Ca}$	4.2737	0.187
$^{76}\text{Ge}$	2.0391	7.73
$^{82}\text{Se}$	2.9955	8.73
$^{96}\text{Zr}$	3.3477	2.8
$^{100}\text{Mo}$	3.0350	9.82
$^{110}\text{Pd}$	2.0040	11.72
$^{116}\text{Cd}$	2.8091	7.49
$^{124}\text{Sn}$	2.2877	5.79
$^{130}\text{Te}$	2.5303	34.08
$^{136}\text{Xe}$	2.46296	8.86
$^{150}\text{Nd}$	3.3673	5.63

An event from double beta decay will be detected through the scintillation light produced by the electrons in the reaction. The photons registered by the PMTs in

the detector are used to reconstruct the electron energy. The neutrinoless double beta decay signal is a sharp peak at the end of the regular double beta decay spectrum. Figure 3.3 shows an idealized case of the reaction where the detector energy resolution is very good such that the two-neutrino double beta decay signal can be differentiated from the neutrinoless double beta decay signal. Because the neutrinos are not present in the neutrinoless double beta decay reaction, all of the energy is transferred to the electrons and thus the sharp peak appears at the Q-value of the reaction.

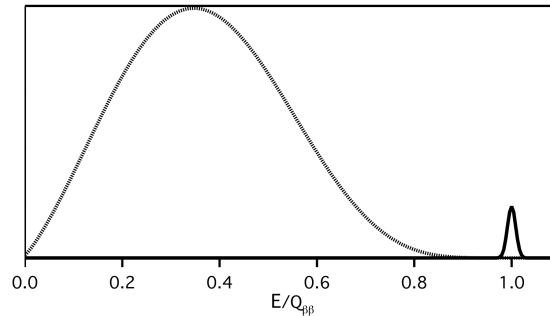


Figure 3.3: An idealized schematic of the neutrinoless double beta decay signal, where the detector energy resolution can distinguish the two-neutrino double beta decay signal (dashed line) from the neutrinoless double beta decay signal (solid line). The width of the neutrinoless double beta decay peak is also related to the detector resolution. The  $2\nu\beta\beta$  peak and the  $0\nu\beta\beta$  are not drawn to scale. Modified from [80].

In practice, the neutrinoless double beta decay signal is not so cleanly distinguished due to effects such as the imperfect energy resolution of the detector, and backgrounds which could be in the energy region of interest. Figure 3.4 shows what the signal in SNO+ could look like, using a simulation from the RAT Monte Carlo code. Major backgrounds for neutrinoless double beta decay include  $^{214}\text{Bi}$  and  $^{208}\text{Tl}$ , as well as gammas and betas from  $^{40}\text{K}$ . There is also the possibility of contamination from external backgrounds, for example from the PMTs or the AV.

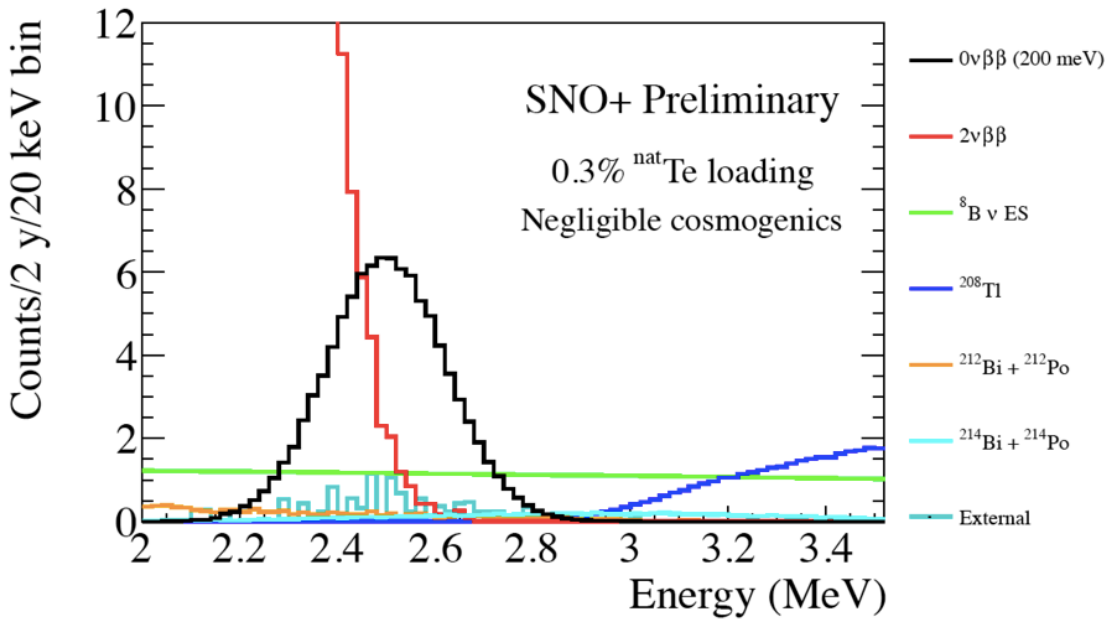


Figure 3.4: SNO+ energy spectrum with tellurium in the detector after two years of livetime. The relevant backgrounds to the signal are shown on the plot, namely the  ${}^8\text{B}$  neutrinos (the green line),  ${}^{208}\text{Tl}$  (the dark blue line),  ${}^{212}\text{Bi}$  (the orange line),  ${}^{214}\text{Bi}$  (the light blue line), external backgrounds from the hold down ropes, the AV, and the PMTs (medium blue), and the two neutrino double beta decay signal (red) [81].

### Other neutrinoless double beta decay experiments

SNO+ is not the only experiment searching for neutrinoless double beta decay. The CUORE experiment [82], will also be looking for neutrinoless double beta decay with  ${}^{130}\text{Te}$ , and is expected to begin taking data around the same time as SNO+. The advantage of SNO+ over CUORE is that the detector is larger, and so a larger mass of tellurium can be loaded into the detector. In addition, the capability for SNO+ to scale up to a larger tellurium loading makes our experiment more versatile. Other neutrinoless double beta decay experiments that are either taking data or will be taking data in the near future are looking at other candidate isotopes. The best neutrinoless double beta decay limits are currently set by experiments using  ${}^{136}\text{Xe}$ ,

namely EXO and KamLAND-Zen [83, 84]. The GERDA experiment also recently set a neutrinoless double beta decay limit using  $^{76}\text{Ge}$  [85]. Examples of future experiments are Candles [86], which will use  $^{48}\text{Ca}$  to search for neutrinoless double beta decay, and the MAJORANA experiment [87], which will use  $^{76}\text{Ge}$ . There has been a claim on the discovery of neutrinoless double beta decay in  $^{76}\text{Ge}$  by a subset of the Heidelberg-Moscow experiment [88], but this result remains controversial.

### 3.5.2 Solar neutrinos

Neutrinos are produced in the Sun through two main series of thermonuclear reactions, referred to as the pp chain and the CNO cycle. Details of these processes can be seen in Figure 3.5. Studying these neutrinos can give us information about both our Sun and the properties of the neutrinos themselves.

Figure 3.6 shows the BS05(OP) model fluxes as a function of energy for the neutrino products which come from the pp chain and CNO cycle. As discussed in Section 2.1, the overall rate of solar neutrinos has been well studied by radiochemical experiments such as Homestake, SAGE, GALLEX, and GNO. Homestake was mainly sensitive to  $^8\text{B}$  neutrinos, while the gallium experiments mainly detected pp neutrinos due to the lower energy threshold of the reaction.  $^8\text{B}$  neutrinos have been studied by Cherenkov experiments such as SNO and Super-Kamiokande. Borexino has made a measurement of the flux of  $^7\text{Be}$  neutrinos, as well as the flux of pep neutrinos.

SNO+ aims to measure pep and CNO neutrinos. As previously mentioned, pep neutrinos have been observed by the Borexino collaboration, though the uncertainty on the measured rate of these neutrinos was quite large. SNO+ aims to make a

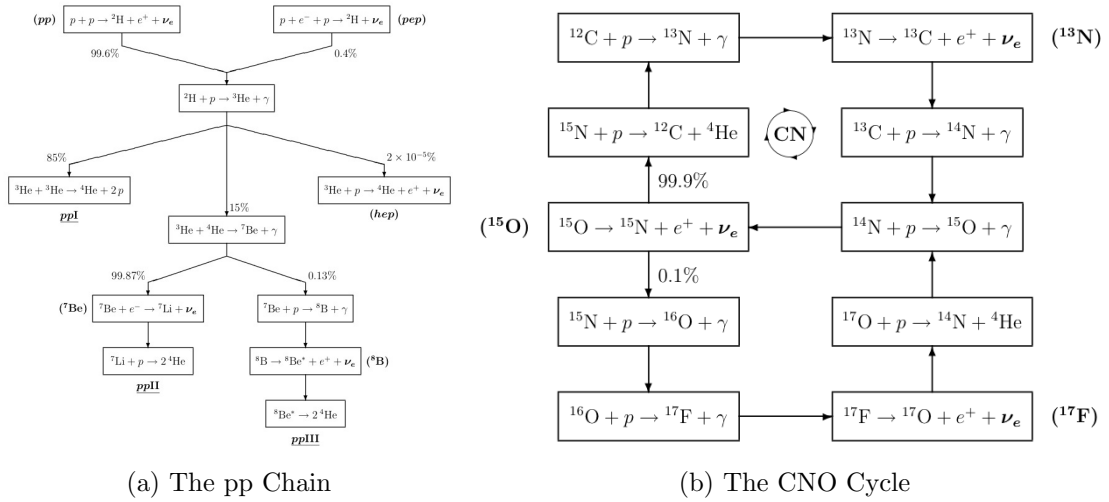


Figure 3.5: Thermonuclear reactions in the Sun that produce solar neutrinos. The names of the reactions corresponding to neutrino production are given in parentheses. Of particular interest to SNO+ is the pep neutrinos created in the pp chain and the neutrinos from the CNO cycle [47].

precision measurement of the pep neutrino rate to probe the transition region of solar neutrino oscillations, as well as to search for new neutrino physics. SNO+ plans to make a first measurement of the CNO neutrinos, which has some implications on the determination of solar elemental abundances.

### CNO Neutrinos

The CNO neutrinos are of interest because it would represent the first direct measurement of the neutrinos from this thermonuclear cycle.

While the CNO cycle is secondary to the pp chain as a mode of producing energy in our Sun, it is the primary mechanism for producing heat in more massive stars ( $>1.5$  solar masses) [54]. Measuring the flux of CNO solar neutrinos could aid in the understanding of the fuel cycle in massive stars.

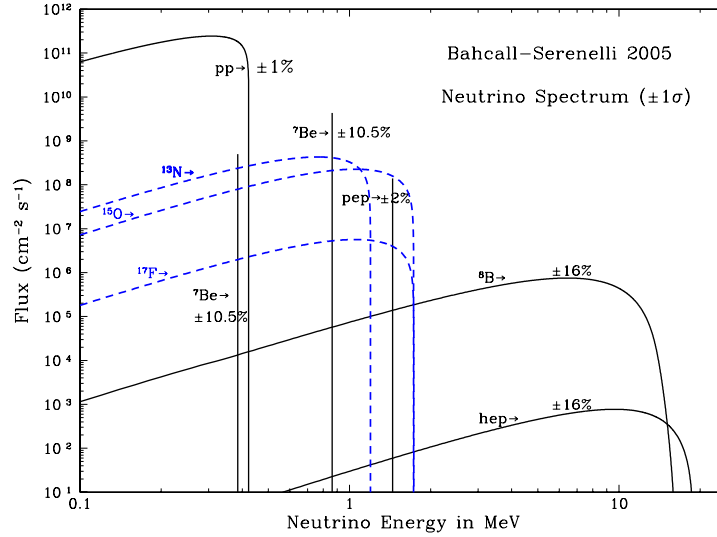


Figure 3.6: Energy spectra of solar neutrino fluxes as predicted by the Standard Solar Model. [57]

CNO neutrinos are also interesting because their flux is related to solar metallicity. The composition of our Sun can be determined by measuring the abundance of heavy metals on the surface of the Sun and inferring the overall solar metallicity. Solar models which use these metallicities do not predict observables which agree with helioseismology. Solar models which use higher metallicities are needed to agree with helioseismology results, and this gives rise to two separate solar models. The high metallicity model (BPS08(GS)) agrees with the measurements from the helioseismology surveys, and the low metallicity model (BPS08(AGS)) agrees with elemental abundance measurements [89]. The expected flux of CNO neutrinos varies by  $\sim 30 - 40\%$  between these two models. Thus, a measurement of CNO neutrinos could play a role in solving this puzzle.

### pep Neutrinos

A precise measurement of the pep neutrino survival probability would be of great interest to the physics community. As seen in Figure 3.6, the expected flux of pep neutrinos predicted by solar models has a very low uncertainty ( $\sim 2\%$ ). Because the flux coming from the Sun is well predicted in theory, a precision measurement of the flux determined at Earth would result in a survival probability measurement with a small uncertainty. This makes pep neutrinos an ideal probe for nonstandard neutrino physics. The neutrino mixing angles and mass eigenstates have well understood values from previous neutrino experiments (as described in Chapter 2). If the detected rate of pep neutrinos was significantly different from the expected three-neutrino, MSW solution, then this could suggest that there is some nonstandard physics affecting the oscillation behaviour. One type of nonstandard physics that could affect the oscillation behaviour of the pep neutrino is the influence of sterile neutrinos. Using pep neutrinos as a probe for sterile neutrino models is further examined in Chapter 5.

The energy of the pep neutrino also makes them particularly interesting. As explained in Chapter 2, there exists a transition between the vacuum oscillation dominated energy region and the matter oscillation dominated energy region for solar neutrinos. pep neutrinos are emitted with an energy of 1.44 MeV, which falls in this transition region. Since neutrinos in the transition region have a minimized contribution from the vacuum and matter terms in the Hamiltonian, higher order terms which may not be otherwise significant at other energies might have an effect on neutrinos in the transition region. Thus a precise pep neutrino flux measurement plays a key role in the search for nonstandard neutrino-matter couplings, as in [90].

Figure 3.7 shows a RAT simulation which depicts how the signals and backgrounds are expected to look in the SNO+ detector. Neutrinos will be detected through elastic scattering reactions between the incoming neutrinos and the electrons in the liquid scintillator. The main backgrounds in the solar phase will be from the uranium and thorium chains, as well as  $^{40}\text{K}$  decays.

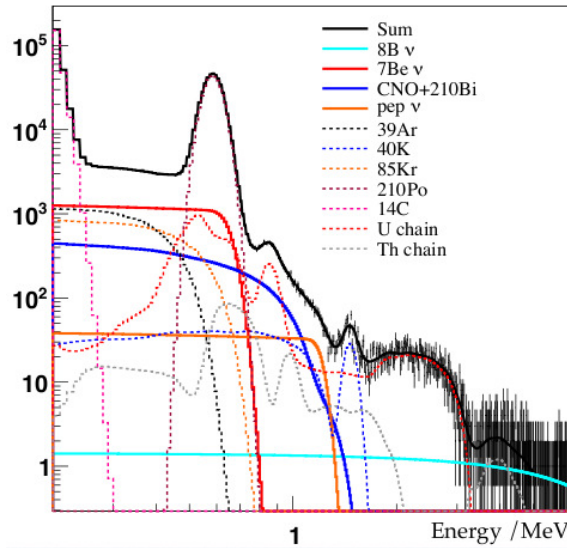


Figure 3.7: Solar neutrino signal in the SNO+ detector with backgrounds. The pep and CNO neutrinos are in the same energy region as  $^{40}\text{K}$  and the daughters from the uranium and thorium chains. [91]

The detection of low energy neutrinos is very difficult because many natural backgrounds are in this energy region. Depth is important for SNO+ since the rock overburden provides shielding from cosmogenic backgrounds that fall within the energy region of interest. A key cosmogenic background that would hinder the measurement of the pep neutrinos is the production of  $^{11}\text{C}$ , which is caused by muon spallation. The fact that SNO+ is located deeper than the Borexino experiment means that there should be less  $^{11}\text{C}$  in our detector, which will allow us to make a more precise measurement of the pep neutrino, as well as a first measurement of the CNO neutrino.

### 3.6 A final word on backgrounds (for now)

It should be clear after reading the physics goals for SNO+ that backgrounds play an important role in limiting our detection capability for the signals of interest. It seems useful to summarize the role these backgrounds play to give further motivation to the studies contained in this thesis, particularly Chapter 4.

Backgrounds are typically grouped into two categories: internal backgrounds and external backgrounds. Internal backgrounds originate from inside the fiducial volume of our signal region. External backgrounds originate outside of the fiducial volume, but can enter into or misreconstruct inside the signal region. Examples of internal backgrounds are radioactivity in the scintillator or anything which is loaded into the scintillator, such as the PPO or tellurium. Examples of external backgrounds are backgrounds from the AV walls or the PMTs.

The two major radioactive decay chains that affect the measurements in SNO+ are the  $^{238}\text{U}$  chain and the  $^{232}\text{Th}$  chain. The details of the decay chains are shown in Appendix A in Figures A.2 and A.1 respectively.

Backgrounds are a key part of signal extraction and without any characterization of the overall backgrounds, it can be very difficult to achieve the physics goals outlined above. It would be very useful to have some tool to eliminate backgrounds in our detector, especially between alpha backgrounds and beta signals. Chapter 4 investigates a method for tagging alpha backgrounds.

# Chapter 4

## Timing Measurements in Linear Alkylbenzene

### 4.1 Motivation

Proper reconstruction of events in the SNO+ detector requires many measurements which characterize the scintillator optics. One such measurement is of the scintillator emission timing profile, which is the intensity of emitted light as a function of time during a single event in the detector. Doing a bench-top scale experiment to measure the emission timing profile of the SNO+ scintillator cocktail allows for the estimation of the timing profile that is expected to be seen in the detector. It also has the advantage of being able to easily test the timing of the scintillator in different conditions, for example in an oxygenated or deoxygenated state.

The measurement of the timing components is useful because there exists differences in the timing profiles due to alpha excitation compared with beta excitation, which can lead to a powerful method of discrimination between signals from different

particle types. We are particularly interested in discriminating the signals from neutrinoless double beta decay and low energy solar neutrinos, which are beta events, from alpha backgrounds. This is known as pulse shape discrimination (PSD) and this had not previously been measured for our scintillator cocktail.

The measured timing components outlined in this chapter have been implemented into the RAT Monte Carlo code which is used by SNO+ as a means to simulate events in the detector. Knowing these timing components before the start of data taking will help us to do studies that involve our timing response. Section 4.8 shows how the detector effects can distort the timing parameters which were measured in the bench-top experiment, and also shows how PSD can be used to tag  $^{210}\text{Po}$  in the detector.

This chapter begins with a description of the components of the scintillator cocktail. Next, the scintillator physics related to the timing profile is outlined. The experimental apparatus and method used to collect the data for the timing profile is described, then the results of the timing parameters are given. Next, the timing profiles for beta and alpha excitation are compared and the possibility of using the timing profiles as a way to discriminate between these two event types using PSD is examined. Finally, the timing components are implemented into the RAT Monte Carlo code to see how detector effects can change the PSD capability of the scintillator cocktail. An example of using PSD to tag  $^{210}\text{Po}$  backgrounds is given.

## 4.2 The SNO+ Scintillator Cocktail

Linear alkylbenzene (LAB) was chosen as the solvent for the SNO+ scintillator cocktail due to its low toxicity, high flashpoint, and the relative ease of purchase, as well

as its excellent optical properties. LAB is a precursor chemical used in detergent manufacturing, making it a cost effective choice.

Organic scintillators, including LAB, are known for having a fast decay time [92]. This helps to reduce the chance of overlapping events, but can have a poorer light yield in comparison to other scintillator types. It also can be the case that the optical absorption and emission spectra for a scintillator can overlap, making it unsuitable for detecting the emitted light over long propagation distances. In the case of LAB, both of these challenges apply. In addition, the wavelength of the light emitted by LAB excitation is not in the region where the PMTs have a high detection efficiency. To circumvent these issues, the SNO+ scintillator cocktail includes a fluor, namely PPO (2,5-diphenyloxazole), which will shift the wavelength of the emitted light out of the absorption region and into the region where the PMTs have a high detection efficiency. As a particle enters the scintillator volume, the LAB is excited and transfers its energy non-radiatively to the PPO molecules very efficiently. The light produced by the scintillation of the PPO molecules are viewed by the PMTs and information about the event is extracted. The amount of PPO in the scintillator cocktail will be  $\sim 2\text{g/L}$  of LAB.

### 4.3 Scintillator Physics

A comprehensive description of the physics principles of organic scintillators can be found in [93].

The light produced in the detector is a result of the fluorescence of the PPO molecule. When the PPO molecule is excited, electrons populate the available singlet and triplet states. The de-excitation from singlet to ground state is spin allowed

and happens very promptly (on the order of a few nanoseconds). The de-excitation from the triplet state to the ground state is spin-forbidden. Since the electron cannot transition directly from the triplet state to the ground state, fluorescence is produced only when some mechanism allows the electron in the triplet state to transition to the singlet state. This is broadly known as intersystem crossing. Examples of such mechanisms are thermal excitations of the triplet state which makes it isoenergetic with a singlet state orbital, or collisions between excited PPO molecules. Once the electron has transitioned to the singlet state, it decays to the ground state and has the same characteristic wavelength as the prompt light. Since this intersystem crossing mechanism takes some time to occur, this mode of fluorescence gives light which is delayed when compared with the prompt light provided by direct singlet to ground state de-excitation. There are therefore at least two lifetimes associated with the fluorescence: a short lifetime from direct singlet to ground state fluorescence and a longer time associated with electrons which are excited to the triplet state, undergo intersystem crossing to a singlet state, and de-excite to ground state. In reality, a scintillator fluorescence timing spectrum can be best fit with multiple characteristic lifetimes due to the variety of intersystem crossing mechanisms which contribute to the longer time component.

As discussed in [93], the form of the fast and slow components of the light emission do not depend on the ionization density. The relative intensities of the timing components, however, do depend on ionization density, and therefore depend on the ionizing particle. Alpha particles have a high ionization density, which results in a saturation of the available singlet states. Thus in organic scintillators, an alpha particle will produce a higher relative intensity of the slow decay component when compared to

an electron. This is the basis of using timing profiles as a method to discriminate between electron and alpha events in the detector, which is known as PSD.

Oxygen dissolved in the scintillator also plays an important role in determining the relative intensity of fast and slow decay emission. Oxygen provides a non-radiative mode of de-excitation for the triplet state, resulting in a reduced amount of slow decay component emission. Scintillators are often deoxygenated to reduce this effect and to improve their pulse shape discrimination capability. In the SNO+ experiment, the scintillator in the detector will be in a deoxygenated state.

## 4.4 Experimental Apparatus and Method

To sample the light emission timing profile the single photon sampling technique was implemented as described in [94]. In this method, the light produced in a sample of scintillator is observed by two photomultiplier tubes (PMTs) connected to fast timing discriminators. The first PMT observes many photons and is therefore highly likely to detect a photon at the beginning of an event. This provides a trigger for the electronics chain. The second PMT is covered by a mask containing a small hole in the centre, which allows for a very small probability of more than one photon being detected. The unmasked PMT provides a reference (start) time for each event. A finite time later, a photon is detected by the masked PMT, which statistically samples photons over the decay time of the light pulse. The time difference between the start and stop of each event is recorded. By producing a histogram of these delayed coincidence events, accounting for the background and timing resolution, the timing profile of the scintillator can be obtained. Figure 4.1 shows a schematic of the experimental setup. A glass dish containing about 50 mL of LAB + 2g/L PPO

was optically coupled to a 5 cm diameter PMT (Electron Tubes Ltd 9266KB). This is labeled PMT B in Figure 4.1. PMT B was unmasked such that it was able to see all of the scintillation light produced, as previously described. The scintillator dish was also viewed from above by a masked 5 cm diameter PMT (also Electron Tubes Ltd 9266KB), labeled PMT A in Figure 4.1.

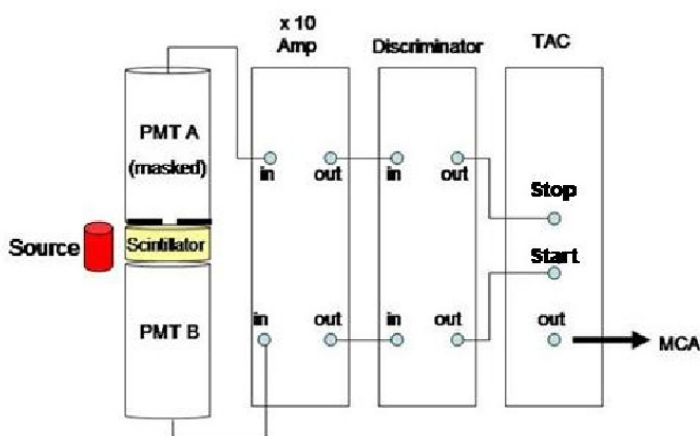


Figure 4.1: Electronics setup for scintillator timing profiles.

The signal from each PMT was connected to an independent channel of a fast timing discriminator (Phillips 715). The discriminator threshold for each PMT was set by using the discriminator signal to gate an MCA energy spectrum. For PMT A (masked), the discriminator threshold was set such that the energy spectrum cut off just below the single photoelectron peak for all runs. For PMT B (unmasked), the discriminator threshold was set such that a suitable energy threshold was selected to exclude events lower in energy than our source. The threshold for PMT B remained the same for alpha and electron runs, which ensured the zero offset of the timing

spectrum was identical for all runs. The output from the PMT B discriminator was connected to the start input of a time to amplitude converter (TAC) (ORTEC 566). The PMT A discriminator channel was connected to the stop input of the TAC. A range of 500 nanoseconds was used for the TAC time window. The output of the TAC was connected to a PC running the Maestro multichannel analyzer (MCA) data acquisition software. Maestro binned the time difference for each event in terms of MCA channels.

Cesium-137 was used to obtain a sample of electrons via Compton scattering of the 662 keV gamma. The discriminator threshold was set to accept the full Compton edge. An americium-241 source was used to produce a sample of alpha events. This source was immersed in the scintillator and the discriminator threshold was set to exclude the 59 keV gamma, but include the full 5.48 and 5.44 MeV (quenched) alpha peaks.

Coincidences between the PMTs could be caused by non-scintillation events. To characterize this, complementary background runs were taken before and after each timing run. In a background run, the radioactive source remained in place and the hole in the mask covering PMT A was covered to prevent detection of photons from scintillation. The background spectrum was dominated by fast coincidences from cosmic ray interactions in the PMT glass and random coincidences between dark noise events. Each background run was time normalized and subtracted from its corresponding timing run.

The timing resolution was measured by removing the mask from PMT A, which allowed scintillation light to be recorded by both PMTs simultaneously. This produced a Gaussian distribution of timings, with sigma equal to the timing resolution

of the apparatus. Delays ranging from 5 nanoseconds to 100 nanoseconds were introduced between the discriminator and the stop channel of the TAC. This additional delay shifted the mean of the Gaussian by a given number of MCA channels and the timing calibration was obtained by applying a linear fit to this data. A timing resolution of  $1.9 \pm 0.2$  ns was obtained by fitting a Gaussian distribution to this data along with a conversion factor of  $16.98 \pm 0.85$  MCA bins per nanosecond.

Oxygen is commonly thought to quench the slow decay component of scintillators, although the extent of this effect was not widely shown in the literature. Timing profiles were obtained for both oxygenated and deoxygenated scintillator to study this quenching effect directly. In the oxygenated configuration, timing profiles were taken with the scintillator exposed to the lab air. In the deoxygenated configuration, an in-house method was used to remove the oxygen from the setup. A schematic of the deoxygenated set up can be seen in Figure 4.2. Plastic sheeting was placed under the PMT-scintillator set up and a needle at the end of a hose attached to a high purity nitrogen cylinder was placed in the scintillator dish. An acrylic cylinder that was approximately 30 centimeters in diameter and roughly 1 meter in height was lowered over the PMT-scintillator apparatus. A small (3 centimeter) hole was cut into the bottom of the acrylic cylinder, to allow for the circulation of nitrogen, as well as to allow for the wires of the electronics to pass through. The plastic sheeting was then taped around the bottom of the acrylic cylinder to ensure a mostly airtight environment. A copper pipe was plumbed into the top of the acrylic cylinder. The pipe was then connected via a valve to the hose that was connected to the nitrogen bottle. The nitrogen cylinder was opened in order to flood the inside of the cylinder with nitrogen. Oxygen was displaced from the cylinder by flowing through the opening at

the bottom of the cylinder. Simultaneously, nitrogen was bubbled through the scintillator cocktail for 20 minutes. After 20 minutes, the valve connected to the needle was shut off and the pressure of the nitrogen was turned down to just maintain the overpressure of  $N_2$  gas inside the cylinder. The timing measurement was then taken in this nitrogen-rich environment, with care being taken to ensure that the nitrogen overpressure was maintained throughout the measurement. As a cross-check to ensure that the scintillator was deoxygenated throughout the measurement, an energy spectrum was taken three times per timing measurement: before the deoxygenation process, just after the nitrogen was bubbled through the scintillator, and at the end of the timing measurement. When the scintillator was in the oxygenated state, the energy spectrum was measured. After the nitrogen was bubbled through the scintillator, the energy of the signal from the radioactive source was about 17 % higher than in the oxygenated state. The energy spectrum was measured at the end of each run to confirm that it matched the spectrum just after deoxygenation.

## 4.5 Extraction of Timing Parameters from Timing Profiles

Peak normalized timing profiles with beta and alpha excitation using scintillator in both the oxygenated and deoxygenated configuration are shown in Figure 4.3. Qualitatively we can see that, as expected from the theory described in Section 4.3, timing profiles for alpha excitation have a larger slow decay component when compared with beta excitations because the ionization density is higher. This allows for the possibility of discriminating between event types in our detector, which will be described

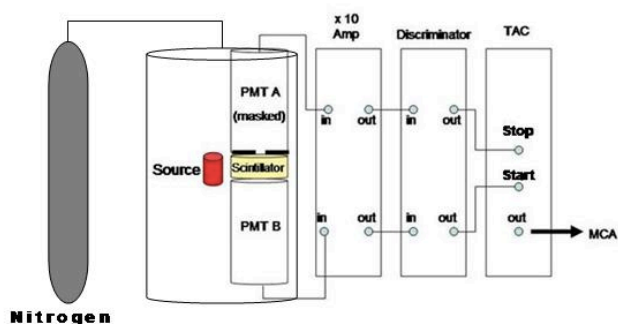


Figure 4.2: Electronics setup for scintillator timing profiles taken in the deoxygenated configuration.

more fully in Section 4.7.

In order to extract timing components from the profiles, a function consisting of three exponentials convolved with a Gaussian was fitted to the data. This is shown explicitly in equation 4.1. Here,  $A_i$  is the weighting of the exponential in the fit,  $t_i$  is the characteristic decay time, and  $\sigma$  should match the timing resolution, which accounts for the PMT transit time jitter as well as any discriminator timing jitter that could affect the timing resolution. The relative weighting of each exponential component,  $R_i$ , can be obtained using equation 4.2. The relative weights of the exponentials, the characteristic decay time, and the timing resolution were all allowed to float in the fit. The TF1 function fitting class, found in the ROOT analysis framework was used to perform the fit to the data. A cross check was made using

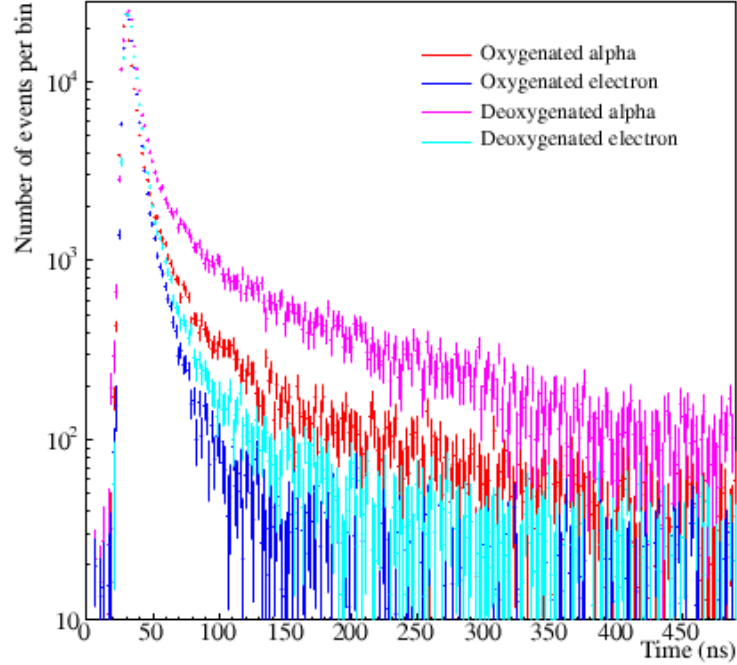


Figure 4.3: Background subtracted, peak normalized timing profiles due to alpha and beta excitation for oxygenated and deoxygenated scintillator. Clear differences can be seen in the slow decay tail of the profile when comparing both particle type and oxygenation level. Alpha particles produce profiles with a larger slow decay component compared with profiles from beta particles. Also, deoxygenated scintillator has a larger slow decay component compared with oxygenated scintillator. [95]

ROOFIT that is also found in ROOT. The TF1 fit results are shown in Table 4.1.

$$F(t_i) = \sum_{i=1}^3 A_i \exp\left(\frac{-x}{t_i} + \frac{0.25}{\sigma t_i^2}\right) \sqrt{\frac{\pi}{4\sigma}} \left[1 + \text{Erf}\left(\sqrt{\sigma}\left(x - \frac{0.5}{t_i\sigma}\right)\right)\right] \quad (4.1)$$

$$R_i = \frac{A_i t_i}{\sum_{i=1}^3 A_i t_i} \quad (4.2)$$

Table 4.1: Summary of timing results from alpha and beta timing profiles. [95]

	Oxygenated $\alpha$	Oxygenated $\beta$	Deoxygenated $\alpha$	Deoxygenated $\beta$
$t_1$	$4.4 \pm 0.2$	$4.3 \pm 0.3$	$3.2 \pm 0.2$	$4.6 \pm 0.3$
$t_2$	$20 \pm 1$	$16 \pm 1$	$18 \pm 1$	$18 \pm 1$
$t_3$	$178 \pm 10$	$166 \pm 11$	$190 \pm 10$	$156 \pm 9$
$A_1$	$520 \pm 6$	$768 \pm 12$	$794 \pm 7$	$753 \pm 14$
$A_2$	$59 \pm 3$	$59 \pm 4$	$53 \pm 3$	$61 \pm 3$
$A_3$	$3.3 \pm 0.1$	$0.8 \pm 0.1$	$12.6 \pm 0.2$	$2.2 \pm 0.1$
$R_1$ (%)	55	75	44	71
$R_2$ (%)	28	22	16	22
$R_3$ (%)	17	3	41	7

## 4.6 Comparison of Timing Parameters Found in Literature

Since the measurement of these timing parameters was made, other researchers have also measured the timing parameters of PPO in LAB and this has served as a good cross check for our results. The most extensive of these comparisons can be found in [96] where there is a table of timing parameters and relative intensities for a deoxygenated cocktail of 2 g/L PPO in LAB. A tabulated comparison of our results with the results of beta timing from [97] and the results from both beta and alpha timing from [96] can be seen in Table 4.2. As explained in [96], the authors chose to use four timing components because they were fitting over a larger time range than we were using in our work. If the time range was restricted, three timing components could be used to describe the data. Looking at Table 4.2, we can see that both sets of data show the same trend of the long timing component contributing more to the alpha excitation than the beta excitation. The timing of LAB+PPO has also been

measured in [98], though not for 2g/L of PPO and not using a comparable fitting function. Thus, the results from [98] are not included in Table 4.2. Though not all the values agree within error in Table 4.2, there are many that are within two or three sigma and the overall picture is very similar. Strong correlations exist between the extracted parameters and there are many parameters being fit. Therefore, it can appear that the results of [96] and [97] do not agree with our work when one examines individual parameters without accounting for the correlations. The values and timing profiles are in good agreement, also concluded by the authors of [96].

Table 4.2: Summary of comparison between our work and that of [96] for timing results from alpha and beta timing profiles.

	our work		[96]		[97]
	$\alpha$	$\beta$	$\alpha$	$\beta$	$\beta$
$t_1$	$3.2 \pm 0.2$	$4.6 \pm 0.3$	$4.69 \pm 0.034$	$5.13 \pm 0.05$	$5.21^{+0.04+0.003}_{-0.05-0.03}$
$t_2$	$18 \pm 1$	$18 \pm 1$	$18.61 \pm 0.27$	$17.61 \pm 0.36$	$18.4^{+0.6+0.2}_{-0.6-0.2}$
$t_3$	$190 \pm 10$	$156 \pm 9$	$92.29 \pm 1.42$	$87.40 \pm 2.18$	$118^{+3+0}_{-5-2}$
$t_4$	–	–	$551.15 \pm 6.20$	$554.02 \pm 15.49$	–
$R_1$ (%)	44	71	$48.2 \pm 0.4$	$60.9 \pm 0.6$	77
$R_2$ (%)	16	22	$29 \pm 0.3$	$27.4 \pm 0.5$	17
$R_3$ (%)	41	7	$14.4 \pm 0.2$	$7.5 \pm 0.2$	–
$R_4$ (%)	–	–	$8.2 \pm 0.2$	$4.2 \pm 0.2$	–

## 4.7 Pulse Shape Discrimination with the Bench-Top Results

As seen in Figure 4.3, there is a clear difference between the timing profiles due to alpha and beta excitation. This could provide us with a powerful tool to differentiate

between events due to different particle types within the detector. Other neutrino experiments, such as Borexino [99], have successfully implemented PSD into their analysis, though with a different scintillator.

In order to differentiate between particles on an event-by-event basis using pulse shape discrimination (PSD), a discrimination parameter must be chosen. Because the slow decay component has a greater relative contribution in the alpha profile, we will define our parameter to be the peak-to-total ratio. The peak-to-total ratio is calculated by defining a peak region of the timing profile and comparing the number of counts in the peak with the total number of counts in the profile. To simulate how effective this might be, the peak-to-total ratio was calculated using 300 points sampled from the timing distribution, which would correspond to the number of photons produced by a 5 MeV alpha or a 0.5 MeV beta. Looping over this calculation many times gave a Gaussian spread, as seen in Figure 4.4.

By making a cut in the peak-to-total parameter, the tagging capability using this method can be quantitatively measured. Using this technique, it was determined that oxygenated LAB+PPO has a discrimination capability of tagging 99 % of alphas while keeping > 99% of betas. In the deoxygenated LAB+PPO, the discrimination power increases with > 99.9% of alpha tagged with > 99.9% of betas retained. This level of discrimination represents a best case scenario since other optical effects in the SNO+ detector, such as reflections, are expected to make PSD worse in the actual experiment.

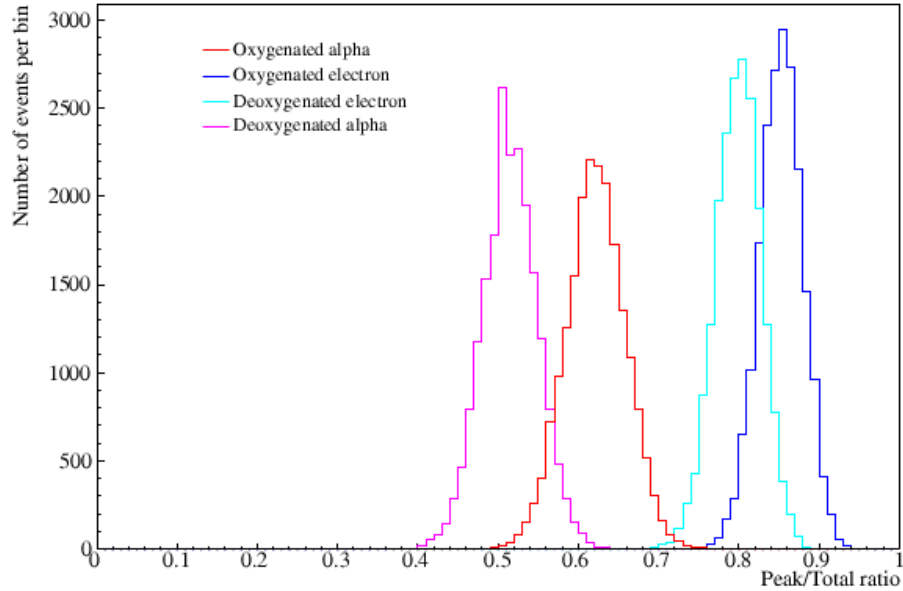


Figure 4.4: Peak-to-total ratios for excitations due to alpha and beta particles in oxygenated and deoxygenated LAB+PPO. [95]

## 4.8 Application of Pulse Shape Discrimination in the SNO+ Experiment

In order to explore the pulse shape discrimination capability in the SNO+ detector, a study was performed using the RAT Monte Carlo code. In particular, tagging the alpha decay of  $^{210}\text{Po}$  was used as an example for how PSD would be implemented in the experiment.

### 4.8.1 Motivation for Tagging $^{210}\text{Po}$ Events

The tagging of  $^{210}\text{Po}$  is particularly valuable to the SNO+ experiment because it is the decay daughter of  $^{210}\text{Bi}$ , which is a major background for the CNO neutrino measurement. As seen in Figure A.2,  $^{210}\text{Bi}$  is produced in the uranium chain as

the daughter of  $^{210}\text{Pb}$ .  $^{210}\text{Bi}$  decays to  $^{210}\text{Po}$  via the emission of a beta particle with an end-point energy of 1.16 MeV and a half life of 5.01 days. The resulting energy spectrum of the  $^{210}\text{Bi}$  beta resembles the electron recoil signal for the CNO neutrino, as seen in Figure 4.5. Because the CNO and  $^{210}\text{Bi}$  spectra cannot be easily differentiated in energy, nor can the signals be disentangled using PSD methods, the  $^{210}\text{Po}$  daughter of  $^{210}\text{Bi}$  is used as a marker for the levels of  $^{210}\text{Bi}$  in the detector. As seen in Figure A.2,  $^{210}\text{Po}$  decays with the half life of 138 days via emission of a 5.30 MeV alpha particle.

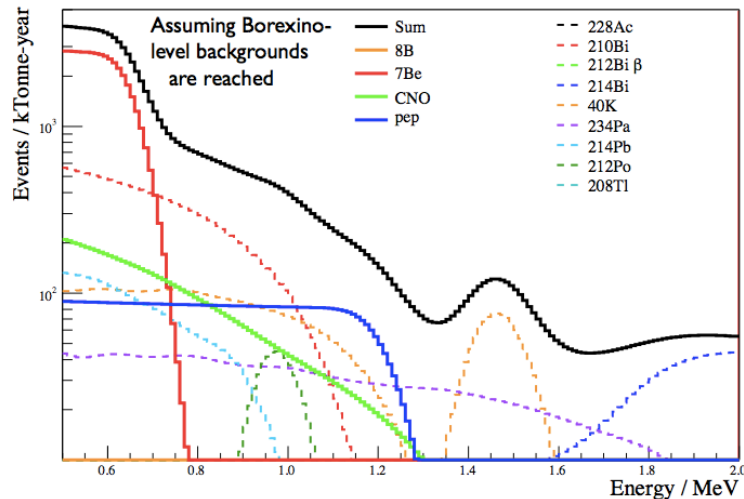


Figure 4.5: Solar neutrino signals with key backgrounds. The energy spectrum from CNO neutrinos is shown as the green solid line, while the  $^{210}\text{Bi}$  background is shown with the dotted red line.

If the  $^{210}\text{Bi}$  and  $^{210}\text{Po}$  were in equilibrium, the measurement of the polonium daughter would give a direct measurement of the contamination level of the bismuth parent. In reality, other liquid scintillator based solar neutrino experiments have found that the  $^{210}\text{Bi}$  and  $^{210}\text{Po}$  rates have not been in equilibrium [100], for reasons that have yet to be fully determined. It is still possible to determine the levels of

$^{210}\text{Bi}$  using a time-analysis method, the details of which are described in [100].

### 4.8.2 Simulated Timing Profiles in the SNO+ Detector

The timing results from the bench-top measurement were included in the RAT model and the timing profiles were reconstructed from the code output, which now considered the full detector effects. The profiles were generated using 10,000 events, which were uniformly distributed in the scintillator volume. The energy for the alpha particle was chosen to be 5.3 MeV to correspond with the alpha decay of  $^{210}\text{Po}$ . The quenching of alpha particles in the scintillator is approximately an order of magnitude in energy, and so the electrons were generated with an energy of 0.53 MeV to correspond to roughly the same number of hit PMTs for an average event. It should be noted that in the SNO+ experiment, the scintillator will be deoxygenated and so the timing profiles simulated here will correspond to the deoxygenated bench-top case. Figure 4.6 shows the summed timing residual of the simulated alpha and electron events, where the timing residual  $t_r$  is defined in equation 4.3 using the time recorded by the PMT in the detector ( $t_{PMT}$ ), the time of flight of the photon ( $TOF$ ), and the event time which was reconstructed with the scintFitter tool in RAT ( $t_{fit}$ ). The distributions in Figure 4.3 have been peak normalized.

$$t_r = t_{PMT} - TOF - t_{fit} \quad (4.3)$$

In Figure 4.6, we can see the sum of the timing pulses. Events before the peak are due to dark noise in the detector and will not be considered in the analysis. As seen in Figure 4.6, the alpha tail at long times is very distinguishable from the electron tail, even when detector effects are considered.

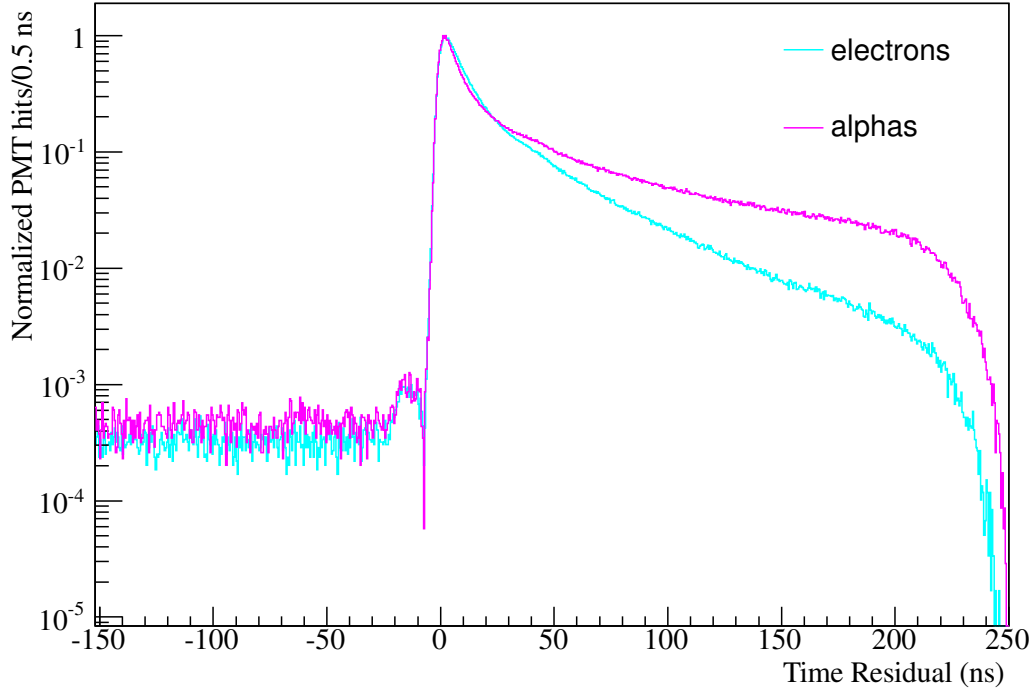


Figure 4.6: Peak normalized timing spectrum from alpha and electron excitation in the SNO+ detector using the RAT Monte Carlo code.

### 4.8.3 Pulse Shape Discrimination using Peak-to-Total Method

The PSD capability of the simulated detector data was determined using the peak-to-total method described in Section 4.7. The peak-to-total distributions, which were constructed using the peak normalized timing distributions in Figure 4.6, are shown in Figure 4.7. The peak of the distribution was defined to be in the range of 0 ns – 24 ns and the total was defined to be in the range of 0 ns – 250 ns.

Qualitatively, we can already see that there is more overlap between the alpha and electron distributions in Figure 4.7. Using the same benchmark as was used for the bench-top results in Section 4.7, we can tag 80% of the alpha events while

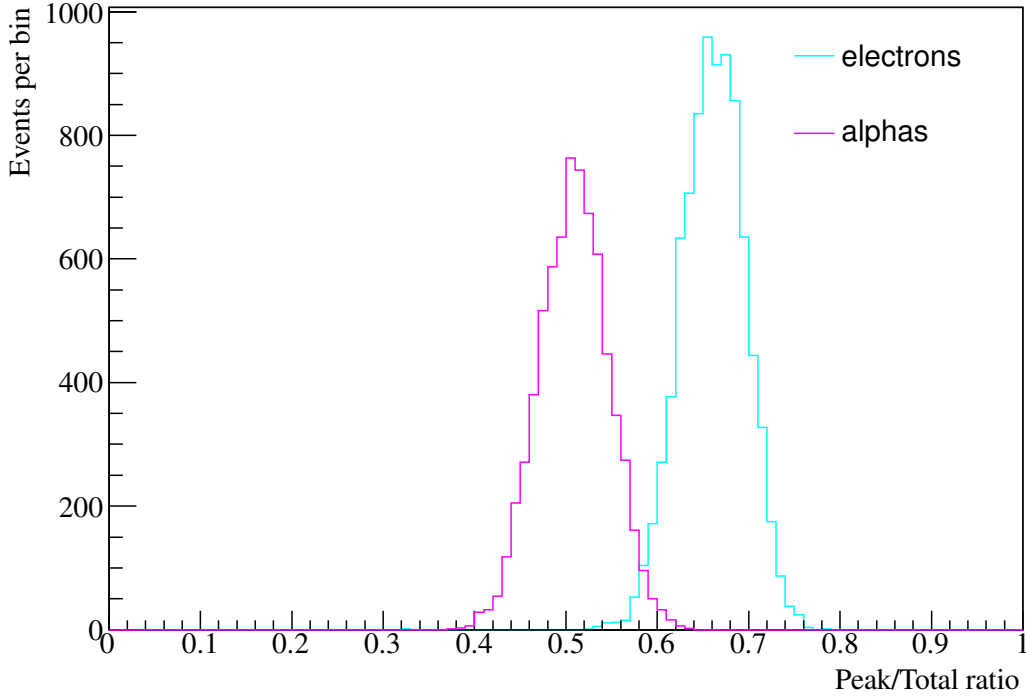


Figure 4.7: Peak-to-total ratios using the timing profiles in figure 4.6

maintaining 99.9% of the electron signal (i.e. 0.1 % of the electron signal will be background events in the alpha tag).

The diminished capability of distinguishing events from alpha and electron excitation using the peak-to-total method provides motivation for using a more optimal method for discriminating the timing distributions. A good candidate is Gatti's method, which will be described in Section 4.8.4.

#### 4.8.4 Pulse Shape Discrimination using Gatti's Method

Gatti's method, which is outlined in [101], is designed to maximize the weight of the bins where there is the largest difference between the two distributions being

compared.

To construct the Gatti number, which is the discrimination parameter used in this method, we first consider the area-averaged time functions for alpha and electron timing distributions. In order to construct the average electron and alpha functions, the time residuals calculated using equation 4.3 were summed for all the simulated events for a given particle type. The weighting factor,  $P_i$ , can then be calculated as in equation 4.4 where  $\bar{\alpha}_i$  is the  $i^{\text{th}}$  bin content of the average alpha function and  $\bar{\beta}_i$  is the  $i^{\text{th}}$  bin content of the average electron function.

$$P_i = \frac{\bar{\alpha}_i - \bar{\beta}_i}{\bar{\alpha}_i + \bar{\beta}_i} \quad (4.4)$$

The Gatti number,  $G$ , can then be calculated using equation 4.5 where  $S_i$  is the bin content of bin  $i$  in the signal distribution.

$$G = \sum_i P_i S_i \quad (4.5)$$

The distribution of Gatti numbers for the simulated runs is shown in Figure 4.8. Only the bins between time 0 ns and 250 ns were considered. We can see from Figure 4.8 that there is less overlap between alpha and electron Gatti number distributions. Again, using the case where we keep 99.9 % of the electron signal, we can now tag 99.9 % of the alpha events.

Figure 4.9 shows the comparison between the discrimination capability of the peak-to-total and Gatti methods. In the case of tagging  $^{210}\text{Po}$  decays, the Gatti method is the better of the two methods.

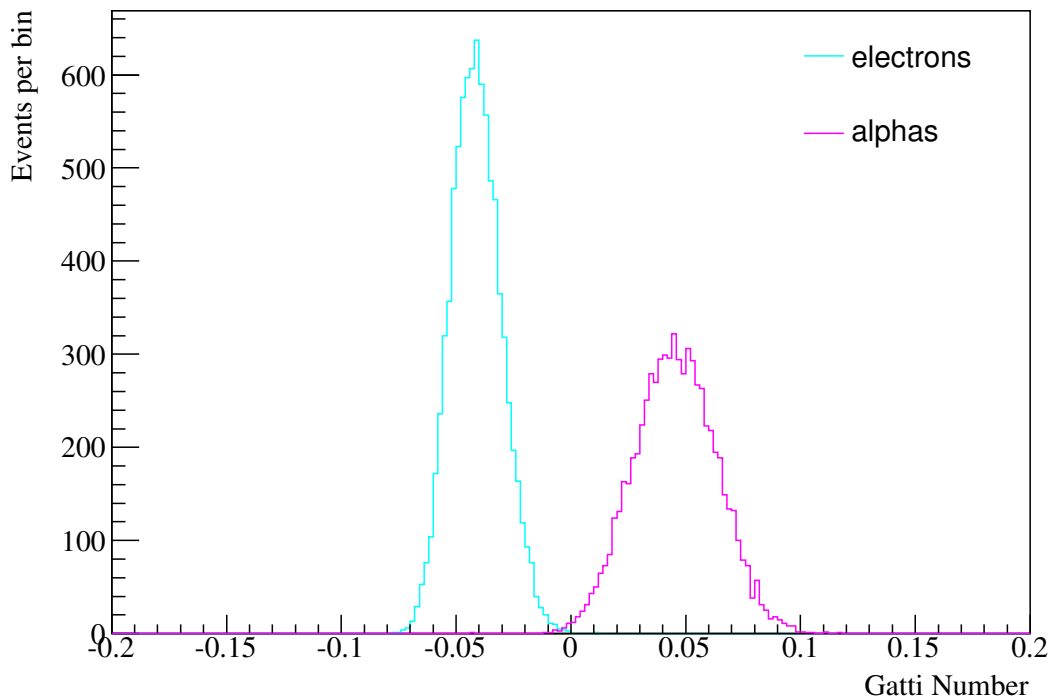


Figure 4.8: Gatti number distributions using the area-normalized timing profiles in figure 4.6.

## 4.9 Summary and Conclusions

This chapter has shown that the scintillator timing profile for linear alkylbenzene contains multiple decay components. The relative populations and values of these components are sufficiently different for electron and alpha events, such that separation and thus discrimination between particle types is possible. By directly comparing measurements of oxygenated and deoxygenated scintillator, it has been demonstrated that removal of oxygen from the scintillator leads to improved particle identification and separation of alpha and electron events. This work was the first to conclusively show this is the case for linear alkylbenzene with PPO, a scintillator which will be

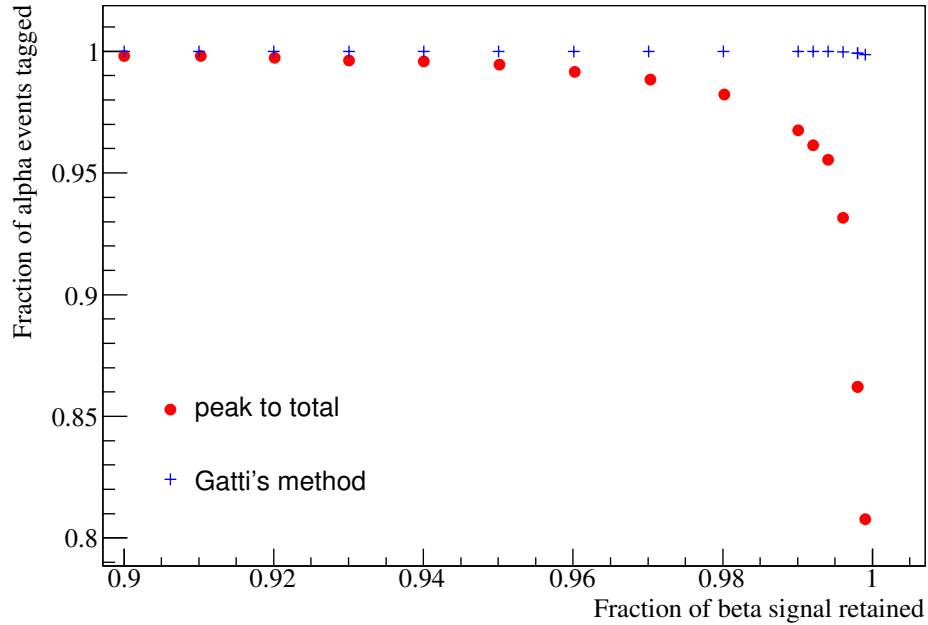


Figure 4.9: Comparison of the discrimination capability of the peak-to-total and Gatti methods.

used in several large scale neutrino physics experiments, including SNO+.

This chapter also explored the PSD capability in the SNO+ detector using events simulated with RAT. It was found that the timing distributions were sufficiently different to discriminate between alpha and electron events, even when considering detector distortions. In addition to the peak-to-total method for discriminating alpha and beta events, Gatti's method was employed and was found to give better discrimination results. Using Gatti's method, we can reach a PSD capability which is comparable to the bench top results.

# Chapter 5

## Solar Neutrinos as a Probe for a 3+1 Sterile Neutrino Model

This chapter will explore the allowed parameters of a sterile neutrino model given the constraints from current solar neutrino data, and will examine how adding a SNO+ pep neutrino measurement could further constrain these parameters. Section 5.1 introduces the sterile neutrino and the 3+1 sterile neutrino model. Section 5.2 describes the mathematics of sterile neutrino oscillations. Section 5.3 will describe how a sterile neutrino could affect the active neutrino observables, as well as the code that was developed to calculate these observables. Section 5.4 will explain the global solar neutrino oscillation analysis code that will be used to determine the excluded and allowed regions of the sterile neutrino oscillation parameter space. Finally, Sections 5.5 and 5.6 will show the results of the fits to solar data.

## 5.1 An Introduction to Sterile Neutrinos

The sterile neutrino has been mentioned previously, but this section will formally introduce the properties of the sterile neutrino.

### 5.1.1 The Definition of a Sterile Neutrino

Sterile neutrinos are similar to active neutrinos in that they are also neutral leptons, but they differ in that they are proposed to exist as a right handed chirality neutrino and a left handed chirality antineutrino, which is opposite in handedness to the active neutrino flavours. As a consequence, sterile neutrinos do not take part in weak interactions, however they could be detected indirectly if they were to mix with active neutrinos. A good review of sterile neutrino theory and experimental hints can be found in [102].

### 5.1.2 Motivation for Sterile Neutrinos in the Solar Neutrino Energy Region

The motivation for searching for sterile neutrinos in the solar neutrino energy sector comes from the absence of a detected upturn in electron neutrino survival probability at the low energy end of the  $^8\text{B}$  spectrum. As seen in Figure 2.6, solar neutrinos above 10 MeV are in the matter dominated region and have a  $P_{ee}$  value of around 0.3. As you move to lower energies and move into the transition region, you would expect to measure a higher electron neutrino survival probability. The best fit values from SNO [37] favours a downturn in  $P_{ee}$  as energy is increased and the SK results [103] measure a flatter than expected  $P_{ee}$  as energy is increased. These results individually

are significant at a level of less than one sigma, but this does leave room for proposed models which can distort the electron neutrino survival probability in the transition region. As we will see in this section, introducing a sterile neutrino with certain mass and mixing parameters can cause a distortion in  $P_{ee}$  that will better describe the  $^8\text{B}$  neutrino data.

### 5.1.3 The 3+1 Sterile Neutrino Model

The sterile neutrino model considered in this thesis will be a 3+1 model, which means that there are three active neutrinos and one sterile neutrino. This is based on a 2+1 model from de Holanda and Smirnov [104, 105]. The 2+1 model approximates the active neutrinos to be only two flavour types, which is valid if one of the active mixing angles are very small. Because we have now measured all three active mixing angles, and know they are sufficiently large, a more proper treatment involves considering all three flavour types of active neutrinos.

In the 3+1 model, we add a sterile neutrino mass eigenstate and flavour eigenstate,  $\nu_4$  and  $\nu_s$  respectively, and only allow mixing between this sterile eigenstate and the active mass eigenstate  $\nu_1$ . In this thesis, the case of  $m_1 < m_4 < m_2$  will be the only one considered. This gives the best description of the current solar data because it only weakly affects the higher energy solar neutrinos, which are better constrained by current experimental measurements than their lower energy counterparts. It is also the most interesting case for the pep energy region since it can have large effects in the transition region. Thus, we introduce two new parameters to our oscillations, an active to sterile mixing angle  $\theta_{14}$  and a mass squared splitting between the sterile and active eigenstates  $\Delta m_{41}^2$ . In order to follow with the notation in the de Holanda and

Smirnov model, we will write  $\theta_{14}$  as  $\alpha$  and we will consider the new mass eigenstate as a ratio with the solar mass splitting and create a parameter called  $R_\Delta$  where  $R_\Delta \equiv \frac{\Delta m_{41}^2}{\Delta m_{21}^2}$ .

## 5.2 Sterile Neutrino Oscillations in the Sun

### The Hamiltonian in the Flavour Basis with Sterile Neutrinos

With the addition of the two new parameters in the sterile model, the Hamiltonian must be modified. We will now consider the Hamiltonian of the form

$$i \frac{d}{dt} \begin{pmatrix} \nu_e \\ \nu_\mu \\ \nu_\tau \\ \nu_s \end{pmatrix} = (U_s m_s U_s^* + V_s) \begin{pmatrix} \nu_e \\ \nu_\mu \\ \nu_\tau \\ \nu_s \end{pmatrix} \quad (5.1)$$

which is similar to Equation 2.14 but with adjusted definitions of the  $U$ ,  $m$ , and  $V$  matrices.

The  $m$  matrix will now simply be adjusted to accommodate the extra mass eigenstate splitting as shown in Equation 5.2. Again, we have defined  $\Delta m_{ij}^2 \equiv m_i^2 - m_j^2$ .

$$m_s = \begin{pmatrix} 0 & 0 & 0 & 0 \\ 0 & \frac{\Delta m_{21}^2}{2E} & 0 & 0 \\ 0 & 0 & \frac{\Delta m_{31}^2}{2E} & 0 \\ 0 & 0 & 0 & \frac{\Delta m_{41}^2}{2E} \end{pmatrix} \quad (5.2)$$

The  $U$  matrix must also be adjusted to incorporate the extra mixing angle between  $\nu_4$  and  $\nu_1$ . Ignoring the CP violation phases, we get a matrix as shown in Equation

5.3. Here,  $c_{ij} \equiv \cos \theta_{ij}$  and  $s_{ij} \equiv \sin \theta_{ij}$ .

$$U_s = \begin{pmatrix} c_{12}c_{13}c_{14} & s_{12}c_{13}c_{14} & s_{13}c_{14} & s_{14} \\ -s_{12}c_{23} - c_{12}s_{23}s_{13} & c_{12}c_{23} - s_{12}s_{23}s_{13} & s_{23}c_{13} & 0 \\ s_{12}s_{23} - c_{12}c_{23}s_{13} & -c_{12}s_{23} - s_{12}c_{23}s_{13} & c_{23}c_{13} & 0 \\ -c_{12}c_{13}s_{14} & -c_{13}s_{12}s_{14} & -s_{13}s_{14} & c_{14} \end{pmatrix} \quad (5.3)$$

Finally, the matter potential term needs to be modified because only the active neutrino flavours take part in the neutral current interactions and so this cannot be ignored as it is in the active neutrino case. The new matter potential matrix is shown in Equation 5.4.

$$V_s = \begin{pmatrix} V_{CC} + V_{NC} & 0 & 0 & 0 \\ 0 & V_{NC} & 0 & 0 \\ 0 & 0 & V_{NC} & 0 \\ 0 & 0 & 0 & 0 \end{pmatrix} \quad (5.4)$$

where

$$V_{CC} = \sqrt{2}G_f N_e \quad (5.5)$$

and

$$V_{NC} = -0.5\sqrt{2}G_f N_n \quad (5.6)$$

To explore the behaviour of the sterile model, the problem will be reduced to only two active neutrino mass eigenstates as was done in Chapter 2. The results in this thesis do a full treatment of the three active neutrinos which results in a more

accurate determination of the allowed regions of the sterile parameters. However for simplicity we will explore the more compact two active neutrino equations, which still illustrate the basic properties of the model. A further discussion of the derivation of these equations is in [104].

In the analysis of the sterile model parameters, the sterile neutrino is in the fourth position as described above. However, in order to keep the notation for the sterile model consistent with [104, 105], we will now consider the sterile state to be in the zero position such that  $\nu_4 \rightarrow \nu_0$ . This is simply a redefinition of the position of the sterile state and will not affect the behaviour of the model.

### The Hamiltonian in the Matter Basis with Sterile Neutrinos

As was the case for the active neutrino case in Chapter 2, we will diagonalize the Hamiltonian in the flavour basis and have an effective mixing angle  $\theta_m$ . We will then show the Hamiltonian in the mass basis to determine how the mass eigenstates propagate. To reiterate, the sterile mass eigenstate here is denoted as  $\nu_0$ . This rotated Hamiltonian in the mass matter basis, taken from [105], is shown in Equation 5.7.

$$i \frac{d}{dt} \begin{pmatrix} \nu_0 \\ \nu_1 \\ \nu_2 \end{pmatrix} = H_{ms} \begin{pmatrix} \nu_0 \\ \nu_1 \\ \nu_2 \end{pmatrix} \tag{5.7}$$

where  $H_{ms}$  is a symmetric matrix shown in Equation 5.8

$$H_{ms} = \frac{1}{4E} \begin{pmatrix} 0 & -\frac{\Delta m_{01}^2}{2E} \sin \alpha \cos(\theta - \theta_m) & -\frac{\Delta m_{01}^2}{2E} \sin \alpha \sin(\theta - \theta_m) \\ \dots & \lambda_1 - \frac{m_0^2}{2E} & 0 \\ \dots & \dots & \lambda_2 - \frac{m_0^2}{2E} \end{pmatrix} \quad (5.8)$$

and

$$\lambda_1 = m_1^2 + m_2^2 + 2EV_{CC} - \sqrt{(\Delta m_{21}^2 \cos 2\theta - 2E(V_{CC} + 2V_{NC}))^2 + (\Delta m_{21}^2 \sin 2\theta)^2} \quad (5.9)$$

$$\lambda_2 = m_1^2 + m_2^2 + 2EV_{CC} + \sqrt{(\Delta m_{21}^2 \cos 2\theta - 2E(V_{CC} + 2V_{NC}))^2 + (\Delta m_{21}^2 \sin 2\theta)^2} \quad (5.10)$$

There exist two resonance conditions between the  $\nu_0$  and  $\nu_1$  state, one in densities above the active neutrino resonance and one below. Effects from the higher density resonance region can be ignored since relevant solar neutrinos are produced at lower energies than the critical energy for this resonance [104]. The neutrino energy which satisfies the relevant active-sterile resonance condition is as shown in Equation 5.11 [104].

$$E_{\nu S} = \frac{0.5m_1^2 + \Delta m_{01}^2 \cos^2 \alpha}{V_{CC} + 2V_{NC}} \times \frac{1 - R_{\Delta}}{1 - 2R_{\Delta} + \xi \cos 2\theta + \sqrt{(1 - 2R_{\Delta} + \xi \cos 2\theta)^2 - 4R_{\Delta}(1 - R_{\Delta})(\xi^2 - 1)}} \quad (5.11)$$

where,

$$\xi = \frac{V_{CC}}{V_{CC} + 2V_{NC}} \quad (5.12)$$

Equation 5.13 determines how the electron neutrino maps to the mass eigenstate values in the matter basis. This is important in determining the conditions of the initial mass eigenstates, which will have an effect on the final observed number of electron neutrinos.

$$\nu_e = \sin \theta_m^0 \nu_{2m} + \cos \theta_m^0 \cos \alpha_m^0 \nu_{1m} + \cos \theta_m^0 \sin \alpha_m^0 \nu_{0m} \quad (5.13)$$

Equation 5.13 introduces the  $\alpha_m$  parameter, which is similar in behaviour to the  $\theta_m$  described in Chapter 2, except that it is sensitive to the active-sterile resonance condition in Equation 5.11. The 0 superscript denotes the matter mixing angle for the density where the neutrino was produced.

An effect which we ignored for the active neutrinos, which will now play a role for the sterile case, is how the mixing angle affects the adiabaticity when crossing the resonance condition. We will first explore some equations related to the active neutrinos, taken from [47]. Equation 5.14 shows the mass squared difference in the matter basis for the active neutrinos at the resonance.

$$\Delta m_M^2|_R = \Delta m^2 \sin 2\theta \quad (5.14)$$

If the mixing angle  $\theta$  in Equation 5.14 was very small, then the  $\Delta m_M^2$  at the resonance would be small. For active neutrinos, it is possible to define an adiabaticity parameter as in Equation 5.15. If  $\gamma \gg 1$ , then the evolution is adiabatic and there

are no transitions between mass eigenstates at the resonance. However, Equation 5.14 says that  $\Delta m_M^2$  is small at the resonance if  $\theta$  is small, so this would make  $\gamma$  small as well. Thus, for small angles, the resonance crossings are not adiabatic and there is a possibility of eigenstate mixing.

$$\gamma = \frac{(\Delta m_M^2)^2}{2E \sin 2\theta_M |dV_{CC}/dx|} \quad (5.15)$$

For active neutrinos,  $\theta$  is large and so adiabaticity holds. The parameter space being explored for sterile neutrinos, however, has a much smaller mixing angle.  $\alpha$  behaves in much the same way as  $\theta$ , and so  $\gamma$  is also applicable to the sterile mixing case, with some necessary adjustments for a dependence on  $V_{NC}$  in addition to  $V_{CC}$ . Thus, a small angle  $\alpha$  will violate adiabaticity.

### 5.3 The Effect of Sterile Neutrino Mixing on Active Neutrino Observables

If sterile neutrinos could mix with active neutrino flavours they would produce a deficit in the rate of detected active neutrinos. This section will explore how sterile-active mixing will affect the  $P_{ee}$  curve. First, a description of the code which produces the survival probabilities will be given. Finally, the characteristics of the dip in  $P_{ee}$  caused by active-sterile mixing will be examined.

### 5.3.1 Producing Survival Tables with Neutrino4f

In order to investigate the sensitivity of solar neutrino experiments to a sterile neutrino model, a code was developed to generate the predicted electron neutrino survival probability in the presence of a sterile neutrino. The survival probabilities can then be used to predict observables, such as the rate of detected neutrinos, and these predicted observables can be compared to actual measurements.

In order to calculate neutrino survival probabilities, a code was developed from an existing three neutrino propagation code. This three neutrino propagation code, called Neutrino3f, was written by Ryan Martin for his MSc thesis. Complete details of that code's development can be found in [106]. In order to adapt Neutrino3f into a code that considers sterile neutrinos, the oscillation equations in the code were replaced with equations 5.2 - 5.4. Since the code now accommodates the extra sterile neutrino flavour, it is called Neutrino4f.

Neutrino4f simulates a neutrino in the Sun in a position that is generated randomly from the radial distribution which is specific to each neutrino type. The neutrino is then propagated through the Sun. At each step, the flavour basis is converted to the mass eigenstate basis, the neutron and electron densities are determined at the current position, and the Hamiltonian is calculated using Equation 5.7 to propagate the neutrino forward in time.

Figure 5.1 shows the effect of the presence of a sterile neutrino on the active neutrino behaviour for specific parameters of the 3+1 model. The oscillation behaviour without sterile neutrinos is commonly referred to as the MSW solution, or the LMA (large mixing angle) solution. Allowing the active neutrinos to oscillate into a sterile state produces a dip in the survival probability curve. A larger mixing angle between

active and sterile states will result in a larger amplitude of the dip, as seen in the bottom panel of Figure 5.1. A larger mass squared difference between the active and sterile states will result in the dip occurring at a higher neutrino energy, as seen in the top panel of Figure 5.1. The increase in  $\Delta m_{01}^2$  is not linearly proportional to the increased energy of the dip, as can be seen in Equation 5.11.

Using Neutrino4f, survival tables are created for each value of  $R_\Delta$  and  $\alpha$ , and for each neutrino species (ex. pep,  $^8\text{B}$ , etc). For the tables which were used to produce Figure 5.1, the active neutrino values were fixed to be the best fit values from the Particle Data Group [36]. The active neutrino parameters were set to  $\sin^2 2\theta_{12}=0.857$ ,  $\sin^2 2\theta_{13}=0.098$ ,  $\sin^2 2\theta_{23}=0.95$ ,  $\Delta m_{21}^2=7.5\times 10^{-5}$  eV<sup>2</sup>, and  $\Delta m_{31}^2=-2.32\times 10^{-3}$  eV<sup>2</sup>.

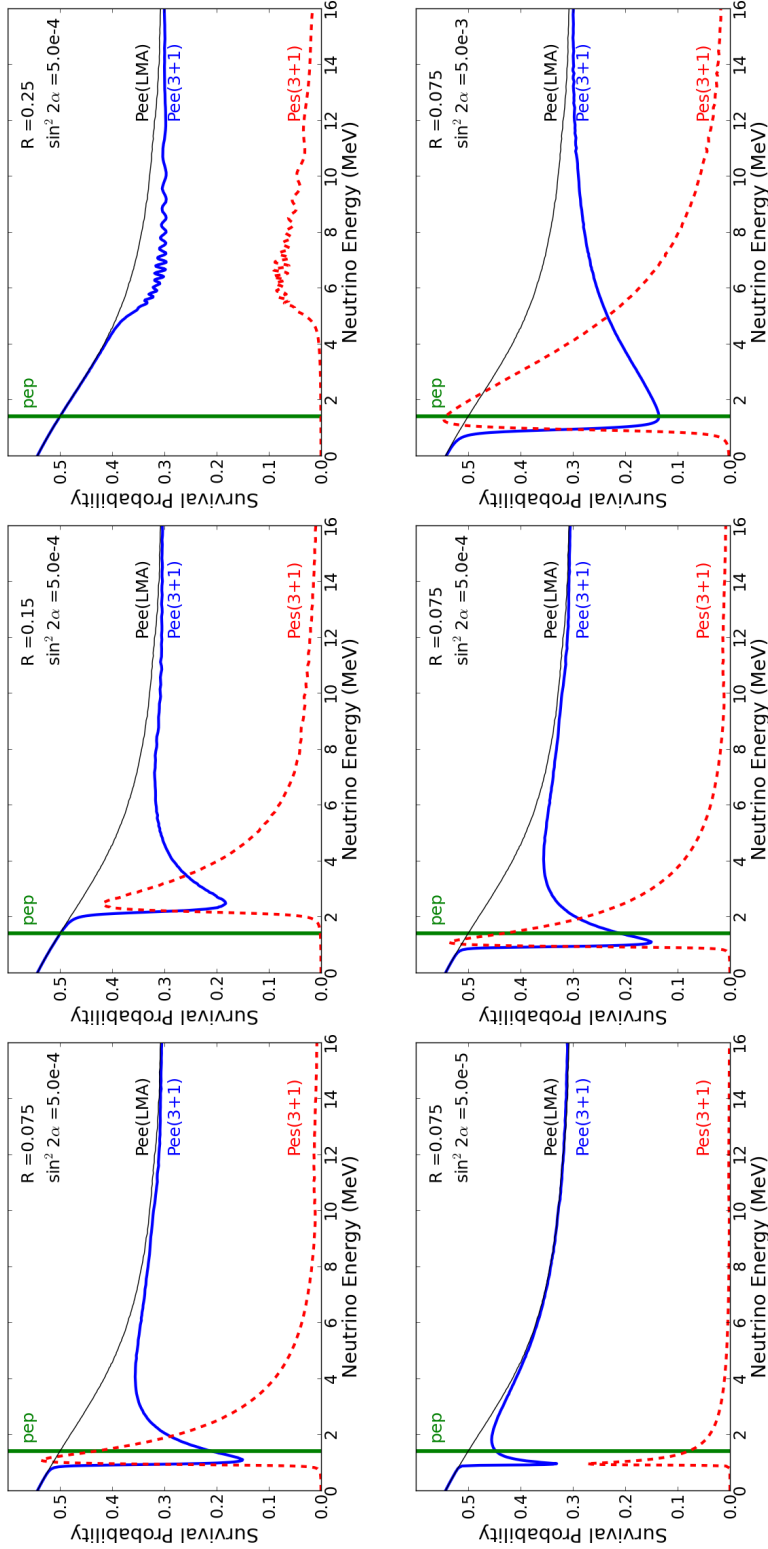


Figure 5.1: The distortion of the electron neutrino survival probability curve under the presence of sterile neutrino mixing. The survival probability curve with no sterile neutrino mixing (the LMA solution) is displayed with a black line. The electron neutrino survival probability for the 3+1 model is the blue solid line. The probability of an electron neutrino being detected as a sterile neutrino, or the  $P_{es}$ , is shown as the dotted red line. The energy of the pep neutrino is displayed as a vertical green line. The top panel shows three values of  $R$ , which are proportional to  $\Delta m_{01}^2$ . As  $R_\Delta$  increases, the energy where the dip occurs also increases. The bottom panel shows the effect of increasing  $\alpha$ . As  $\alpha$  increases, so does the depth of the dip. Wiggles in the survival probability can be seen for the largest value of  $R_\Delta$  plotted here ( $R_\Delta = 0.25$ ).

### 5.3.2 The Topology of the Dip in Electron Neutrino Survival Probability

We will consider three cases to explain the physics behind the features in the dip in survival probability.

#### Changing Energy

In the first case, we will fix  $\Delta m_{01}^2$  and  $\alpha$  and look at what happens as the neutrino energy is varied. As an example, we will use the top left plot in Figure 5.1 where the values of  $R_\Delta$  and  $\alpha$  are fixed to  $R_\Delta=0.075$  and  $\sin^2 2\alpha=5.0 \times 10^{-4}$ .

Neutrinos that are lower in energy than the dip ( $E < 0.5$  MeV in the top left panel of Figure 5.1), are insufficient in energy to see an effect from either the active ( $\nu_1$ - $\nu_2$ ) or active-sterile ( $\nu_0$ - $\nu_1$ ) resonance condition. Thus, at the production regions of these neutrinos  $\theta_m^0 \approx \theta_{12}$  and  $\alpha_m^0 \approx \alpha \approx 0$ , and so the neutrinos will not see an effect from active-sterile mixing.

Neutrinos which are higher in energy than the dip ( $E > 8$  MeV in the top left panel of Figure 5.1) are produced at densities much higher than both the active and the active-sterile resonance conditions. Thus, from Equation 2.22,  $\theta_m^0 \approx 90^\circ$  and so most of the neutrinos are produced in a  $\nu_2$  state. Because there is no mixing between the  $\nu_2$  and the  $\nu_0$  state, these higher energy neutrinos do not see an effect from sterile-active mixing.

Neutrinos which are produced at densities between, or near, the active and the active-sterile resonances can produce a dip in  $P_{ee}$ . In the maximal case ( $E \sim 1$  MeV in the top left panel of Figure 5.1), the neutrino is produced at a lower density than the  $\nu_1$ - $\nu_2$  resonance such that  $\theta_m^0 \approx \theta_{12}$  and at a higher density than the  $\nu_0$ - $\nu_1$

resonance such that  $\alpha_m^0 \approx 90^\circ$ . This situation represents the maximal probability of the electron neutrino being in the  $\nu_0$  state because  $\theta_m^0 \approx \theta$  and so there is the lowest possible probability of the neutrino being in the  $\nu_2$  state. Since  $\alpha_m^0 \approx 90^\circ$ , there is a very low probability of the neutrino being in the  $\nu_1$  state and so there is the maximal probability of the neutrino being a  $\nu_0$ . Neutrinos which are lower in energy than this maximal case see an  $\alpha_m^0 < 90^\circ$ , and so neutrinos which are not produced in a  $\nu_2$  state have a higher probability of being in the  $\nu_1$  state (and therefore have a lower probability of being in the  $\nu_0$  state). Neutrinos which are higher in energy than the maximal case see  $\theta_m^0 > \theta$  while still having  $\alpha_m^0 \sim 90^\circ$ , and so there is a higher probability for the neutrino to be produced in the  $\nu_2$  state, which again translates into a lower probability of being produced in the  $\nu_0$  state.

### Changing $\Delta m_{01}^2$

Now we will examine the overall effect of increasing  $\Delta m_{01}^2$ . This is shown in the top three plots in Figure 5.1. Increasing  $\Delta m_{01}^2$  will result in higher neutrino energies satisfying the  $\nu_0$ - $\nu_1$  resonance condition described in Equation 5.11, which means that the energy where the dip is maximal will also increase. As the critical energy for the  $\nu_0$ - $\nu_1$  resonance condition increases, there will be an increasingly larger effect from the  $\nu_1$ - $\nu_2$  resonance such that  $\theta_m^0$  will not necessarily be equivalent to  $\theta_{12}$  when  $\alpha_m^0 \gg \alpha$ . This will result in a higher probability of the electron neutrino being in the  $\nu_2$  state, which means a lower probability for the neutrino to be in the  $\nu_0$  state, and thus the dip will be shallower.

### Changing $\alpha$

The effect of increasing  $\alpha$  is shown in the bottom panel of Figure 5.1. When  $\alpha$  is small, adiabaticity is violated as explained in Section 5.2. Therefore, at smaller values of  $\alpha$ , there is a larger probability of neutrinos produced in the  $\nu_0$  state to transition to the  $\nu_1$  state as they cross the resonance, which produces a sharper and deeper dip. For larger  $\alpha$ , the resonance is crossed adiabatically and so more of the neutrinos produced in the  $\nu_0$  state will remain in the  $\nu_0$  state. This produces a wider dip with a lower minimum value.

### Wiggles at High $R_\Delta$ Values

The last feature which will be explained are the wiggles that are visible when  $\Delta m_{01}^2$  is high. The main points of the discussion on the origin of these wiggles, as outlined in [105], will be presented here. The wiggles which occur for high  $R_\Delta$ , low  $\alpha$  are due to the interference between two modes of obtaining a  $\nu_1$  state. The first mode is when  $\nu_{1m} \rightarrow \nu_1$  and the other is when  $\nu_{0m} \rightarrow \nu_1$ , which is realized when the neutrino passes over the resonance region non-adiabatically. At high  $R_\Delta$  values, there is a higher probability of the neutrino being produced in the  $\nu_1$  state because  $\alpha_m^0 < 90^\circ$ . At low  $\alpha$ , the adiabaticity is violated and so there is a probability for neutrinos created in the  $\nu_0$  state to transition to the  $\nu_1$  state. This interference leads to wiggles with large period over the energy scale, and thus they are not averaged out when you take the production region into account.

## 5.4 The Global Fit Code

The code used to determine the best fit parameters for the sterile model using solar neutrino data was first developed for the SNO experiment to extract active neutrino parameters. A detailed discussion of the code can be found in [58].

### 5.4.1 Solar Neutrino Experimental Inputs

Solar neutrino experiments give important constraints on the extent to which a sterile neutrino can play a role in the behaviour of active neutrino oscillations. In Chapter 2, solar neutrino experiments were introduced to describe their historical importance in the field of neutrino physics. In this section, past solar experiments will be described in the context of their results to motivate how these findings are used to make a global fit of sterile parameters. For a full listing of the results used in this analysis, see the appendix of [58].

#### Radiochemical Experiments

As discussed in Chapter 2, early solar neutrino experiments used radiochemical methods for neutrino detection. There are two main types of radiochemical experiments: those that used chlorine as a target and those that used gallium. In both cases, the experiment would be sensitive to all solar neutrinos above the threshold for the reaction.

The first solar neutrino experiment, Homestake [12], used perchlorethylene as a detector target and looked for the inverse beta decay reaction which converted the chlorine to argon as in Equation 5.16. The Homestake detector is shown in Figure 5.2. The argon atoms were then extracted and counted to determine the

overall reaction rate of solar neutrinos. The energy threshold for detecting neutrinos using this reaction is 0.81 MeV [15]. The Homestake reaction threshold was just below the energy of the  ${}^7\text{Be}$  neutrino, however because of the higher cross section at higher energies, Homestake was mostly sensitive to  ${}^8\text{B}$  neutrinos. The rate from the Homestake experiment used in this analysis is  $2.56 \pm 0.23$  SNU, taken from [107], where a solar neutrino unit (SNU) is defined as  $10^{-36}$  events  $\text{atom}^{-1}\text{s}^{-1}$ .

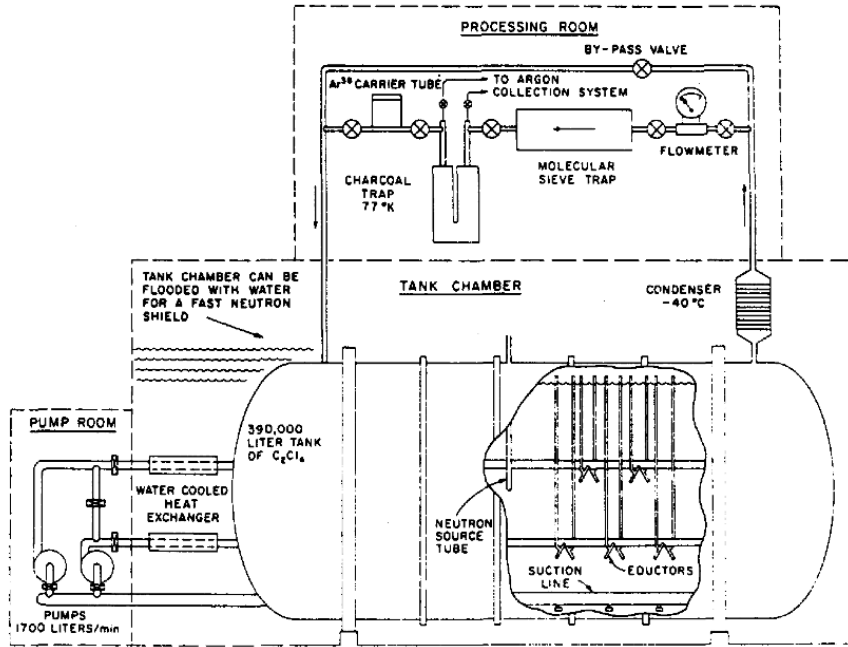


Figure 5.2: Schematic of the Homestake detector [108]

Following the Homestake experiment, a radiochemical experiment which used gallium rather than chlorine was proposed [109], mainly due to the lower reaction threshold which would make the experiment sensitive to pp neutrinos which are the most

abundant type of neutrino and thus would greatly improve the statistics of the experiment. Additionally, the pp solar neutrino is at the start of the pp thermonuclear chain in the Sun and therefore has a very small uncertainty in the solar model. A gallium experiment measures the inverse beta decay which converts gallium to germanium through the reaction described in Equation 5.17.



This proposal led to the SAGE [18] and GALLEX [17] experiments, and later to the GNO experiment [20], all of which used gallium as a target material to detect solar neutrinos. The threshold for this reaction to occur is 0.233 MeV, so gallium experiments detect mostly pp neutrinos. Figure 5.3 shows the SAGE detector and the GALLEX/GNO detector. The global analysis code uses a combined result from these three experiments, which gives a rate of  $66.1 \pm 3.1$  SNU [110].

### Water Cherenkov Experiments

As the name suggests, water Cherenkov experiments see signals from neutrino interactions via the emission of Cherenkov radiation. This happens when the neutrino enters the detector and interacts with a charged particle. The particle then has a velocity which is greater than the speed of light in the medium and emits Cherenkov light in a cone. These experiments can extract the neutrino energy and incoming neutrino direction.

SNO and Super-Kamiokande (SK) are water Cherenkov experiments. The detector schematic can be seen for both detectors in Figure 5.4. These detectors rely on large volumes of water and many photomultipliers which view the active volume to

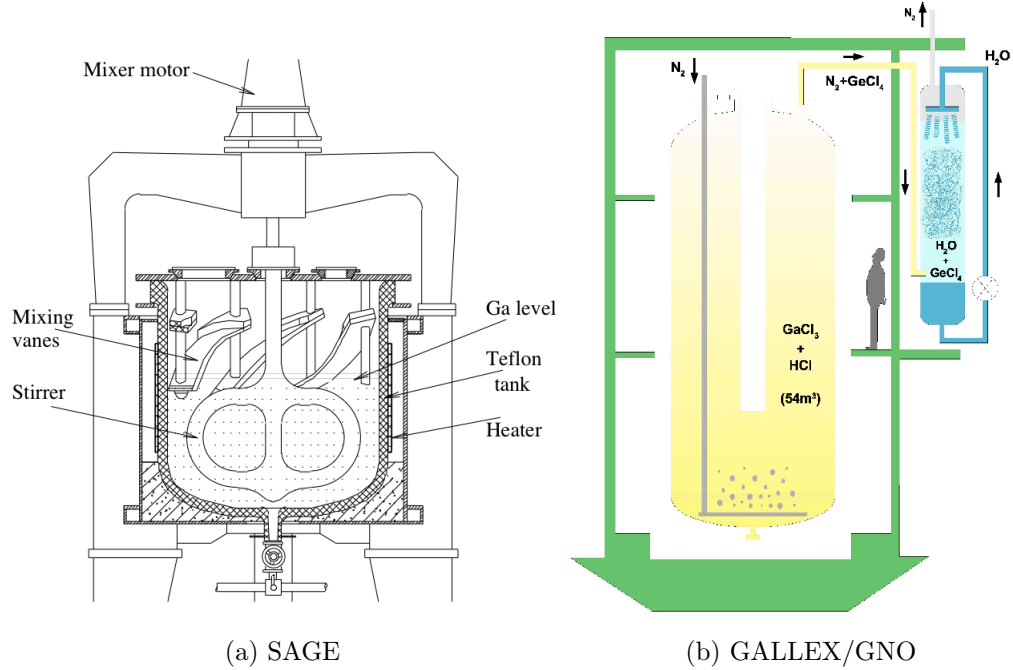


Figure 5.3: A schematic drawing of the SAGE [18] and GALLEX/GNO [111] experiments.

make neutrino measurements.

SK is sensitive to elastic scattering between the incoming  $^8\text{B}$  neutrinos and electrons in the detector. This elastic scattering reaction is sensitive to all flavours of neutrinos, however the cross section for the electron neutrino is six times higher than that of the muon or tau neutrino. The signal from SK is an electron recoil energy spectrum binned in energy and zenith angle (for SK I) or binned in energy and day/night (for SK II and SK III). The three phases of the Super-Kamiokande experiment report data with electron recoil energies from 5.0 MeV - 20.0 MeV (SKI) [113], 7.0 MeV - 20 MeV (SKII) [114], and 5.0 MeV - 20.0 MeV (SKIII) [103].

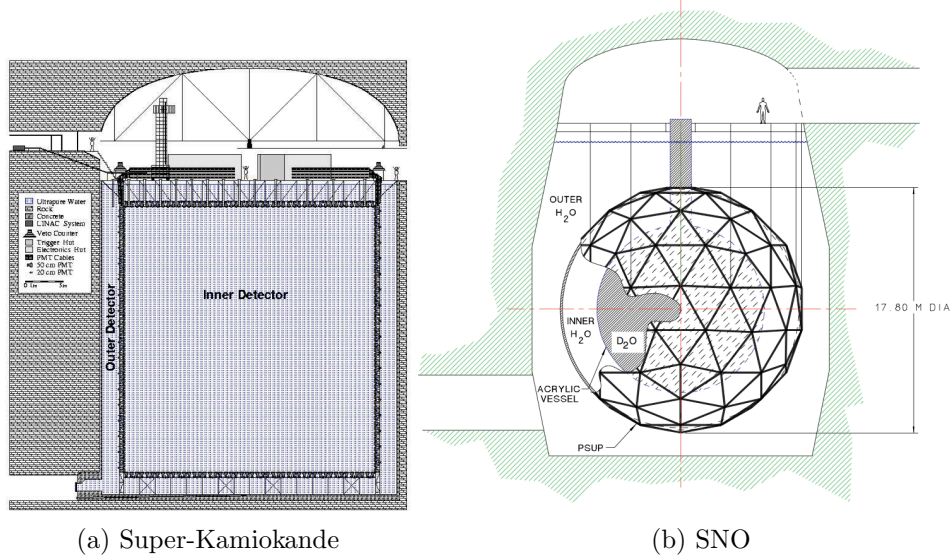


Figure 5.4: A schematic drawing of the water Cherenkov experiments: Super-Kamiokande [112] and SNO [63].

SNO was mostly sensitive to charged current reactions involving  $^8\text{B}$  electron neutrinos and deuterium (as shown in Equation 5.18) and neutral current reactions involving all neutrino types (as shown in Equation 5.19) reactions. SNO also measured events from elastic scattering between neutrinos and electrons, but the statistics for this signal is much higher in the SK measurement and so only the SK result is used in the overall global analysis.



The neutral current reaction in SNO gives a measurement of the overall active neutrino flux. The charged current reaction gives a measurement of the electron

neutrinos which interact in the detector, which can be used to construct an electron neutrino survival probability when divided by the neutral current flux. The SNO results are treated differently from the other experimental results in the global analysis. This is described more extensively in Section 5.4.2 and so the final results which are used in the fit are given there.

### Liquid Scintillator Experiments

Borexino is a liquid scintillator experiment which is currently running at Gran Sasso National Laboratory in Italy [115]. Figure 5.5 shows the detector set up. Borexino uses pseudocumene with 1.5 g/L PPO as a scintillator and was primarily built to be a solar neutrino experiment.

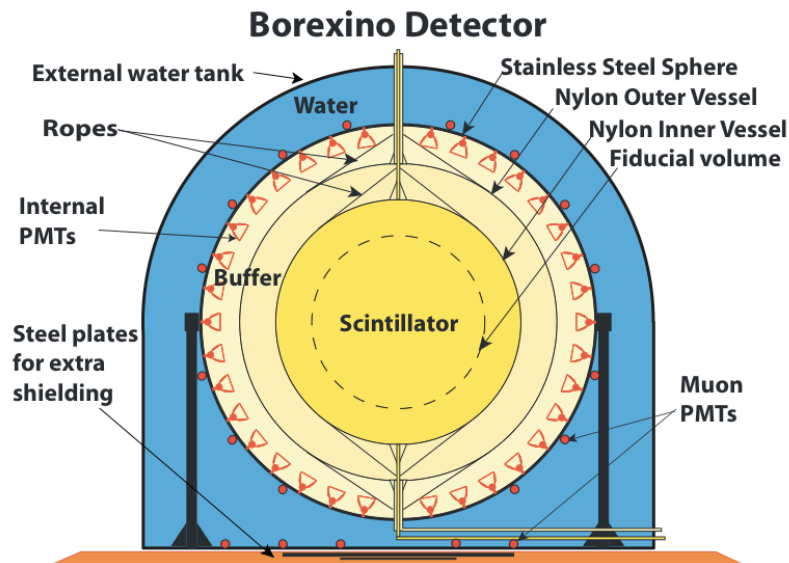


Figure 5.5: Schematic of the Borexino detector [115]

Like SNO+, Borexino detects neutrinos through elastic scattering interactions between the neutrino and the electrons in the scintillator. As was the case for SK, Borexino is sensitive to all three flavour types though the cross section is higher for electron neutrinos. Borexino can observe lower energy neutrinos than water Cherenkov experiments, but cannot reconstruct the direction of the neutrino.

In 2007, Borexino made a first measurement of the 0.862 MeV  ${}^7\text{Be}$  solar neutrinos [53]. In 2011, Borexino reported an improved result of  $46.0 \pm 2.2$  counts/day/100 tons [116], which is used in this global fit. Borexino has also made a measurement of the pep solar neutrino rate [54]. This rate measurement is considered in the global fit code, though it has a large uncertainty and thus has little effect on the allowed parameters of the sterile neutrino model. The Borexino pep measurement is also treated differently from the other rate experiments, as outlined in Section 5.4.6.

### 5.4.2 Treatment of Experimental Observables in the Global Fit Code

Generally speaking, the observables from solar neutrino experiments fall into four categories: experiments which report an overall rate above a reaction threshold (Homesite and gallium experiments, SNO neutral current measurement), experiments which measure a rate from elastic scattering reactions due to a monoenergetic neutrino source (SNO+ pep, Borexino  ${}^7\text{Be}$  and pep), experiments which report an elastic scattering rate which has some sensitivity to energy and/or zenith angle (SK), and SNO charged current rates, which reports its findings as the coefficients of a polynomial which describes the shape of the electron neutrino survival probability.

Rate experiments, both ones that quote a rate binned in energy and that quote

an overall rate, also report their predicted rates if there were no neutrino oscillation effects (ie. if all electron neutrinos produced in the Sun were detected as electron neutrinos on Earth). This is particularly helpful because it can normalize the oscillated results to remove any detector effects which are not made publicly available in the collaboration's publications. Thus, the observable for every experiment except SNO and Borexino pep is treated as a fractional observable,  $R_f^{exp}$ , which is shown explicitly in Equation 5.20. Here,  $R^{exp}$  is the measured rate and  $R^{pred}$  is the predicted rate if  $P_{ee} = 1$ .

$$R_f^{exp} = \frac{R^{exp}}{R^{pred}} \quad (5.20)$$

For SNO, the measurement is expressed as a parameterized, model-independent electron neutrino survival probability, which is calculated from the charged-current events divided by the neutral current events. This is entered into the global fit as a polynomial function with the form of Equation 5.21 [37].

$$P_{ee} = c_0 + c_1(E_\nu - 10[MeV]) + c_2(E_\nu - 10[MeV])^2 \quad (5.21)$$

Additionally, there are two parameters which describe the difference between the number of neutrinos detected during the day and during the night (known as the day-night asymmetry). This is shown in Equation 5.22.

$$A_{ee}(E_\nu) = a_0 + a_1(E_\nu - 10[MeV]) \quad (5.22)$$

Figure 5.6 shows the fit of  $P_{ee}$  and  $A_{ee}$  from the SNO data.

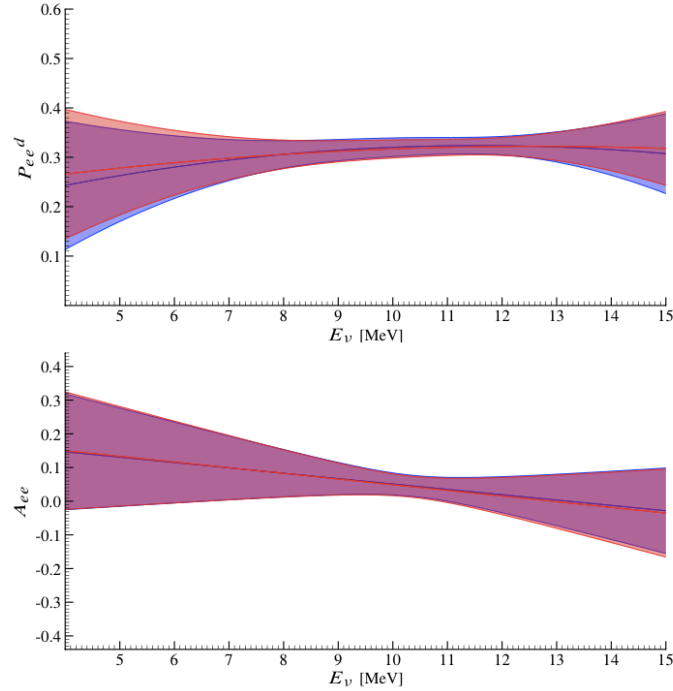


Figure 5.6: The fit of the SNO data using the polynomial  $P_{ee}$  and the day-night asymmetry function  $A_{ee}$ . The red band is the result using the maximum likelihood method and the blue band is the result using Bayesian analysis. The solid red and blue lines represent the best fit values from the maximum likelihood method and the Bayesian method respectively. [37]

The scale of the neutral current flux,  $f_{sB}$ , is also used as an extracted experimental parameter, though it is highly correlated with some of the parameters from the polynomial.

The best fit parameters for the  $^8\text{B}$  neutrino flux, as well as the polynomial coefficients, is shown in Table 5.1.

Table 5.1: Best Fit Values for the SNO Experimental Observables [37]

Parameter	Best Fit	Uncertainty
$\Phi_B$	$5.25 \times 10^6 \text{cm}^{-2} \text{s}^{-1}$	${}^{+0.11}_{-0.13} \times 10^6 \text{cm}^{-2} \text{s}^{-1}$
$c_0$	0.317	$\pm 0.009$
$c_1$	0.00039	$\pm 0.0045$
$c_2$	-0.0010	${}^{+0.0014}_{-0.0016}$
$a_0$	0.046	${}^{+0.014}_{-0.013}$
$a_1$	-0.016	${}^{+0.010}_{-0.011}$

### 5.4.3 Treatment of Theoretical Observables in the Global Fit Code

We will now turn our attention to constructing theoretical observables which we can compare with the experimental observables to see how closely our model predicts the data.

In the case where the experimental observable is an overall rate that is sensitive only to electron neutrinos and contains no energy information, as is the case with the radiochemical experiments, the theoretical rate for a neutrino type  $\nu_i$  (where  $i$  is pep,  ${}^7\text{Be}$ , etc.) is given by Equation 5.23, where  $\phi_{\nu_i}$  is the flux normalized spectrum shape for the given neutrino type and  $\sigma$  is the cross section for the interaction. The cross section will be zero below the reaction threshold for the experiment.  $N$  contains normalization factors such as live-time and capture efficiency effects.

$$R_{\nu_i}^{th} = N \int_0^\infty P_{ee}(E_\nu) \phi_{\nu_i}(E_\nu) \sigma(E_\nu) dE_\nu \tag{5.23}$$

For the SNO neutral current rate, there is no energy information and the cross section is the same for all active neutrinos. Thus, the theoretical rate can be calculated

with Equation 5.24. Here,  $\sigma$  is the cross section which is specific to the SNO neutral current reactions and  $P_{ex} = P_{ee} + P_{ea}$  where  $P_{ex}$  is the probability that an electron neutrino created in the Sun is an active neutrino when it reaches the detector,  $P_{ee}$  is the electron neutrino survival probability, and  $P_{ea}$  is the probability the electron neutrino is a muon or tau neutrino at the detector.

$$R_{\nu_i}^{th} = N \int_0^\infty P_{ex}(E_\nu) \phi_{\nu_i}(E_\nu) \sigma(E_\nu) dE_\nu \quad (5.24)$$

For the experiments that detect neutrinos through elastic scattering (like the Borexino  $^7\text{Be}$  measurement, SK, and SNO+), the theoretical rate for a neutrino type  $\nu_i$  is given by Equation 5.25, where  $T_e$  is the actual kinetic energy of the observed electron,  $T$  is the detected electron energy,  $\Delta T$  is the energy bin width in detected electron energy, and  $R$  is the detector response function. The electron neutrino survival probability values,  $P_{ee}$ , and the electron-muon/tau probability,  $P_{ea}$ , are taken from the tables generated by the Neutrino4f code. The detector response function is related to the detector resolution. The response function is specific to each experiment and is usually provided by the collaborations. The cross-section here is the elastic scattering cross section which is different for electron and muon/tau neutrinos, thus denoted  $\sigma_e$  and  $\sigma_a$ .

$$R_{\nu_i}^{th} = R_e^{th} + R_a^{th} \quad (5.25)$$

where

$$R_y^{th} = N \int_0^\infty \phi_{\nu i}(E_\nu) P_{ey}(E_\nu) \int_0^\infty \frac{d\sigma_y}{dT_e}(E_\nu, T_e) \int_T^{T+\Delta T} R(T_e, T') dT' dT_e dE_\nu \quad (5.26)$$

Some experiments see multiple neutrino types (ex. pep, pp, etc) that contribute to the overall rate, so the theoretical observable in that case is ultimately compared with the experimental value is actually a sum of rates,  $R_f^{th}$  as shown in Equation 5.27. Again, the model-dependent effects have been removed by dividing by the unoscillated theoretical rate where  $P_{ee} = 1$ .

$$R_f^{th} = \sum_i \frac{R_{\nu i}^{th}}{R_{\nu i}^{th}|_{P_{ee}=1}} \quad (5.27)$$

For SNO, the method of generating the theoretical observables is different than the other experiments. The global fit code contains a Monte Carlo-generated detected neutrino energy spectrum without oscillation effects for the SNO experiment. For each combination of  $\alpha$  and  $R_\Delta$ , the survival probabilities from Neutrino4f are used to distort the spectrum in order to fit the five parameters of the  $P_{ee}$  polynomial [58]. Therefore, the theoretical observables for SNO are the five polynomial parameters ( $c_0$ ,  $c_1$ ,  $c_2$ ,  $a_0$ , and  $a_1$ ) that are determined using the method described above, and the overall expected  ${}^8\text{B}$  neutrino flux that is taken from the standard solar model.

#### 5.4.4 Propagation of Uncertainties

In the case of experimental observables, the systematic uncertainties are usually provided with the published results (for example, in the form of a correlation matrix).

For the theoretical uncertainties, there are often errors which affect the results for multiple neutrino experiments. The treatment of these errors are outlined in [58]. The SNO neutral current measurement allows for a more accurate indication of the total  ${}^8\text{B}$  neutrino flux than the standard solar model and thus the neutral current measurement, once corrected for  $P_{ex}$ , is used to constrain the total  ${}^8\text{B}$  flux. The uncertainties in the  ${}^8\text{B}$  neutrino spectrum shape, which affects many of the experiments, is taken from [58]. The fluxes for all of the other neutrino types are fixed and the effect of the uncertainty is determined by the shift and refit method, where the uncertainty is determined by shifting the scale of the parameter to one sigma and refitting. All of the solar model uncertainties are propagated directly with the fractional theoretical rates.

### 5.4.5 Extracting Chi Squared Values

To extract the best fit model parameters and to generate confidence intervals, the method of least squares was used. The equation for chi-squared is shown in Equation 5.28. Here,  $[\sigma_{total}^{-2}]_{nm}$  is the constructed correlation matrix based on the experimental errors provided with the measurements and the errors which are propagated with the theoretical rates. The  $f_i$  terms represent parameters which are allowed to vary away from their best fit values,  $f_i^0$  by their error  $\sigma_{f_i}$ .

$$\chi^2 = \sum_{n,m} (R_n^{exp} - R_n^{theoretical}) [\sigma_{total}^{-2}]_{nm} (R_m^{exp} - R_m^{theoretical}) + \sum_i \left( \frac{f_i - f_i^0}{\sigma_{f_i}} \right)^2 \quad (5.28)$$

To determine the allowed contours, the chi-squared value is calculated for each

combination of parameters  $R_\Delta$  and  $\alpha$ . The overall minimum chi-squared value ( $\chi_{min}^2$ ) is then found and the delta chi-squared value is calculated as  $\Delta\chi^2 = \chi^2 - \chi_{min}^2$ .

To draw the allowed contours, the confidence levels of 68.27%, 95%, and 99.73% were chosen for display. The contours are drawn as  $\Delta\chi^2 < 2.30$  for the 68.27% contour,  $2.30 < \Delta\chi^2 < 5.99$  for the 95% contour, and  $5.99 < \Delta\chi^2 < 11.83$  for the 99.73% contour [36].

### 5.4.6 A note on the Borexino pep measurement

The Borexino pep measurement was treated differently than the other experimental measurements. The Borexino collaboration provided the table of  $\chi^2$  values as a function of pep and CNO neutrino rates that was used to generate Figure 4 in [54]. The CNO neutrino rate was marginalized by finding the lowest  $\chi^2$  for each pep rate. Each pep rate was then converted to a fractional rate observable using the values in Table 1 in [54]. To construct the theoretical observable for each value of  $R_\Delta$  and  $\alpha$ , Equation 5.29 was used. This is a simplified version of Equation 5.25, where there is no need to consider detector responses because that has already been folded into the  $\chi^2$  values in the experimental table. Also, because pep neutrinos are mono-energetic, there is no need to integrate over neutrino energy. This method does not account for flux uncertainties in the model or the uncertainties in the cross sections, though for the pep neutrino and for elastic scattering interactions, these values are quite low.

$$R_f^{th} = \frac{\Phi\sigma_e(1.44MeV)P_{ee} + \Phi\sigma_a(1.44MeV)P_{ea}}{\Phi\sigma_e(1.44MeV)} = P_{ee} + \frac{\sigma_a(1.44MeV)}{\sigma_e(1.44MeV)}P_{ea} \quad (5.29)$$

The theoretical fractional observable,  $R_f^{th}$ , was calculated for each value of  $R_\Delta$

and  $\alpha$  in the sterile model using the  $P_{ee}$  and  $P_{ea}$  tables generated by Neutrino4f. The  $\chi^2$  associated with each  $R_f^{th}$  was determined by looking up the  $\chi^2$  value in the marginalized Borexino table, and performing a linear interpolation if necessary. This was then either taken as the  $\chi^2$  if considering Borexino pep only, or was added on to the total  $\chi^2$  if other experiments were being considered.

## 5.5 Individual Experimental Contributions to the Global Fit

Section 5.6 will show the results from the overall global fit, but first it is illustrative to see how the data from each individual solar neutrino experiment contributes to the overall fit.

### 5.5.1 Radiochemical experiments

If we consider the combined contributions only from radiochemical experiments, which are mostly sensitive to the lower energy pp neutrinos, we will be sensitive to lower values of  $R_\Delta$  in the 3+1 sterile model. Figure 5.7 shows the allowed region of the 3+1 model considering only Homestake and a weighted average for the three gallium experiments.

At low alpha values ( $\sin^2 2\alpha < 10^{-3.6}$ ), the effect of the sterile neutrino is insufficient (at the one sigma level) to change the expected rate for the radiochemical experiments.

For low  $R_\Delta$ /high  $\alpha$  ( $R_\Delta < 0.06$ ,  $\sin^2 2\alpha > 10^{-3.6}$ ), the effect of adding the sterile

neutrino is sufficient to affect the rate of the pp neutrinos, which will affect the measurement of the gallium experiments. Thus, radiochemical experiments can weakly constrain the low  $R_\Delta$ / high  $\alpha$  parameter space.

For high values of  $R_\Delta$  ( $R_\Delta > 0.06$ ), adding the sterile neutrino will affect active neutrinos which are higher in energy than the pp neutrino. Though radiochemical experiments are able to measure these higher energy neutrinos their measurement is not statistically significant enough (at the one sigma level) to affect the sterile neutrino parameters in that region.

### 5.5.2 Borexino ${}^7\text{Be}$ Measurement

Figure 5.8 shows the favoured regions of the sterile neutrino model when taking into account the Borexino  ${}^7\text{Be}$  neutrino measurement only.

As seen in the figure, the Borexino measurement is sensitive to a similar, though slightly higher, region of  $R_\Delta$  value than the radiochemical experiments because the  ${}^7\text{Be}$  solar neutrino is higher in energy than the pp solar neutrino. Also, because Borexino made a more precise measurement than the radiochemical experiments, it can rule out some of the parameter space at more than three sigma.

As seen in Figure 5.8, the Borexino measurement is sensitive to a lower alpha region ( $\sin^2 2\alpha < 10^{-4}$ ) than the radiochemical measurements, mainly due to the higher precision in the Borexino measurement. For very low values of  $R_\Delta$  ( $R_\Delta < 0.02$ ), the value of alpha needs to be high to affect the Borexino energy region because the main effect is at neutrino energies lower than the  ${}^7\text{Be}$  neutrino and so a large mixing angle is needed to give a very large distortion. As  $R_\Delta$  increases to  $0.02 < R_\Delta < 0.07$ , the main effect of having oscillations to sterile neutrinos is in the  ${}^7\text{Be}$  neutrino energy region, so

a smaller mixing angle will still have a large effect on  ${}^7\text{Be}$  neutrino observations. At  $R_\Delta \sim 0.05$ , the effect of the sterile neutrino mixing is maximal for  ${}^7\text{Be}$  neutrinos, and so the Borexino measurement is sensitive to mixing angles as low as  $\sin^2 2\alpha = 10^{-4}$ . For  $R_\Delta > 0.08$ , the effect of the sterile neutrinos is completely in a higher energy region than the  ${}^7\text{Be}$  neutrinos and so the Borexino measurement cannot be used to constrain the sterile neutrino mixing parameters in that region.

### 5.5.3 SNO and Super-Kamiokande

Figure 5.9 shows the favoured region of the sterile model when considering only the  ${}^8\text{B}$  measurements from SNO and SK.

The SNO and SK experiments are sensitive to a higher neutrino energy than radiochemical experiments and the Borexino  ${}^7\text{Be}$  neutrino measurement, and thus is sensitive to a higher  $R_\Delta$  value in the sterile model. As seen in Figure 5.9, there is an interesting feature where the SNO and SK measurements have excluded the low  $R_\Delta$ /low alpha region at more than one sigma. Each of the two experiments individually fit to the LMA solution within one sigma, but still slightly favour a sterile model. When the result from the two experiments are combined, the disagreement with the LMA solution is stronger and now the data favours this sterile neutrino model at more than one sigma. While this is still not statistically significant enough to be evidence the existence of a sterile neutrino, it does give motivation to looking for sterile neutrinos in the solar neutrino sector.

The most disfavoured region when considering only the SK and SNO data is the region with  $\sin^2 2\alpha > 10^{-2.7}$ ,  $0.06 < R_\Delta < 0.17$ . This is because when the sterile neutrino has mixing parameters in this range, it makes a very large effect in the

active neutrino sector which affects the  $^8\text{B}$  neutrino in the energy range visible to SNO and Super-Kamiokande.

#### 5.5.4 Borexino pep neutrino measurement

The allowed parameters of the 3+1 sterile model when considering only the Borexino pep measurement is shown in Figure 5.10. Because the uncertainty on the Borexino pep rate measurement is so high, the measurement does a poor job of constraining the sterile model parameters.

#### 5.5.5 Future SNO+ pep neutrino measurement

A future SNO+ measurement of the pep neutrinos could help to place further constraints on this sterile model. The pep neutrinos are at 1.44 MeV and so exist in the energy region between the  $^7\text{Be}$  and the  $^8\text{B}$  neutrinos. Thus, the pep neutrino measurement would give information about the intermediate  $R_\Delta$  values in this sterile model.

Figure 5.11 shows how a measurement of the pep neutrino, if it is in agreement with the LMA solution, would affect the 3+1 sterile model after one year of live-time. Because the  $^{11}\text{C}$  background is expected to be lower in the SNO+ detector than the Borexino detector, the pep neutrino rate measurement will have a much lower uncertainty [91]. The anticipated uncertainty on pep neutrino flux measurement after one year of live-time is 9.1 % [91]. Because the pep neutrinos have a low uncertainty in the solar models (2 % flux error in BS05(OP)), a high precision measurement of the flux would place strong constraints on the allowed sterile model parameter values at intermediate  $R_\Delta$ .

As seen in Figure 5.11, the pep neutrino is sensitive to values of  $\sin^2 2\alpha > 10^{-4}$  and values of  $R_\Delta < 0.12$ . The effect of the sterile neutrino mixing is maximal in the pep region for  $R_\Delta \sim 0.8$ .

Because of the high precision of both the anticipated experimental measurement and the theoretical prediction of the pep neutrino flux, this measurement has sensitivity even to low values of  $R_\Delta$  if  $\sin^2 2\alpha > 10^{-3}$ . This is because even though the distortion in the active neutrino sector might not be maximal at the pep neutrino energy for these low  $R_\Delta$  values, if the mixing is sufficiently high there can still be an effect and that will be detected with the one year live-time pep neutrino measurement.

The pep neutrino has the highest region of parameter space that is ruled out to more than three sigma compared with the previous current solar neutrino experimental measurements.

## 5.6 Global fits for Allowed Sterile Neutrino Parameters

Now that the allowed parameter space for the sterile model has been examined for each experiment individually, the results will be combined to give an overall picture of the allowed parameter space given the current solar neutrino measurements. The effect of adding in a pep neutrino measurement to the global fit will also be examined.

For the plots in Section 5.5, the mixing angles and mass squared differences between the active neutrinos were kept fixed to their best fit values. For most of the active parameters, this is reasonable since the best fit values are obtained from data which is independent from this analysis (ie. not solar neutrino experiments). For  $\theta_{12}$ ,

however, the leading contribution to the best fit result is the SNO  $^8\text{B}$  data, which is reused in this analysis to constrain the sterile neutrino parameters. To remove this bias, the value of  $\theta_{12}$  was marginalized in the global fit plots by finding the minimum  $\chi^2$  when  $\theta_{12}$  was varied between  $-1\sigma$  and  $+4\sigma$ , which corresponded to  $\sin^2 2\theta_{12}$  values between 0.832 and 0.949.

### 5.6.1 Global sterile fit with current solar neutrino measurements

In order to get an overall global fit using current solar neutrino experimental data, the experiments described in Section 5.4.1 are combined using the methods described in Section 5.4. Explicitly, the fit includes the rate from the Homestake experiment, the combined rate from the Gallium experiments (SAGE, GALLEX, GNO), the  $^7\text{Be}$  and pep rates from Borexino, the binned energy spectra for  $^8\text{B}$  from SK I, II, and III, and the polynomial expression for the  $P_{ee}$ , as well as the overall flux measurement, from the  $^8\text{B}$  neutrinos in SNO.

As seen in Figure 5.12, the behaviour of the overall global fit is a combination of the plots shown in Section 5.5. At  $R_\Delta < 0.07$ ,  $\sin^2 2\alpha > 10^{-4}$ , the behaviour is mostly dominated by the Borexino  $^7\text{Be}$  neutrino measurement. At higher  $R_\Delta$  ( $R_\Delta > 0.07$ ), the behaviour of the fit is mostly influenced by the SK and SNO  $^8\text{B}$  neutrino measurement. At low  $R_\Delta$  and low alpha ( $R_\Delta < 0.07$ ,  $\sin^2 2\alpha < 10^{-4}$ ), we see the influence from the SK and SNO  $^8\text{B}$  neutrino measurement where the overall model weakly favours sterile neutrino mixing.

## 5.6.2 Global sterile fits with a future SNO+ measurement

To determine how a SNO+ measurement would change the current sterile neutrino picture, a fake measurement was added to the fit. Both the case of one year and two years of SNO+ live-time were considered.

### Global Sterile Fit with One Year pep Measurement

The results are shown in Figure 5.13 for a pep neutrino measurement after one year of SNO+ live-time. The anticipated uncertainty on the one year pep neutrino flux measurement is 9.1 % [91]. As expected, adding in the pep neutrino measurement affected the low and intermediate values of  $R_\Delta$ . As seen in Figure 5.13, most of the region with  $R_\Delta < 0.09$ ,  $\sin^2 2\alpha > 10^{-3.7}$  is excluded at greater than three sigma. Also, the parameter space allowed within one sigma is constrained to  $R_\Delta > 0.12$ .

### Global Sterile fit with Two Year pep Measurement

Figure 5.14 shows the effect of adding in a pep signal after two years of SNO+ running. Again, this assumes that the LMA solution will be measured. The expected uncertainty on the pep flux after two years of live-time is 6.5 % [91].

As seen in Figure 5.14, having an extra year of running increases the area of parameter space which is ruled out compared with the one year of live-time. Now most of the parameter space with  $R_\Delta < 0.1$ ,  $\sin^2 2\alpha > 10^{-3.8}$  is excluded at more than three sigma.

## 5.7 Summary and Conclusions

This chapter formally introduced the sterile neutrino and the light 3+1 sterile neutrino model. The main result of this chapter was the allowed 3+1 sterile neutrino model parameter space given the current solar neutrino experimental data, as well as the effect of adding a future SNO+ pep solar neutrino measurement.

Current solar neutrino experiments already exclude some of the high alpha/low  $R_\Delta$  region of the sterile neutrino parameter space. Adding a SNO+ pep solar neutrino measurement that agrees with the LMA MSW solution would create a noticeably larger exclusion region for this high alpha/low  $R_\Delta$  parameter space.

Adding an expected SNO+ pep neutrino measurement that agrees with the MSW LMA solution has the largest impact on the  $R_\Delta$  parameter in the 3+1 sterile model. Without the SNO+ pep neutrino measurement, the value of  $R_\Delta$  that is allowed within one sigma is  $R_\Delta > 0.07$ . After a SNO+ pep measurement, the  $R_\Delta$  values allowed within one sigma is  $R_\Delta > 0.12$ .

Including an expected SNO+ pep neutrino measurement that agrees with the MSW LMA solution in the global analysis does have a weak effect on the allowed values of  $\alpha$ , though it is more difficult to quantify this effect due to the shape of the allowed region. Including the two year live-time measurement of the SNO+ pep neutrino had the largest effect on reducing the allowed parameter space for  $\alpha$ .

This work represents the first analysis which examines how the pep neutrino measurement will affect the 3+1 sterile neutrino model. If the SNO+ measurement is significantly different from the LMA MSW prediction, then a 3+1 sterile model could be used to explain the discrepancy.

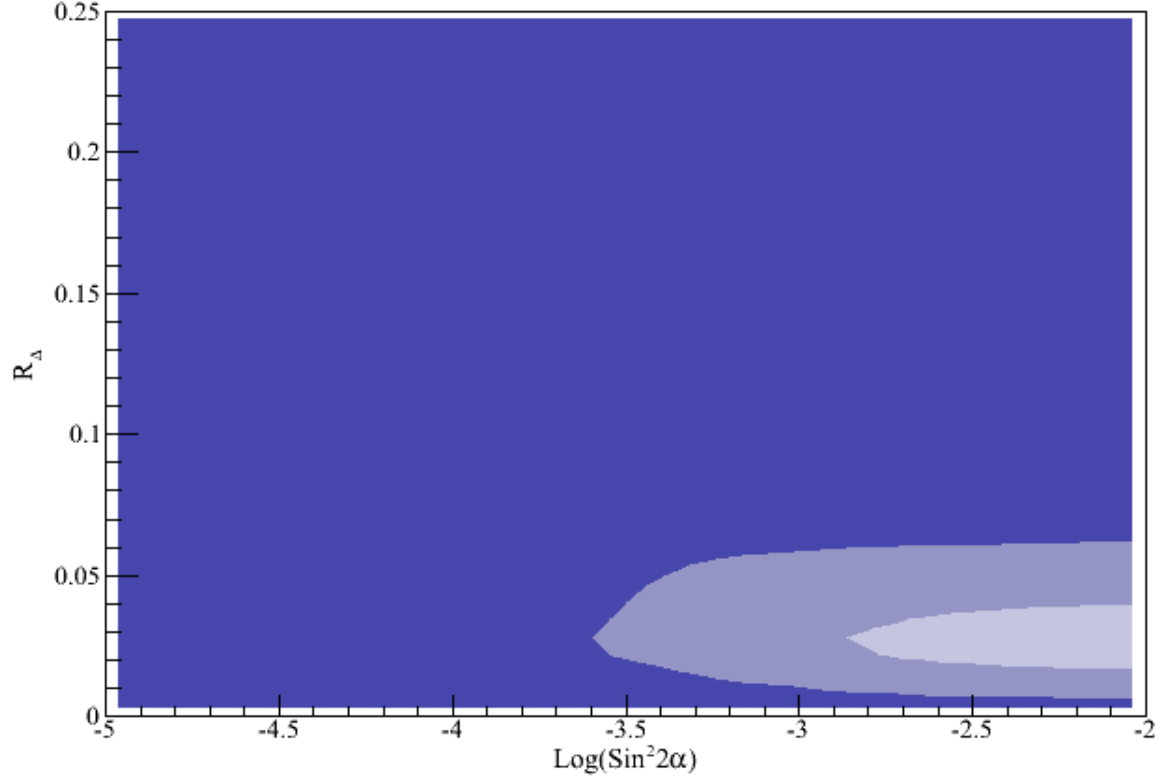


Figure 5.7: Allowed sterile neutrino parameters considering radiochemical experiments only. As seen here, because these experiments mainly measure low energy solar neutrinos, they are sensitive to the low  $R_{\Delta}$  region of the 3+1 model. The dark blue region represents the model parameters which result in a  $\Delta\chi^2 < 2.30$ , which means that these values are allowed within the 68.27% confidence level. The medium blue represents the model parameters which result in a  $2.30 < \Delta\chi^2 < 5.99$ , which means that these values are allowed within the 95% confidence level. The lightest blue represents the model parameters which result in a  $5.99 < \Delta\chi^2 < 11.83$ , which means that these values are allowed within the 99.73% confidence level. All active oscillation parameters are fixed to the best fit values from [36].

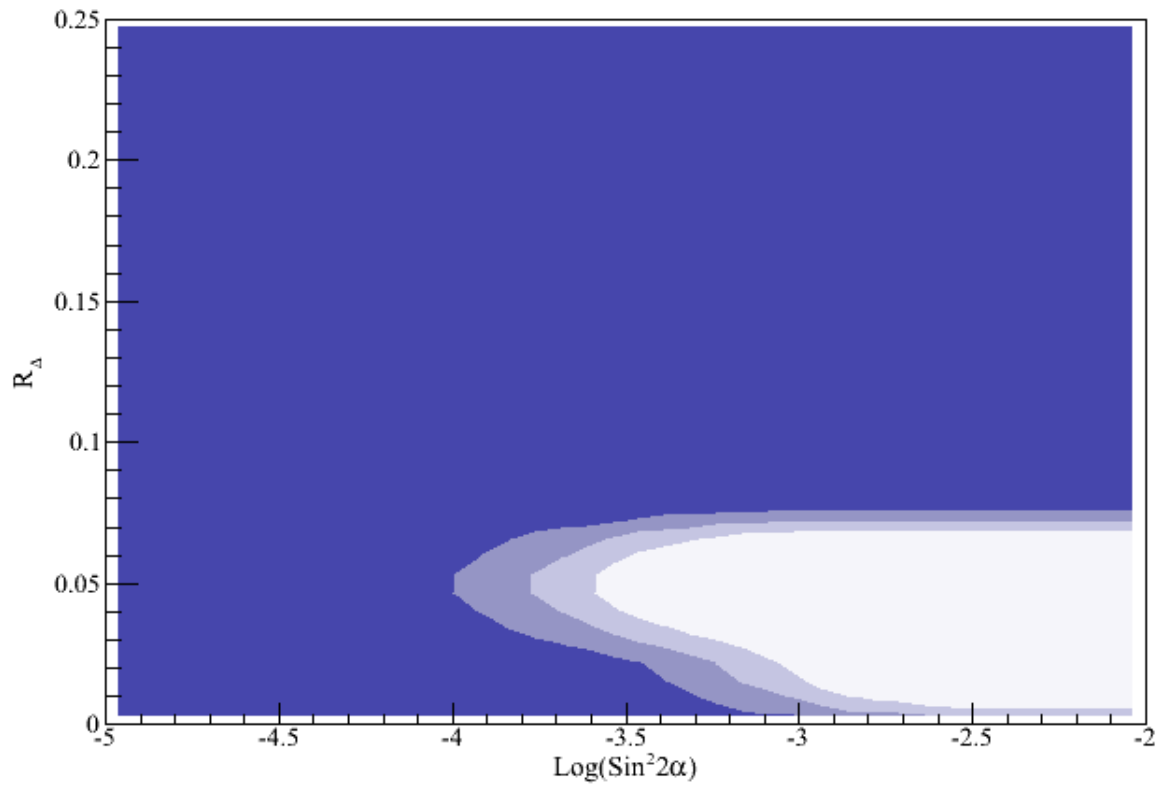


Figure 5.8: Allowed sterile neutrino parameters considering the Borexino  ${}^7\text{Be}$  solar neutrino measurement only. Contour colours represent the  $\chi^2$  regions as in Figure 5.7. All active oscillation parameters are fixed to the best fit values from [36].

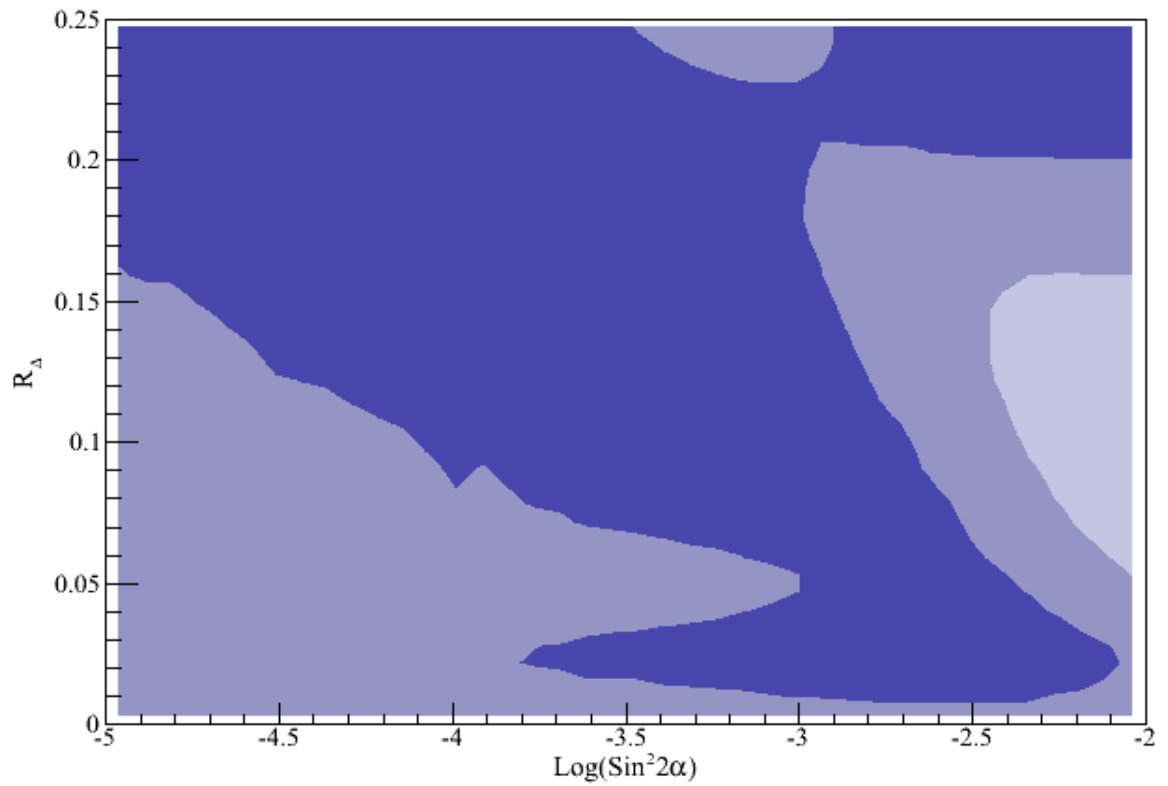


Figure 5.9: Allowed sterile neutrino parameters considering the  $^8\text{B}$  solar neutrino measurements from SNO and SK only. The low  $R_\Delta$ /low  $\alpha$  region is now allowed at less than one sigma and thus a sterile neutrino is somewhat favoured when considering this data. Contour colours represent the  $\chi^2$  regions as in Figure 5.7. All active oscillation parameters are fixed to the best fit values from [36].

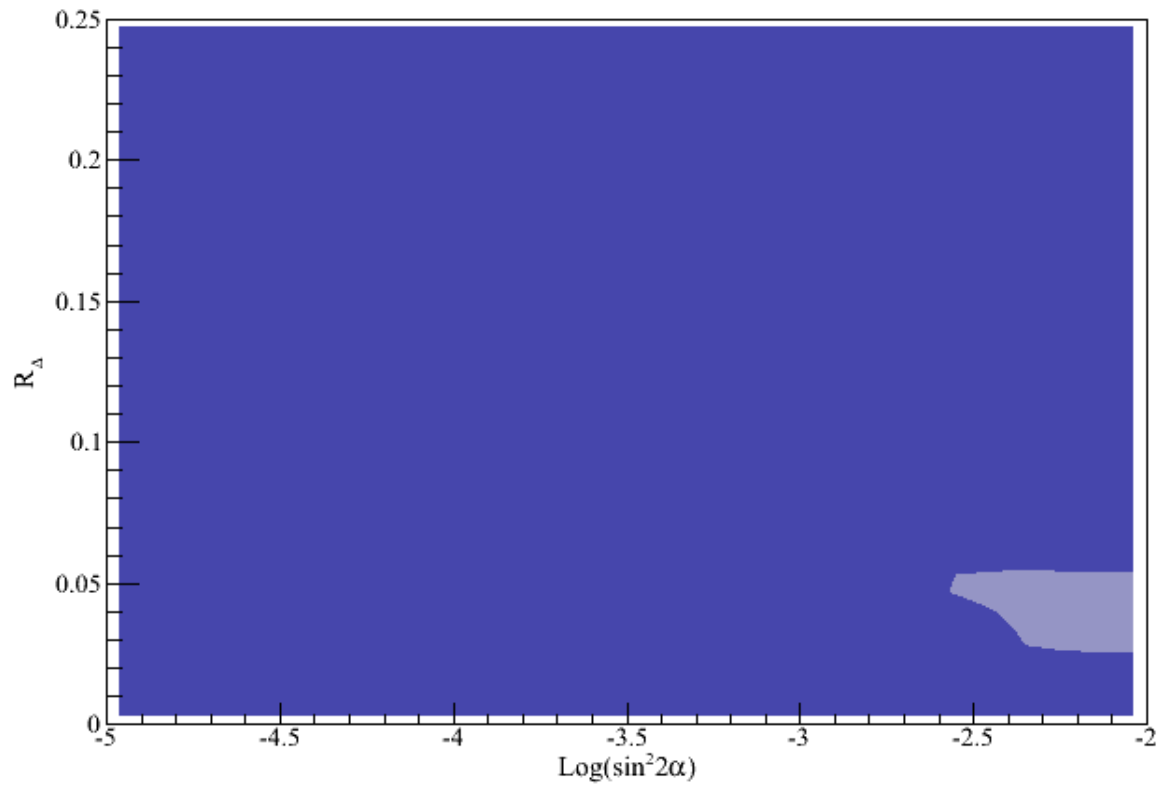


Figure 5.10: Allowed sterile neutrino parameters considering the pep solar neutrino measurements from Borexino only. Contour colours represent the  $\chi^2$  regions as in Figure 5.7. All active oscillation parameters are fixed to the best fit values from [36].

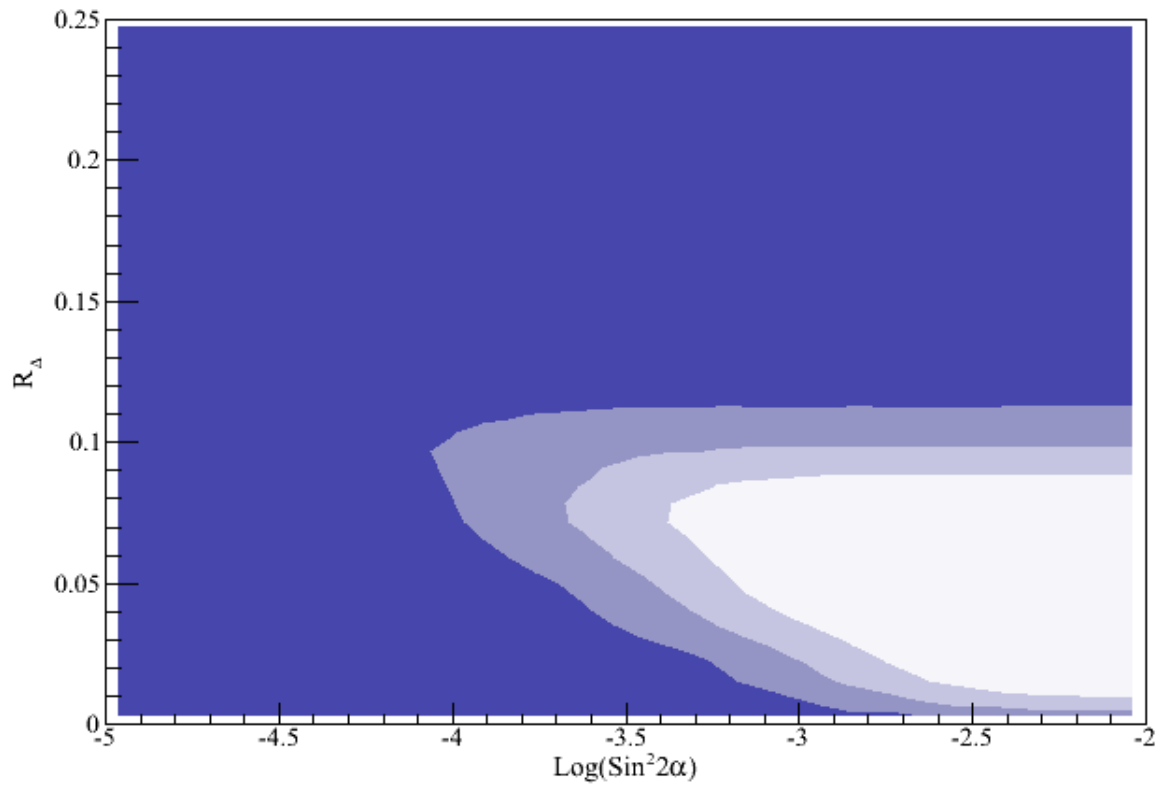


Figure 5.11: Allowed sterile neutrino parameters considering an example of a future pep solar neutrino measurement, which agrees with the LMA solution, from SNO+. Contour colours represent the  $\chi^2$  regions as in Figure 5.7. All active oscillation parameters are fixed to the best fit values from [36].

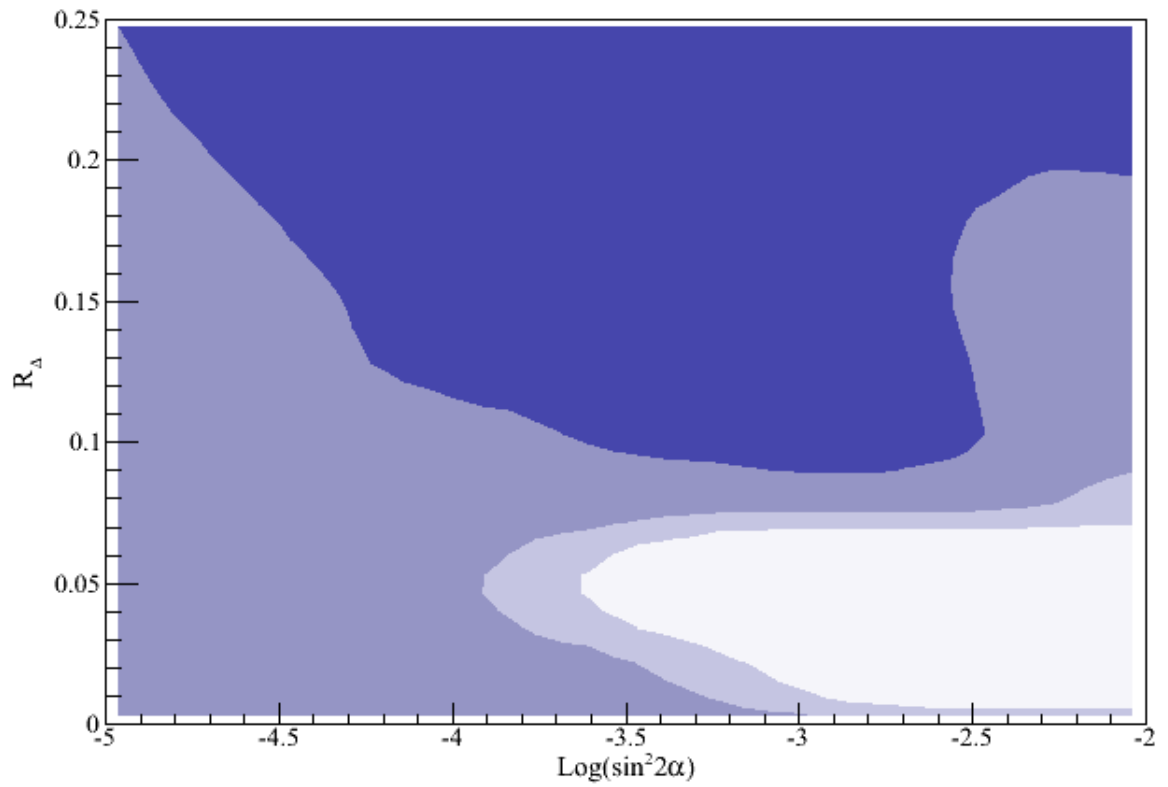


Figure 5.12: Allowed sterile neutrino parameters considering all current solar neutrino data. Contour colours represent the  $\chi^2$  regions as described in Figure 5.7. All active oscillation parameters are fixed to the best fit values from [36], except for  $\theta_{12}$  which is marginalized.

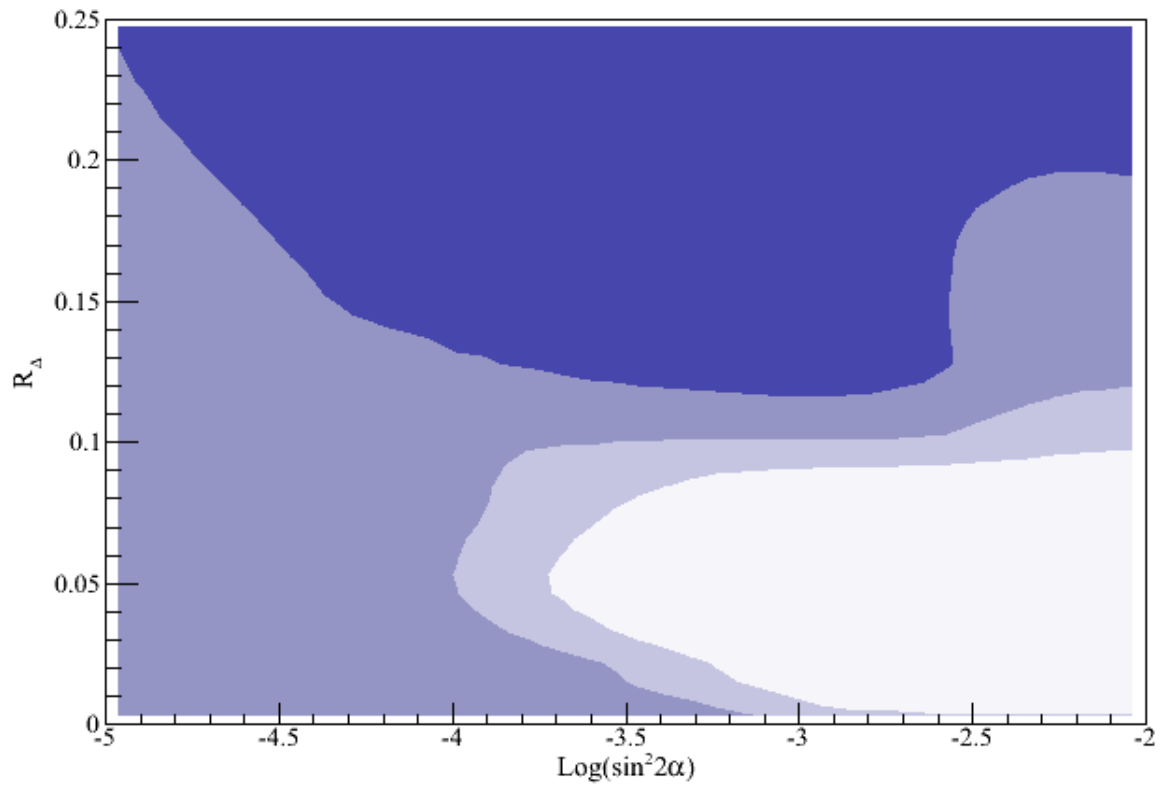


Figure 5.13: Allowed sterile neutrino parameters considering all current solar neutrino data and the expected LMA pep signal after one year of SNO+ live-time. Contour colours represent the  $\chi^2$  regions as described in Figure 5.7. All active oscillation parameters are fixed to the best fit values from [36], except for  $\theta_{12}$  which is marginalized.

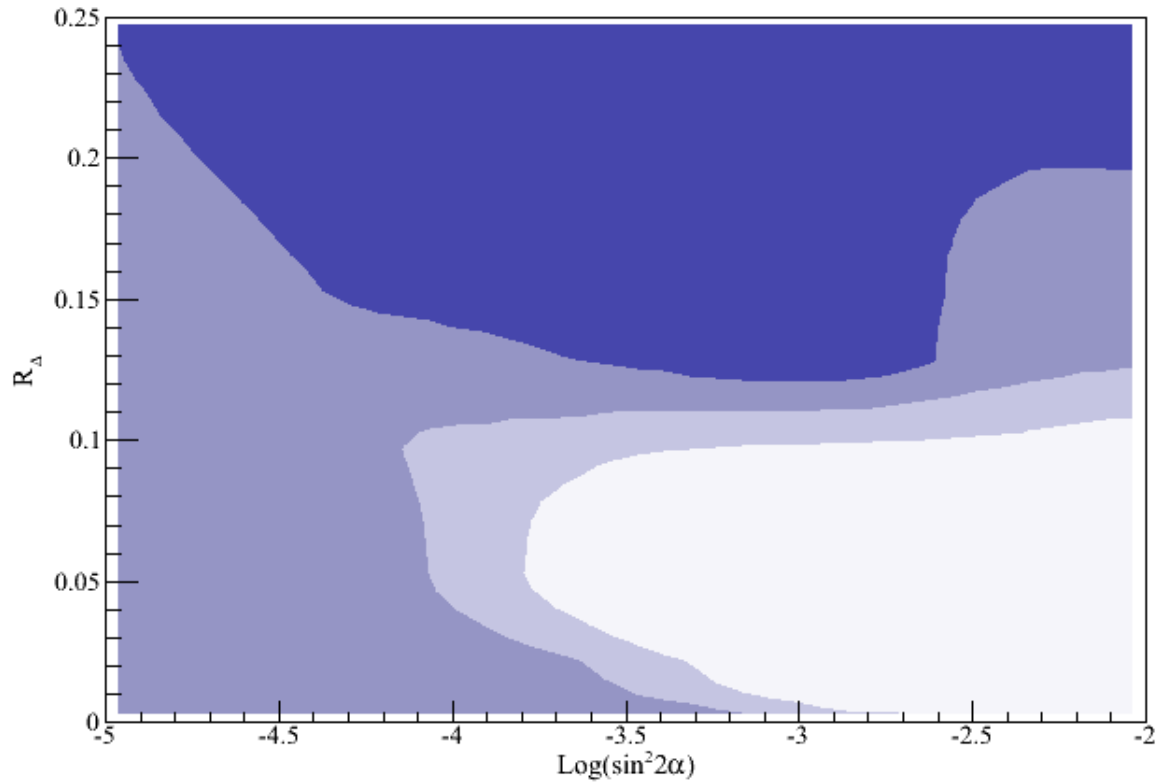


Figure 5.14: Allowed sterile neutrino parameters considering all current solar neutrino data and the expected LMA pep signal after two years of SNO+ live-time. Contour colours represent the  $\chi^2$  regions as described in Figure 5.7. All active oscillation parameters are fixed to the best fit values from [36], except for  $\theta_{12}$  which is marginalized.

# Chapter 6

## Conclusions and Recommendations

This thesis outlined important developments in the SNO+ experiment. The first part of the thesis addressed tools which can be used to extract signals from backgrounds, while the second part showed how a signal from SNO+ could impact the neutrino community.

Chapter 4 described the measurement of the scintillator timing pulse for LAB+PPO, as well as the feasibility of using PSD to separate between alpha and beta events. Using data from a bench-top experiment, it was found that using the peak-to-total discrimination parameter was an excellent method of separating events from alpha and beta excitation. Implementing these results into RAT in order to consider detector effect lead to a reduction in PSD capability using the peak-to-total method. Using Gatti's method to discriminate events was found to restore the PSD capability in the detector to the level of the bench top results. It is therefore the recommendation of this author that Gatti's method should be used for PSD in the SNO+ detector.

Chapter 5 outlined a study which probed a 3+1 sterile neutrino model using solar neutrino measurements. If SNO+ were to make a precision pep solar neutrino

measurement that was in agreement with the LMA solution, then some low  $R_\Delta$  and high  $\alpha$  parameters which are allowed in the current global fit could be excluded. It is therefore the recommendation of this author that a precision pep solar neutrino measurement be pursued and that the results be examined in the context of constraining sterile neutrinos.

# Bibliography

- [1] RENO Collaboration and J. K. Ahn. RENO: An Experiment for Neutrino Oscillation Parameter  $\theta_{13}$  Using Reactor Neutrinos at Yonggwang. *ArXiv e-prints*, March 2010, [arXiv:1003.1391](#) [hep-ex].
- [2] W. Beriguete, J. Cao, Y. Ding, S. Hans, et al. Production of Gadolinium-loaded Liquid Scintillator for the Daya Bay Reactor Neutrino Experiment. *ArXiv e-prints*, February 2014, [arXiv:1402.6694](#) [physics.ins-det].
- [3] M. Wurm, J. F. Beacom, L. B. Bezrukov, D. Bick, et al. The next-generation liquid-scintillator neutrino observatory LENA. *Astroparticle Physics*, 35:685–732, June 2012, [arXiv:1104.5620](#) [astro-ph.IM]. doi:10.1016/j.astropartphys.2012.02.011.
- [4] W. Pauli. Dear radioactive ladies and gentlemen. *Phys. Today*, 31N9:27, 1978.
- [5] J. Chadwick. The existence of a neutron. *Proceedings of the Royal Society of London. Series A*, 136(830):692–708, 1932.
- [6] F. Reines and C. L. Cowan. Detection of the free neutrino. *Phys. Rev.*, 92:830–831, Nov 1953. doi:10.1103/PhysRev.92.830.
- [7] F. Reines and C. L. Cowan. The neutrino. *Nature*, 178(4531):446–449, 1956.
- [8] T. D. Lee and C. N. Yang. Question of parity conservation in weak interactions. *Phys. Rev.*, 104:254–258, Oct 1956. doi:10.1103/PhysRev.104.254.
- [9] C. S. Wu, E. Ambler, R. W. Hayward, D. D. Hoppes, et al. Experimental Test of Parity Conservation in Beta Decay. *Physical Review*, 105:1413–1415, February 1957. doi:10.1103/PhysRev.105.1413.
- [10] M. Goldhaber, L. Grodzins, and A. W. Sunyar. Helicity of neutrinos. *Phys. Rev.*, 109:1015–1017, Feb 1958. doi:10.1103/PhysRev.109.1015.
- [11] R. Davis Jr. A half-century with solar neutrinos. *Usp. Fiz. Nauk*, 174(4):408–417, 2004.

- [12] R. Davis. Solar neutrinos. II. experimental. *Phys. Rev. Lett.*, 12:303–305, Mar 1964. doi:10.1103/PhysRevLett.12.303.
- [13] B. Pontecorvo and I. B. Decay. Chalk river report PD-205 (1946). *Usp. fiz. nauk*, 141:675, 1983.
- [14] J. N. Bahcall. Solar models: An historical overview. *Nuclear Physics B - Proceedings Supplements*, 118(0):77 – 86, 2003. ISSN 0920-5632. doi:http://dx.doi.org/10.1016/S0920-5632(03)01306-9. Proceedings of the XXth International Conference on Neutrino Physics and Astrophysics.
- [15] J. N. Bahcall and R. J. Davis. Solar Neutrinos: A Scientific Puzzle. *Science*, 191:264–267, January 1976. doi:10.1126/science.191.4224.264.
- [16] K. S. Hirata, T. Kajita, T. Kifune, K. Kihara, et al. Observation of  $^8\text{B}$  solar neutrinos in the Kamiokande-II detector. *Phys. Rev. Lett.*, 63:16–19, Jul 1989. doi:10.1103/PhysRevLett.63.16.
- [17] W. Hampel et al. GALLEX solar neutrino observations: Results for GALLEX IV. *Phys. Lett.*, B447:127–133, 1999.
- [18] J. N. Abdurashitov, V. N. Gavrin, S. V. Girin, V. V. Gorbachev, et al. Measurement of the solar neutrino capture rate with gallium metal. *Physical Review C*, 60(5):055801, November 1999, arXiv:astro-ph/9907113. doi:10.1103/PhysRevC.60.055801.
- [19] J. Abdurashitov, E. Faizov, V. Gavrin, A. Gusev, et al. Results from SAGE (the Russian-American gallium solar neutrino experiment). *Physics Letters B*, 328(12):234 – 248, 1994. ISSN 0370-2693. doi:http://dx.doi.org/10.1016/0370-2693(94)90454-5.
- [20] M. Altmann, M. Balata, P. Belli, E. Bellotti, et al. Complete results for five years of GNO solar neutrino observations. *Physics Letters B*, 616(34):174 – 190, 2005. ISSN 0370-2693. doi:http://dx.doi.org/10.1016/j.physletb.2005.04.068.
- [21] V. Gribov and B. Pontecorvo. Neutrino astronomy and lepton charge. *Physics Letters B*, 28(7):493 – 496, 1969. ISSN 0370-2693. doi:http://dx.doi.org/10.1016/0370-2693(69)90525-5.
- [22] H. H. Chen. Direct approach to resolve the solar-neutrino problem. *Phys. Rev. Lett.*, 55:1534–1536, Sep 1985. doi:10.1103/PhysRevLett.55.1534.

- [23] H. H. Chen. The sudbury neutrino observatory: Solar and supernova neutrino studies with a large heavy water cherenkov detector. *Nuclear Instruments and Methods in Physics Research Section A: Accelerators, Spectrometers, Detectors and Associated Equipment*, 264(1):48 – 54, 1988. ISSN 0168-9002. doi:[http://dx.doi.org/10.1016/0168-9002\(88\)91101-1](http://dx.doi.org/10.1016/0168-9002(88)91101-1).
- [24] Q. R. Ahmad, R. C. Allen, T. C. Andersen, J. D. Anglin, et al. Direct evidence for neutrino flavor transformation from neutral-current interactions in the sudbury neutrino observatory. *Phys. Rev. Lett.*, 89:011301, Jun 2002. doi:10.1103/PhysRevLett.89.011301.
- [25] Y. Fukuda, T. Hayakawa, E. Ichihara, K. Inoue, et al. Evidence for oscillation of atmospheric neutrinos. *Physical Review Letters*, 81(8):1562, 1998.
- [26] G. Danby, J. Gaillard, K. Goulianos, L. Lederman, et al. Observation of high-energy neutrino reactions and the existence of two kinds of neutrinos. *Physical Review Letters*, 9(1):36–44, 1962.
- [27] K. Kodama, N. Ushida, C. Andreopoulos, N. Saoulidou, et al. Observation of tau neutrino interactions. *Physics Letters B*, 504(3):218 – 224, 2001. ISSN 0370-2693. doi:[http://dx.doi.org/10.1016/S0370-2693\(01\)00307-0](http://dx.doi.org/10.1016/S0370-2693(01)00307-0).
- [28] D. Decamp, B. Deschizeaux, J.-P. Lees, M.-N. Minard, et al. A precise determination of the number of families with light neutrinos and of the Z boson partial widths. *Physics Letters B*, 235(34):399 – 411, 1990. ISSN 0370-2693. doi:[http://dx.doi.org/10.1016/0370-2693\(90\)91984-J](http://dx.doi.org/10.1016/0370-2693(90)91984-J).
- [29] OPAL Collaboration, G. Abbiendi, and et al. Precise determination of the Z resonance parameters at LEP: “Zedometry”. *European Physical Journal C*, 19:587–651, March 2001, [hep-ex/0012018](http://arxiv.org/abs/hep-ex/0012018). doi:10.1007/s100520100627.
- [30] DELPHI Collaboration, P. Abreu, and et al. Cross-sections and leptonic forward-backward asymmetries from the Z<sup>0</sup> running of LEP. *European Physical Journal C*, 16:371–405, 2000.
- [31] L3 Collaboration, M. Acciarri, and et al. Measurements of cross sections and forward-backward asymmetries at the Z resonance and determination of electroweak parameters. *European Physical Journal C*, 16:1–40, 2000, [hep-ex/0002046](http://arxiv.org/abs/hep-ex/0002046).
- [32] F. Boehm and P. Vogel. *Physics of Massive Neutrinos*. Cambridge University Press, 1992.

- [33] R. M. Bionta, G. Blewitt, C. B. Bratton, D. Casper, et al. Observation of a neutrino burst in coincidence with supernova 1987a in the large magellanic cloud. *Phys. Rev. Lett.*, 58:1494–1496, Apr 1987. doi:10.1103/PhysRevLett.58.1494.
- [34] E. N. Alekseev, L. N. Alekseeva, V. I. Volchenko, and I. V. Krivosheina. Possible detection of a neutrino signal on 23 February 1987 at the Baksan underground scintillation telescope of the Institute of Nuclear Research. *Soviet Journal of Experimental and Theoretical Physics Letters*, 45:589, May 1987.
- [35] K. Hirata, T. Kajita, M. Koshiba, M. Nakahata, et al. Observation of a neutrino burst from the supernova sn1987a. *Phys. Rev. Lett.*, 58:1490–1493, Apr 1987. doi:10.1103/PhysRevLett.58.1490.
- [36] J. Beringer, J.-F. Arguin, R. M. Barnett, K. Copic, et al. Review of Particle Physics. *Physicsal Review D*, 86(1):010001, July 2012. doi:10.1103/PhysRevD.86.010001.
- [37] B. Aharmim, S. N. Ahmed, A. E. Anthony, N. Barros, et al. Combined analysis of all three phases of solar neutrino data from the Sudbury Neutrino Observatory. *Physical Review C*, 88(2):025501, August 2013, arXiv:1109.0763 [nucl-ex]. doi:10.1103/PhysRevC.88.025501.
- [38] H. Sekiya and for the Super-Kamiokande Collaboration. Solar neutrino analysis of Super-Kamiokande. *ArXiv e-prints*, July 2013, arXiv:1307.3686 [astro-ph.SR].
- [39] A. Gando, Y. Gando, K. Ichimura, H. Ikeda, et al. Constraints on  $\theta_{13}$  from a three-flavor oscillation analysis of reactor antineutrinos at kamland. *Phys. Rev. D*, 83:052002, Mar 2011. doi:10.1103/PhysRevD.83.052002.
- [40] P. Adamson, C. Andreopoulos, R. Armstrong, D. J. Auty, et al. Measurement of the neutrino mass splitting and flavor mixing by minos. *Phys. Rev. Lett.*, 106:181801, May 2011. doi:10.1103/PhysRevLett.106.181801.
- [41] F. P. An, J. Z. Bai, A. B. Balantekin, H. R. Band, et al. Observation of electron-antineutrino disappearance at daya bay. *Phys. Rev. Lett.*, 108:171803, Apr 2012. doi:10.1103/PhysRevLett.108.171803.
- [42] C. Athanassopoulos, L. B. Auerbach, R. L. Burman, I. Cohen, et al. Evidence for neutrino oscillations from muon decay at rest. *Physical Review C*, 54:2685–2708, November 1996, nucl-ex/9605001. doi:10.1103/PhysRevC.54.2685.

- [43] A. A. Aguilar-Arevalo, C. E. Anderson, S. J. Brice, B. C. Brown, et al. Event Excess in the MiniBooNE Search for  $\bar{\nu}_\mu \rightarrow \bar{\nu}_e$  Oscillations. *Physical Review Letters*, 105(18):181801, October 2010, [arXiv:1007.1150](https://arxiv.org/abs/1007.1150) [hep-ex]. doi:10.1103/PhysRevLett.105.181801.
- [44] J. M. Conrad, W. C. Louis, and M. H. Shaevitz. The LSND and MiniBooNE oscillation searches at high  $\Delta m^2$ . *Annual Review of Nuclear and Particle Science*, 63(1):45–67, 2013, <http://www.annualreviews.org/doi/pdf/10.1146/annurev-nucl-102711-094957>. doi:10.1146/annurev-nucl-102711-094957.
- [45] J. N. a. Abdurashitov. Measurement of the response of a gallium metal solar neutrino experiment to neutrinos from a  $^{51}\text{Cr}$  source. *Physical Review C*, 59:2246–2263, April 1999, [hep-ph/9803418](https://arxiv.org/abs/hep-ph/9803418). doi:10.1103/PhysRevC.59.2246.
- [46] F. Kaether, W. Hampel, G. Heusser, J. Kiko, et al. Reanalysis of the GALLEX solar neutrino flux and source experiments. *Physics Letters B*, 685:47–54, February 2010, [arXiv:1001.2731](https://arxiv.org/abs/1001.2731) [hep-ex]. doi:10.1016/j.physletb.2010.01.030.
- [47] C. Giunti and C. W. Kim. *Neutrino Physics and Astrophysics*. Oxford University Press, 2007.
- [48] G. Mention, M. Fechner, T. Lasserre, T. A. Mueller, et al. Reactor antineutrino anomaly. *Physical Review D*, 83(7):073006, April 2011, [arXiv:1101.2755](https://arxiv.org/abs/1101.2755) [hep-ex]. doi:10.1103/PhysRevD.83.073006.
- [49] C. Kraus, B. Bornschein, L. Bornschein, J. Bonn, et al. Final results from phase II of the Mainz neutrino mass search in tritium  $\beta$  decay. *The European Physical Journal C - Particles and Fields*, 40(4):447–468, 2005. ISSN 1434-6044. doi:10.1140/epjc/s2005-02139-7.
- [50] V. N. Aseev, A. I. Belesev, A. I. Berlev, E. V. Geraskin, et al. Upper limit on the electron antineutrino mass from the Troitsk experiment. *Physical Review D*, 84(11):112003, December 2011, [arXiv:1108.5034](https://arxiv.org/abs/1108.5034) [hep-ex]. doi:10.1103/PhysRevD.84.112003.
- [51] J. Wolf. The KATRIN neutrino mass experiment. *Nuclear Instruments and Methods in Physics Research Section A: Accelerators, Spectrometers, Detectors and Associated Equipment*, 623(1):442 – 444, 2010. ISSN 0168-9002. doi: <http://dx.doi.org/10.1016/j.nima.2010.03.030>. 1st International Conference on Technology and Instrumentation in Particle Physics.

- [52] A. Renshaw, K. Abe, Y. Hayato, K. Iyogi, et al. First Indication of Terrestrial Matter Effects on Solar Neutrino Oscillation. *ArXiv e-prints*, December 2013, [arXiv:1312.5176 \[hep-ex\]](#).
- [53] BOREXINO Collaboration, C. Arpesella, G. Bellini, J. Benziger, et al. First real time detection of  ${}^7\text{Be}$  solar neutrinos by Borexino. *Physics Letters B*, 658:101–108, January 2008, [arXiv:0708.2251](#). doi:10.1016/j.physletb.2007.09.054.
- [54] Borexino Collaboration. First Evidence of pep Solar Neutrinos by Direct Detection in Borexino. *Physical Review Letters*, 108(5):051302, February 2012, [arXiv:1110.3230 \[hep-ex\]](#). doi:10.1103/PhysRevLett.108.051302.
- [55] G. Bellini, D. Bick, G. Bonfini, D. Bravo, et al. SOX: Short distance neutrino Oscillations with BoreXino. *Journal of High Energy Physics*, 2013(8):1–14, 2013. doi:10.1007/JHEP08(2013)038.
- [56] A. Porta, V. Bui, M. Cribier, M. Fallot, et al. Reactor neutrino detection for non-proliferation with the NUCIFER experiment. *Nuclear Science, IEEE Transactions on*, 57(5):2732–2739, 2010.
- [57] J. N. Bahcall, A. Serenelli, and S. Basu. New solar opacities, abundances, helioseismology, and neutrino fluxes. *Astrophysical Journal Letters*, 621:L85–L88, mar 2005, [arXiv:astro-ph/0412440](#). doi:10.1086/428929.
- [58] N. Barros. *Precision Measurement of Neutrino Oscillation Parameters: Combined Three-phase Results of the Sudbury Neutrino Observatory*. Ph.D. thesis, University of Lisbon, 2011.
- [59] S. P. Mikheev and A. I. Smirnov. Resonant amplification of neutrino oscillations in matter and solar-neutrino spectroscopy. *Nuovo Cimento C Geophysics Space Physics C*, 9:17–26, February 1986. doi:10.1007/BF02508049.
- [60] L. Wolfenstein. Neutrino oscillations in matter. *Physical Review D*, 17:2369–2374, May 1978. doi:10.1103/PhysRevD.17.2369.
- [61] H. A. Bethe. Possible explanation of the solar-neutrino puzzle. *Phys. Rev. Lett.*, 56:1305–1308, Mar 1986. doi:10.1103/PhysRevLett.56.1305.
- [62] A. Y. Smirnov. The MSW effect and Solar Neutrinos. *ArXiv High Energy Physics - Phenomenology e-prints*, May 2003, [hep-ph/0305106](#).
- [63] J. Boger, R. Hahn, J. Rowley, A. Carter, et al. The sudbury neutrino observatory. *Nuclear Instruments and Methods in Physics Research Section A: Accelerators, Spectrometers, Detectors and Associated Equipment*, 449(12):172 – 207, 2000. ISSN 0168-9002. doi:[http://dx.doi.org/10.1016/S0168-9002\(99\)01469-2](http://dx.doi.org/10.1016/S0168-9002(99)01469-2).

- [64] P. Jones. *Background Rejection for the Neutrinoless Double Beta Decay Experiment for SNO+*. Ph.D. thesis, Oxford University, 2012.
- [65] E. O’Sullivan. SNO+ long term soak tests. Technical Report SNO+-doc-381-v1, December 2009.
- [66] G. McGoldrick. The effect of LAB on crazing in acrylic. Technical Report SNO+-doc-508-v1, May 2010.
- [67] M. Lay, D. Wark, and N. West. It’s alive-the birth of snoman. Technical report, SNO report SNOSTR-91-077, 1991.
- [68] S. Agostinelli, J. Allison, K. Amako, J. Apostolakis, et al. Geant4 – a simulation toolkit. *Nuclear Instruments and Methods in Physics Research Section A: Accelerators, Spectrometers, Detectors and Associated Equipment*, 506(3):250 – 303, 2003. ISSN 0168-9002. doi:[http://dx.doi.org/10.1016/S0168-9002\(03\)01368-8](http://dx.doi.org/10.1016/S0168-9002(03)01368-8).
- [69] R. Brun and F. Radenmakers. ROOT – an object oriented data analysis framework. *Nucl. Inst. & Meth. in Phys. Res. A*, 389:81–86, 1997.
- [70] S. Andringa and B. von Krosigk. Overview over anti-neutrino group activities and status. Technical Report SNO+-doc-2452-v3, March 2014.
- [71] M. Chen. Geo-neutrinos in SNO+. *Earth, Moon, and Planets*, 99(1-4):221–228, 2006. ISSN 0167-9295. doi:[10.1007/s11038-006-9116-4](https://doi.org/10.1007/s11038-006-9116-4).
- [72] B. Mueller and H.-T. Janka. A New Multi-Dimensional General Relativistic Neutrino Hydrodynamics Code for Core-Collapse Supernovae IV. The Neutrino Signal. *ArXiv e-prints*, February 2014, [arXiv:1402.3415](https://arxiv.org/abs/1402.3415) [astro-ph.SR].
- [73] I. Coulter. Nucleon decay plenary talk. Technical Report SNO+-doc-2114-v2, August 2013.
- [74] S. R. Elliott and P. Vogel. Double beta decay. *Annual Review of Nuclear and Particle Science*, 52:115–151, 2002, [arXiv:hep-ph/0202264](https://arxiv.org/abs/hep-ph/0202264). doi:[10.1146/annurev.nucl.52.050102.090641](https://doi.org/10.1146/annurev.nucl.52.050102.090641).
- [75] M. Redshaw, G. Bollen, M. Brodeur, S. Bustabad, et al. Atomic mass and double- $\beta$ -decay  $Q$  value of  $^{48}\text{Ca}$ . *Phys. Rev. C*, 86:041306, Oct 2012. doi:[10.1103/PhysRevC.86.041306](https://doi.org/10.1103/PhysRevC.86.041306).
- [76] W. Rodejohann. Neutrino-Less Double Beta Decay and Particle Physics. *International Journal of Modern Physics E*, 20:1833–1930, 2011, [arXiv:1106.1334](https://arxiv.org/abs/1106.1334) [hep-ph]. doi:[10.1142/S0218301311020186](https://doi.org/10.1142/S0218301311020186).

- [77] N. N. D. Center. Chart of nuclides, 2014.
- [78] R. Arnold, C. Augier, J. Baker, A. S. Barabash, et al. Measurement of the  $\beta\beta$  Decay Half-Life of  $^{130}\text{Te}$  with the NEMO-3 Detector. *Physical Review Letters*, 107(6):062504, August 2011, [arXiv:1104.3716](https://arxiv.org/abs/1104.3716) [nucl-ex]. doi:10.1103/PhysRevLett.107.062504.
- [79] C. Arnaboldi, D. Artusa, F. A. III, M. Balata, et al. First results on neutrinoless double beta decay of  $^{130}\text{Te}$  with the calorimetric {CUORICINO} experiment. *Physics Letters B*, 584(34):260 – 268, 2004. ISSN 0370-2693. doi:<http://dx.doi.org/10.1016/j.physletb.2004.01.040>.
- [80] F. T. Avignone, III, S. R. Elliott, and J. Engel. Double beta decay, Majorana neutrinos, and neutrino mass. *Reviews of Modern Physics*, 80:481–516, April 2008, [arXiv:0708.1033](https://arxiv.org/abs/0708.1033) [nucl-ex]. doi:10.1103/RevModPhys.80.481.
- [81] S. Biller. Final talk as presented at TAUP 2013. Technical Report SNO+-doc-2130-v4, September 2013.
- [82] CUORE Collaboration, D. R. Artusa, F. T. Avignone, III, O. Azzolini, et al. Searching for neutrinoless double-beta decay of  $^{130}\text{Te}$  with CUORE. *ArXiv e-prints*, February 2014, [arXiv:1402.6072](https://arxiv.org/abs/1402.6072) [physics.ins-det].
- [83] M. Auger, D. Auty, P. Barbeau, E. Beauchamp, et al. Search for neutrinoless double-beta decay in  $^{136}\text{Xe}$  with exo-200. *Physical review letters*, 109(3):032505, 2012.
- [84] A. Gando et al. Limit on Neutrinoless  $\beta\beta$  Decay of  $^{136}\text{Xe}$  from the First Phase of KamLAND-Zen and Comparison with the Positive Claim in  $^{76}\text{Ge}$ . *Phys.Rev.Lett.*, 110(6):062502, 2013, [arXiv:1211.3863](https://arxiv.org/abs/1211.3863) [hep-ex]. doi:10.1103/PhysRevLett.110.062502.
- [85] M. Agostini, M. Allardt, E. Andreotti, A. M. Bakalyarov, et al. Results on Neutrinoless Double- $\beta$  Decay of  $^{76}\text{Ge}$  from Phase I of the GERDA Experiment. *Physical Review Letters*, 111(12):122503, September 2013, [arXiv:1307.4720](https://arxiv.org/abs/1307.4720) [nucl-ex]. doi:10.1103/PhysRevLett.111.122503.
- [86] S. Umehara, T. Kishimoto, I. Ogawa, R. Hazama, et al. CANDLES for double beta decay of  $^{48}\text{Ca}$ . *Journal of Physics: Conference Series*, 39:356, 2006.
- [87] Majorana Collaboration. The Majorana Experiment. *Nuclear Physics B Proceedings Supplements*, 221:364–364, December 2011, [arXiv:1109.4790](https://arxiv.org/abs/1109.4790) [nucl-ex]. doi:10.1016/j.nuclphysbps.2011.10.016.

- [88] H. Klapdor-Kleingrothaus, A. Dietz, H. Harney, and I. Krivosheina. Evidence for neutrinoless double beta decay. *Modern Physics Letters A*, 16(37):2409–2420, 2001.
- [89] C. Pena-Garay and A. Serenelli. Solar neutrinos and the solar composition problem. *ArXiv e-prints*, November 2008, arXiv:0811.2424.
- [90] A. Friedland, C. Lunardini, and C. Pea-Garay. Solar neutrinos as probes of neutrino-matter interactions. *Physics Letters B*, 594(34):347 – 354, 2004. ISSN 0370-2693. doi:http://dx.doi.org/10.1016/j.physletb.2004.05.047.
- [91] G. Orebi Gann. Solar neutrino figures and slides. Technical Report SNO+-doc-1640-v3, Sept 2012.
- [92] F. Brooks. Development of organic scintillators. *Nuclear Instruments and Methods*, 162(13):477 – 505, 1979. ISSN 0029-554X. doi:http://dx.doi.org/10.1016/0029-554X(79)90729-8.
- [93] J. Birks. *The Theory and Practice of Scintillation Counting*. The MacMillan Company, New York, 1964.
- [94] Bollinger, L. M. and Thomas, G. E. Measurement of the Time Dependence of Scintillation Intensity by a Delayed-Coincidence Method. *Review of Scientific Instruments*, 32:1044–1050, September 1961. doi:10.1063/1.1717610.
- [95] H. M. O’Keeffe, E. O’Sullivan, and M. C. Chen. Scintillation decay time and pulse shape discrimination in oxygenated and deoxygenated solutions of linear alkylbenzene for the SNO+ experiment. *Nuclear Instruments and Methods in Physics Research A*, 640:119–122, June 2011, arXiv:1102.0797 [physics.ins-det]. doi:10.1016/j.nima.2011.03.027.
- [96] P. Lombardi, F. Ortica, G. Ranucci, and A. Romani. Decay time and pulse shape discrimination of liquid scintillators based on novel solvents. *Nuclear Instruments and Methods in Physics Research A*, 701:133–144, February 2013. doi:10.1016/j.nima.2012.10.061.
- [97] T. Marrodñ Undagoitia, F. von Feilitzsch, L. Oberauer, W. Potzel, et al. Fluorescence decay-time constants in organic liquid scintillators. *Review of Scientific Instruments*, 80(4):043301, 2009. doi:http://dx.doi.org/10.1063/1.3112609.
- [98] L. Xiao-Bo, X. Hua-Lin, C. Jun, L. Jin, et al. Timing properties and pulse shape discrimination of lab-based liquid scintillator. *Chinese Physics C*, 35(11):1026, 2011.

- [99] H. O. Back, M. Balata, G. Bellini, J. Benziger, et al. Pulse-shape discrimination with the Counting Test Facility. *Nuclear Instruments and Methods in Physics Research A*, 584:98–113, January 2008, [arXiv:0705.0239 \[physics.ins-det\]](#). doi:10.1016/j.nima.2007.09.036.
- [100] F. L. Villante, A. Ianni, F. Lombardi, G. Pagliaroli, et al. A step toward CNO solar neutrino detection in liquid scintillators. *Physics Letters B*, 701:336–341, July 2011, [arXiv:1104.1335 \[hep-ph\]](#). doi:10.1016/j.physletb.2011.05.068.
- [101] E. Gatti and F. De Martini. Optimum linear filter for pulse shape recognition in the presence of thermal noise. *Energia nucleare (Milan)*, 9, 1962.
- [102] K. N. Abazajian, M. A. Acero, S. K. Agarwalla, A. A. Aguilar-Arevalo, et al. Light Sterile Neutrinos: A White Paper. *ArXiv e-prints*, April 2012, [arXiv:1204.5379 \[hep-ph\]](#).
- [103] K. Abe, Y. Hayato, T. Iida, M. Ikeda, et al. Solar neutrino results in Super-Kamiokande-III. *Physical Review D*, 83(5):052010, March 2011, [arXiv:1010.0118 \[hep-ex\]](#). doi:10.1103/PhysRevD.83.052010.
- [104] P. C. de Holanda, W. Liao, and A. Y. Smirnov. Toward precision measurements in solar neutrinos. *Nuclear Physics B*, 702:307–332, December 2004, [hep-ph/0404042](#). doi:10.1016/j.nuclphysb.2004.09.027.
- [105] P. C. de Holanda and A. Y. Smirnov. Solar neutrino spectrum, sterile neutrinos, and additional radiation in the Universe. *Physical Review D*, 83(11):113011, June 2011, [arXiv:1012.5627 \[hep-ph\]](#). doi:10.1103/PhysRevD.83.113011.
- [106] R. Martin. *Numerical Methods and Approximations for the Calculation of Solar Neutrino Fluxes in Three Flavours Focused on Results for the Sudbury Neutrino Observatory*. Master’s thesis, Queen’s University, 2006.
- [107] B. T. Cleveland, T. Daily, J. Raymond Davis, J. R. Distel, et al. Measurement of the solar electron neutrino flux with the homestake chlorine detector. *The Astrophysical Journal*, 496(1):505, 1998.
- [108] R. Davis. A review of the homestake solar neutrino experiment. *Progress in Particle and Nuclear Physics*, 32(0):13 – 32, 1994. ISSN 0146-6410. doi: [http://dx.doi.org/10.1016/0146-6410\(94\)90004-3](http://dx.doi.org/10.1016/0146-6410(94)90004-3).
- [109] J. N. Bahcall, B. T. Cleveland, R. Davis, I. Dostrovsky, et al. Proposed solar-neutrino experiment using  $^{71}\text{Ga}$ . *Phys. Rev. Lett.*, 40:1351–1354, May 1978. doi:10.1103/PhysRevLett.40.1351.

- [110] J. N. Abdurashitov, V. N. Gavrin, V. V. Gorbachev, P. P. Gurkina, et al. Measurement of the solar neutrino capture rate with gallium metal. III. Results for the 2002-2007 data-taking period. *Physical Review C*, 80(1):015807, July 2009, arXiv:0901.2200 [nucl-ex]. doi:10.1103/PhysRevC.80.015807.
- [111] F. Kaether. *Data analysis of the solar neutrino experiment GALLEX*. Ph.D. thesis, University of Heidelberg, 2007.
- [112] S. Fukuda, Y. Fukuda, T. Hayakawa, E. Ichihara, et al. The Super-Kamiokande detector. *Nuclear Instruments and Methods in Physics Research Section A: Accelerators, Spectrometers, Detectors and Associated Equipment*, 501(23):418 – 462, 2003. ISSN 0168-9002. doi:http://dx.doi.org/10.1016/S0168-9002(03)00425-X.
- [113] S. Fukuda, Y. Fukuda, M. Ishitsuka, Y. Itow, et al. Determination of solar neutrino oscillation parameters using 1496 days of Super-Kamiokande-I data. *Physics Letters B*, 539:179–187, July 2002, hep-ex/0205075. doi:10.1016/S0370-2693(02)02090-7.
- [114] J. P. Cravens, K. Abe, T. Iida, K. Ishihara, et al. Solar neutrino measurements in Super-Kamiokande-II. *Physical Review D*, 78(3):032002, August 2008, arXiv:0803.4312 [hep-ex]. doi:10.1103/PhysRevD.78.032002.
- [115] BOREXINO Collaboration, G. Alimonti, C. Arpesella, H. Back, et al. The Borexino detector at the Laboratori Nazionali del Gran Sasso. *Nuclear Instruments and Methods in Physics Research A*, 600:568–593, March 2009, arXiv:0806.2400 [physics.ins-det]. doi:10.1016/j.nima.2008.11.076.
- [116] G. Bellini, J. Benziger, D. Bick, S. Bonetti, et al. Precision measurement of the  $^7\text{Be}$  solar neutrino interaction rate in Borexino. *Phys. Rev. Lett.*, 107:141302, Sep 2011. doi:10.1103/PhysRevLett.107.141302.
- [117] H. O’Keeffe. *Low Energy Background in the NCD Phase of the Sudbury Neutrino Observatory*. Ph.D. thesis, Oxford University, 2008.

# Appendix A

## Background Decay Chains

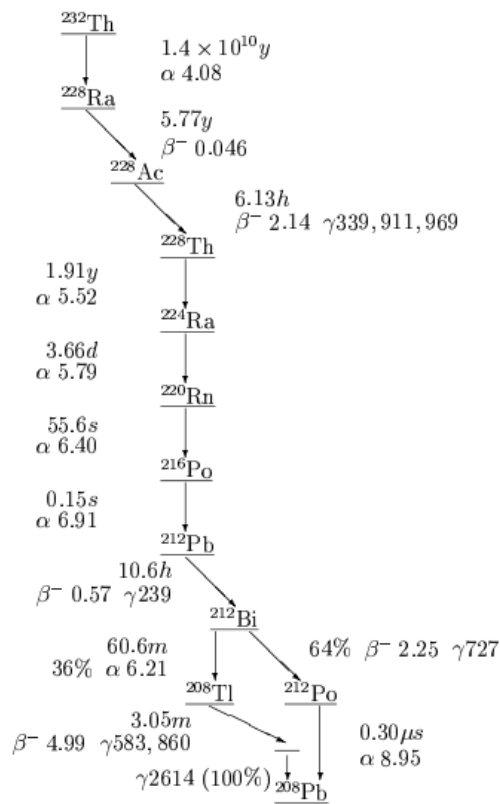


Figure A.1: Thorium decay chain. [117]

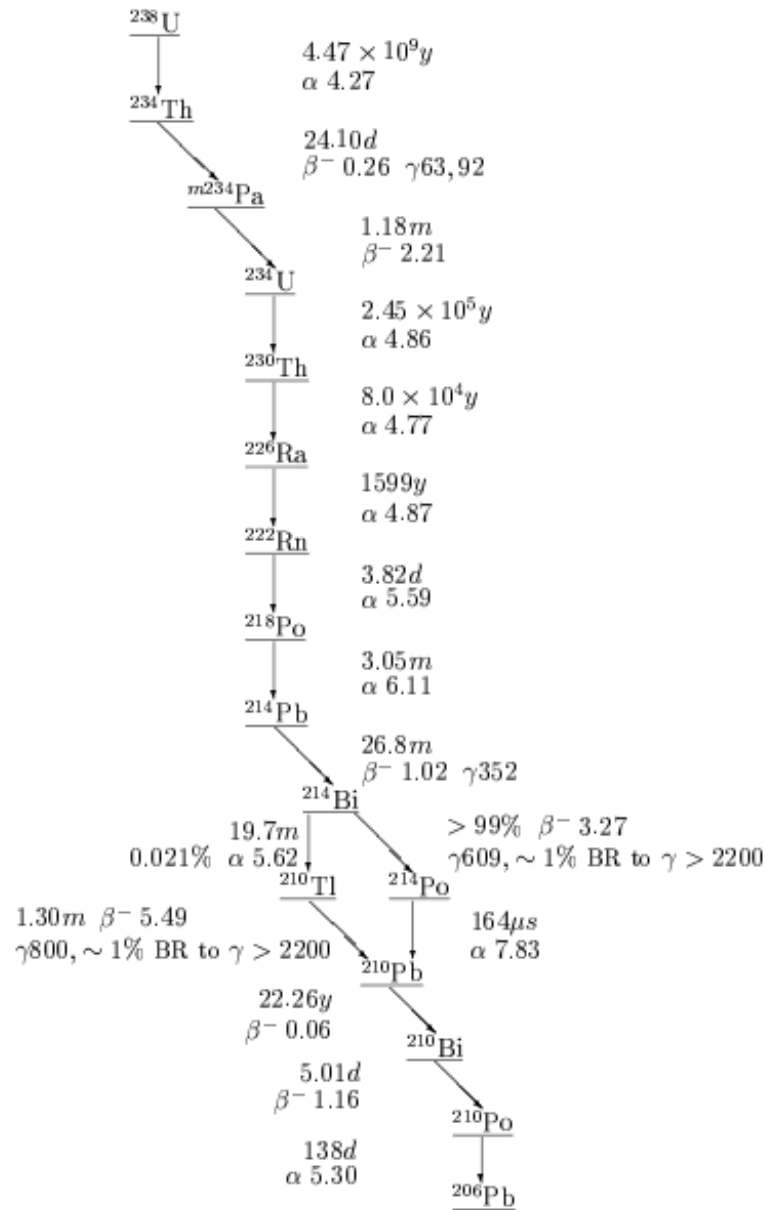


Figure A.2: Uranium decay chain. [117]

# Appendix B

## List of Important Acronyms

<b>CC</b>	Charged current
<b>NC</b>	Neutral current
<b>CNO</b>	Carbon-Nitrogen-Oxygen cycle
<b>CP</b>	Charge-parity
<b>RAT</b>	Reactor Analysis Tools
<b>AV</b>	Acrylic vessel
<b>PMT</b>	Photomultiplier tube
<b>PSUP</b>	Photomultiplier support structure
<b>LAB</b>	Linear alkylbenzene
<b>PSD</b>	Pulse shape discrimination
<b>TAC</b>	Time to amplitude convertor
<b>MCA</b>	Multichannel analyser
<b>TOF</b>	Time of flight
<b>LMA</b>	Large mixing angle
<b>SNU</b>	Solar neutrino unit